



저작자표시-비영리-변경금지 2.0 대한민국

이용자는 아래의 조건을 따르는 경우에 한하여 자유롭게

- 이 저작물을 복제, 배포, 전송, 전시, 공연 및 방송할 수 있습니다.

다음과 같은 조건을 따라야 합니다:



저작자표시. 귀하는 원저작자를 표시하여야 합니다.



비영리. 귀하는 이 저작물을 영리 목적으로 이용할 수 없습니다.



변경금지. 귀하는 이 저작물을 개작, 변형 또는 가공할 수 없습니다.

- 귀하는, 이 저작물의 재이용이나 배포의 경우, 이 저작물에 적용된 이용허락조건을 명확하게 나타내어야 합니다.
- 저작권자로부터 별도의 허가를 받으면 이러한 조건들은 적용되지 않습니다.

저작권법에 따른 이용자의 권리는 위의 내용에 의하여 영향을 받지 않습니다.

이것은 [이용허락규약\(Legal Code\)](#)을 이해하기 쉽게 요약한 것입니다.

[Disclaimer](#)

공학박사학위논문

**나노 덴드라이트 구조의 루테튬 연료  
극을 이용한 박막 단실형 고체산화물  
연료전지 개발에 관한 연구**

Development of Thin Film Single Chamber Solid Oxide  
Fuel Cell Using Nano-Dendritic Ru-GDC Anodes

2016년 8월

서울대학교 대학원

기계항공공학부

이 윤 호

Development of Thin Film Single Chamber Solid Oxide  
Fuel Cell Using Nano-Dendritic Ru-GDC Anodes

by

**Yoon Ho Lee**

A Dissertation Submitted in Partial Fulfillment

of the Requirements for the Degree of

**DOCTOR OF PHILOSOPHY**

**Department of Mechanical and Aerospace Engineering**

**Seoul National University**

**August 2016**

## **ABSTRACT**

# **Study on Thin Film Solid Oxide Fuel Cell Using Hydrocarbon as a Fuel**

Yoon Ho Lee

Department of Mechanical and Aerospace Engineering

Seoul National University

Student number: 2010-30966

Fuel cells are energy conversion device which directly converts chemical energy into electric energy. Since it has no moving parts, high reliability and continuous conversion is guaranteed. However, conventional fuel cells have too high or low operating temperature due to the characteristics of electrolyte materials. To solve the temperature issue of fuel cells, high temperature ( $800^{\circ}\text{C}$ ) operating solid oxide fuel cell was operated at intermediate temperature between  $500\sim 600^{\circ}\text{C}$ . Intermediate temperature operation of solid oxide fuel cell has advantages of allowing cheap stainless steel components and improved system stability. Additionally, to solve the problem of hydrogen storage and inefficient production, we directly operated fuel cell with hydrocarbon fuels without reformers. It requires

advanced anode and cathode structure and material.

To verify the application of thin film for SOFCs, we used sputtering to fabricate metal and ceramic nano-composite electrodes. We analyzed morphological and electrochemical data by different ratio of metal and ceramic composite films. The porosity and grain size was increased while increasing the pressure of sputtering chamber. On the other hand the porosity and grain size was decreased while decreasing the pressure of sputtering chamber. It shows that control of morphology and catalytic activity can be managed by modification of sputtering conditions.

In the past, a thin film YSZ was usually fabricated by sputtering of ceramic targets. We used the reactive sputtering by mixture of oxygen in the sputtering gas to fabricate YSZ film from Y/Zr metal alloy.

Application of above listed nano fabrication technic, we fabricated thin film SOFCs using Ru-Ni-GDC anodes for direct hydrocarbon operation. It showed about 80mW/cm<sup>2</sup> of peak power density and it was less than 10% of performance difference than that of hydrogen operation. If the Ru-Ni-GDC mixture is more uniform, higher performance is expected

Last, we fabricated thin film single chamber SOFCs and measured electro chemical performances. By co-sputtering of Ru-GDC in 200W and 50W respectively, nano-dendritic structure was successfully fabricated and it showed

superior catalytic activity and thermo mechanical stability. The cathodes were fabricated with sputter and pulsed laser deposition. To improve the electric conductivity of nano fabricated perovskite cathode, Au was used as a current collecting and surface modifying material. The Au-SSC co-sputtered cathode shows more than 13time bigger peak power density compared to the pure SSC. In case of cell using pulsed laser deposited LSCF as a cathode, it showed 560mW/cm<sup>2</sup> of peak power density at 550°C under single chamber condition of  $R_{mix}=2$ .

**Key words:** Single chamber, Thin Film SOFC, Sputter, pulsed laser deposition

## CONTENTS

<b>ABSTRACT .....</b>	<b>iii</b>
<b>CONTENTS.....</b>	<b>vi</b>
<b>CHAPTER 1 INTRODUCTION.....</b>	<b>1</b>
<b>1.1 Motivation .....</b>	<b>1</b>
1.1.1 Fundamentals of fuel cells .....	1
<b>1.2 Introduction to thin film solid oxide fuel cell .....</b>	<b>4</b>
1.2.1 Thin film fabrication technics .....	6
1.2.1.1 Sputtering .....	6
1.2.1.2 Pulsed laser deposition .....	10
1.2.1.3 Atomic layer deposition .....	13
1.2.2 Overview of thin film SOFCs structure .....	17
<b>1.3 Single chamber operation of SOFCs .....</b>	<b>20</b>
<b>CHAPTER 2 Thin film application to solid oxide fuel cells .....</b>	<b>29</b>
2.1 Thin film application to solid oxide fuel cell electrodes .....	29
2.1.1 Introduction .....	29
2.1.2 Experimental .....	32
2.1.3 Results and Discussion.....	34
2.1.3.1 Thermal stability of the Pt-based nanocomposite electrode .....	34
2.1.3.2 Cell application and electrochemical analysis.....	38
2.1.4 Conclusion.....	48
2.2 Thin film application to solid oxide fuel cell electrolyts .....	49
<b>CHAPTER 3 Operation of thin film SOFCs using direct methane fuel.....</b>	<b>54</b>
3.1 Introduction .....	54

3.2 Experimental.....	57
3.3 Results and Discussion .....	59
3.4 Conclusion.....	66
<b>CHAPTER 4 Single chamber operation of thin film SOFCs.....</b>	<b>67</b>
4.1 Introduction .....	67
4.2 Experimental.....	68
4.3 Result and discussion.....	69
4.3.1 Characterization of anode materials and structure .....	69
4.3.2 Characterization of thin film perovskite electrodes for cathode. ....	75
4.3.2 Characterization of thin film single chamber SOFCs. ....	75
4.4 Conclusion.....	91
<b>CHAPTER 5 Concluding remarks .....</b>	<b>92</b>
<b>REFERENCES.....</b>	<b>94</b>
<b>국문 초록</b>	<b>107</b>

## List of Figures

Figure 1.1 Characteristics of solid oxide fuel cells in the temperature range or 500°C – 1000°C

Figure 1.2 (a) Conventional and (b) nano fabricated electrode on the electrolyte with the particle size of (a) 500nm – 1µm, (b) 10nm – 50nm.

Figure 1.3 Schematic diagram of sputtering devices.

Figure 1.4 Schematic diagram of pulsed laser deposition devices.

Figure 1.5 Schematic diagram of ALD processes: (a) A precursor delivery to a substrate, (b) purging an inert gas for neutralizing a process chamber, (c) The second precursor delivery to a substrate, (d) purging an inert gas for neutralizing a process chamber.

Figure 1.6 (a) Thin film SOFC structure of free-standing membrane, (b) thin film SOFC on hydrogen permeable palladium substrates, (c) thin film SOFC on porous anode substrates.

Figure 1.7 Schematic diagram of (a) dual chamber operation with gas separators and seal, (b) single chamber operation using mixture of air and fuel to the entire cell.

Figure 1.8 Designs of single chamber SOFCs. (a) Conventional, (b) co-planar and (c) all porous structure

Figure 1.9 The upper flammability limit and lower flammability limit of methane as a function of temperature.

Figure 2.1 Schematic image of (a) the thermal barrier GDC coating on a Pt electrode and a (b) dispersion-hardened Pt / GDC obtained by co-sputtering.

Figure 2.2 Surface SEM images of the pure Pt and thermal barrier GDC coating on Pt. Electrodes of before [(a)Pure, (b)5nm-GDC coated, (c)10nm-GDC coated] and after [(d)Pure, (e)5nm-GDC coated, (f)10nm-GDC coated] operating at 500°C for

Figure 2.3 Surface SEM images of dispersion hardened Pt – GDC electrodes by co-sputtering. Electrodes of before [(a)95% Pt / 5% GDC, (b)90% Pt / 10% GDC, (c)

80% Pt / 20% GDC] and after [(d)95% Pt / 5% GDC, (e)90% Pt / 10% GDC, (f) 80% Pt / 20% GDC] operating at 500°C for an hour.

Figure 2.4 (a) Initial and (b) 1 hour after I-V behaviors and power densities of thermal barrier GDC coating on Pt electrodes at 500 °C.

Figure 2.5 (a) Initial and (b) 1 hour after I-V behaviors and power densities of dispersion-hardened Pt / GDC co-sputtered electrodes at 500 °C.

Figure 2.6 (a) Initial and (b) 1 hour after EIS analysis of thermal barrier GDC coating on Pt electrodes at 500 °C.

Figure 2.7 (a) Initial and (b) 1 hour after EIS analysis of dispersion-hardened Pt / GDC co-sputtered electrodes at 500 °C.

Figure 2.8 12 hour potentiostamperometry data of pure Pt, 10nm-GDC coated Pt and co-sputtered 95% Pt / 5% GDC electrodes at 0.7V.

Figure 2.9 XRD patterns of thin film YSZ prepared by reactive sputtering of Y/Zr metal targets.

Figure 2.10 FE-SEM analysis of (a) surface, (b) cross-sectional images of YSZ film by reactive sputtering of Y/Zr metal alloy using Ar + O<sub>2</sub> mixture gas.

Figure 3.1 Cell image of thin film SOFC using direct hydrocarbon as a fuel.

Figure 3.2 FE-SEM analysis of Ni based anodes. As deposited samples of (a) Ni and (b) Ru/Ni-GDC. Samples after Sintering at 600°C. (a) Ni and (b) Ru/Ni-GDC.

Figure 3.3 FE-SEM analysis of (a) cross section of the cell and (b) surface of the YSZ electrolyte.

Figure 3.4 Performance of thin film SOFC using different fuels at 500°C. The fuels were supplied with fully humidified hydrogen and methane at room temperature. The flow rates of fuels were 100scm.

Figure 3.5 Impedance spectra of SOFC using different fuels at 500°C. The measurement was taken at OCV.

Figure 4.1 The surface and the cross-sectional image of the Ni-GDC electrodes by FE-SEM. (a) Surface image of as-deposited Ni-GDC, (b) surface image of heat-

treated Ni-GDC at 650°C, (c) cross-sectional image of as-deposited Ni-GDC, (d) cross-sectional image of as-deposited Ni-GDC

Figure 4.2 The surface and the cross-sectional image of the Ru-GDC electrodes by FE-SEM. (a) Surface image of as-deposited Ru-GDC, (b) surface image of heat-treated Ru-GDC at 650°C, (c) cross-sectional image of as-deposited Ru-GDC, (d) cross-sectional image of as-deposited Ru-GDC

Figure 4.3 Cross sectional images of thin film SOFCs using (a) Ni-GDC and (b) Ru-GDC as an anode material.

Figure 4.4 I-V curves of thin film SOFCs using (a) Ni-GDC and (b) Ru-GDC as an anode material. The cell was operated under dual chamber configuration of 600°C, and mixture of methane and air of  $R_{mix}=2$  was supplied to the anode side. The cathode was exposed for natural air supply.

Figure 4.5 Surface and cross sectional FE-SEM image of thin film SSC electrode by sputtering. The sputtering condition was 50mtorr of Ar chamber pressure and 100W of RF power to ceramic SSC target.

Figure 4.6 Surface and FE-SEM image of thin film SSC electrode after heat treatment by sputtering. (a) 500°C heat treated with 50mtorr of Ar chamber pressure, (b) 700°C heat treated with 50mtorr of Ar chamber pressure, (c) 500°C heat treated with 120mtorr of Ar chamber pressure, (a) 700°C heat treated with 120mtorr of Ar chamber pressure, .

Figure 4.7 Open circuit voltage measurements of cell using (a) 700°C heat-treated SSC fabricated under 50mtorr of sputtering chamber, (b) 700°C heat-treated SSC fabricated under 120mtorr of sputtering chamber.

Figure 4.8 Surface FE-SEM analysis of Au-SSC with a co-sputtering condition of (a) 50W of DC power to the Au target and 200W of RF power to the SSC target, (b) 100W of DC power to the Au target and 200W of RF power to the SSC target.

Figure 4.9 I-V and power density curves of fuel cell with Au-SSC cathodes on 500um YSZ pellet.

Figure 4.10 Impedance Spectra of fuel cell with Au-SSC cathodes on 500um YSZ pellet.

Figure 4.11 Surface FE-SEM analysis of LSCF by pulsed laser deposition at the chamber pressure of (a) 200mtorr, (b) 100mtorr, (c) 75mtorr, (b) 50mtorr

Figure 4.12 Surface images of Au on LSCF (a) as-deposited and (b) after operation.

Figure 4.13 Cross section of thin film single chamber SOFCs cell with a cell configuration of Ru-GDC/ YSZ / GDC / LSCF / Au.

Figure 4.14 I-V behaviors and power densities of thin film single chamber SOFCs cell with a cell configuration of Ru-GDC/ YSZ / GDC / LSCF / Au.

## **List of Tables**

Table 2.1 Deposition parameters of the thermal barrier GDC coated Pt electrodes

Table 2.2 Deposition parameters of dispersion-hardened Pt and GDC co-sputtered electrodes

Table 2.3 Initial performance, 1 hour after performance, and degradation percentages of cells using Pt / GDC composite electrodes.

Table 2.4 EIS measured initial and 1 hour after reaction resistances and resistance increments of the cells using Pt / GDC composite electrodes

Table 4.1 Performances of single chamber SOFC using YSZ electrolyte.

# **.Chapter 1 Introduction**

## **1.1 Motivation**

### **1.1.1 Fundamentals of fuel cells**

Fuel cells have in common to batteries in the respect of generating electricity. Although fuel cells and batteries both use electrochemical reactions to produce electrical energy, but the fuel cells only consume fuels. Thus, fuel cells permanently generate electricity while providing fuels, and this is the main difference between fuel cells and batteries[1].

In this respect, internal combustion engines are also similar to fuel cells, while internal combustion engines convert a chemical energy of fuel into electrical energy. However, the main difference between fuel cells and internal combustion engines are converting procedures. While internal combustion engines pass through the two converting process (chemical to mechanical, mechanical to electrical energy), fuel cells pass just one conversion process (chemical to electrical). Thus, energy efficiency of fuel cells is higher than that of internal combustion engines. Additionally, clean emission without any NO<sub>x</sub> and SO<sub>x</sub> during operation is guaranteed, while fuel cells use hydrogen or hydrocarbon as a fuel. Since fuel cells don't have the driving unit, it could be the ideal energy conversion device due to the friction-free operation.

Although fuel cells have those advantages, still some issues have to be solved for commercialization. First issue to solve is the expensive price of fuel cell components. In case of polymer electrolyte fuel cells, it is forced to use expensive

platinum based catalysts due to low operating temperature. Solid oxide fuel cells also have price issues, since high temperature operating requires high system stability and reliability. Fuel flexibility is also issue in fuel cell commercialization. Fuel cells usually use hydrogen as a fuel but almost 95% of hydrogens are generated by reforming hydrocarbons and nearly 30% of fuels are lost during the procedure. Additionally, hydrogen is hard to storage at liquid form and metal hydrides are still too heavy to use. The most serious problem is low power density of fuel cells. Power densities are the power generated at certain volume or weight. Although power densities of fuel cells are improved by research for decades, it needs further more improvement for commercialization.

For improvement of fuel cell performance, we clarify the elements effecting fuel cells performance. The first elements effecting fuel cells performance is activation loss which related to the reaction speed of electrochemical reaction at electrodes. When the rate of electrochemical reaction at electrodes increases, current generation also increases. The most commonly used method to increase the electrochemical reaction at electrodes is applying catalytic materials at electrodes. Thus using suitable catalyst of the reaction and enlarging catalytic reaction sites are key factors to decrease activation loss. In addition, activation losses are more dominantly observed in polymer electrolyte fuel cells due to the low operating temperature.

The second elements effecting fuel cells performance is ohmic loss which is related to the electric and ionic conductivity of electrodes and electrolytes respectively. Unlike electrons, ions such as  $H^+$  and  $O^{2-}$  have relatively poor

mobility due to the bigger size and mass. The path of the ions in fuel cells are electrolytes and ions are passing through the electrolytes by the hopping method which is far inefficient than that of the electrons. Therefore, movement of the ions may cause a significant loss due to the resistance, which degrades the performance of the fuel cell. In particular, solid oxide fuel cell requires a high temperature of over 800°C because of the ion conducting mechanism of the ceramic electrolytes. It is required to fabricate material which has higher ionic conductivity and applying thin film electrolyte to minimize the path of the ions.

The third elements effecting fuel cells performance is mass transport loss which is related to a supply and removal of a reaction product. If the fuel and oxidant are not rapidly supplied to the fuel cell, there will be a limitation of fuel cells performance regardless of the activation and the ohmic losses. Additionally, if the water and carbon dioxide of fuel cells products doesn't rapidly removed, the products will be accumulated at electrodes and degrade the performance. It is important to design the flow field for effective deliver and removal of reactants and products to minimize mass transport losses.

## 1.2 Introduction to thin film solid oxide fuel cell.

SOFCs are fuel cells which the anode, electrolyte and cathode materials are consist of solid oxides. As mentioned above, high temperature operation is required for SOFCs and it is the main bottleneck of commercialization [2]. The high operating temperature causes stability problems of SOFC components and difficulties of thermal managements. If we can lower the operating temperature between 500-600°C, we can avoid the problems of high temperature operation, while maintaining the advantages of SOFC. According to the Figure 1, intermediate temperature operating SOFCs (IT-SOFC) allow metallic components such as stainless steel, thus we can avoid using expensive LaCoO<sub>3</sub> based interconnecting materials. Furthermore, internal reforming of hydrocarbon can be more stabilized without carbon deposition of anodes due to avoiding Bouduard reaction (under 500°C) and pyrolysis of methane (over 700°C) [3].

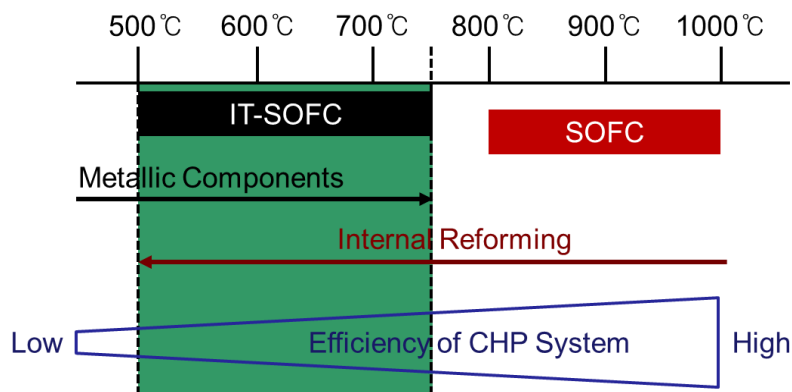


Figure 1.1 Characteristics of solid oxide fuel cells in the temperature range or 500°C – 1000°C

While it is reasonable to operate SOFCs in the intermediate temperature regime, there are lots of technical issues. First issue to solve is temperature dependency of ceramic electrolytes. According to the relationship between temperature and resistance of electrolyte (1), ionic conductivity decreases while temperature decreases. Thus, operating SOFCs in intermediate temperature regime without any technical modification will show lower performance. Furthermore, catalytic activity of ceramic electrodes is also proportional to the temperature, so electrodes have to be also modified.

While there have been numerous researches to solve the technical issues of IT-SOFC, one the most attracting candidate is application of nanotechnology. Referring to equation (1), thickness of electrolyte is inverse proportional to the resistance of electrolyte. Thus, the application of thin film electrolytes by nano-fabrication can offset the loss of the conductivity of low temperature operation (FIG. 2. (a)). In case of nano fabrication of electrodes, nano sized particle of catalyst can improve triple phase boundary (TPB) area (FIG. 2. (b)).

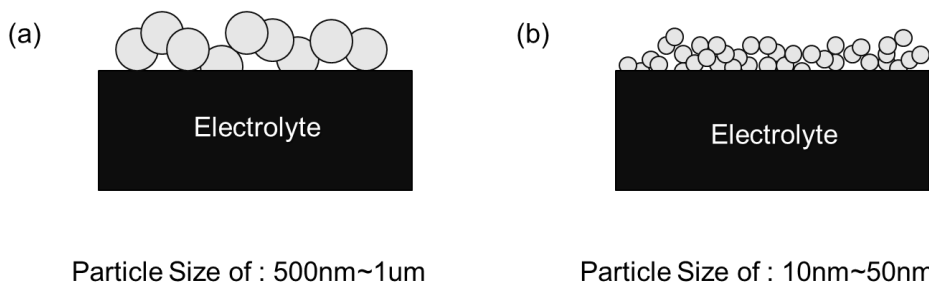


Figure 1.2 (a) Conventional and (b) nano fabricated electrode on the electrolyte with the particle size of (a) 500nm – 1um, (b) 10nm – 50nm.

### **1.2.1 Thin film fabrication technics**

Thin film fabrication technics are usually categorized into physical vapor depositions (PVD) and chemical vapor depositions (CVD). If the vaporizing process of target materials is caused by physical process, it is categorized into PVD, and if the vaporizing process of target materials is caused by chemical process, it is categorized into CVD.

#### **1.2.1.1 Sputtering**

A Sputtering is a widely used PVD method due to fine reproducibility of the thin film and capability of both metal and ceramic materials. In sputtering procedure, atoms are ejected from a solid target material due to the bombardment of energetic particles (Figure 3). It has features of controlling the microstructures of thin films by adjusting process parameters such as the power, target-to-substrate (TS) distance and the chamber pressure [4–6]. Both fully dense and highly porous films can be readily formed [7,8] because the film porosity tends to change with the chamber background pressure. In addition, crystallinity and chemical properties can be controlled by adjusting the substrate temperature and background gas species [9–12].

YSZ has been widely used as electrolyte material for SOFCs due to its moderate ionic conductivity and excellent mechanical and chemical stability under fuel-cell operation environments [10]. Unfortunately, it does not have sufficient ionic conductivity at a temperature range below 700 °C [10]; thus, to overcome this issue, the thickness of electrolyte needs to be decreased to alleviate the ionic

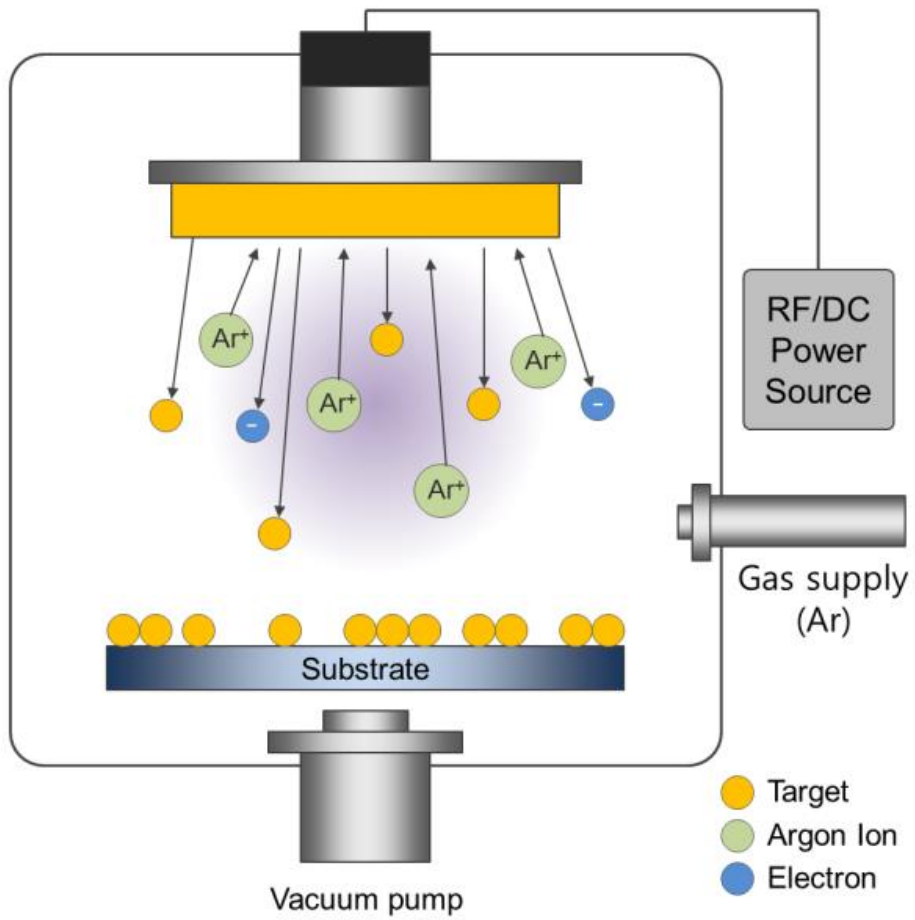


Figure 1.3 Schematic diagram of sputtering devices.

resistance, which can be resolved by a sputtering method, which has appropriate characteristics for synthesizing high-quality SOFC electrolytes [9,10,12–15]. To verify the optimal doping ratio of yttria, YSZ thin films with various yttria concentrations were fabricated by reactive sputtering methods using a gas mixture containing argon and oxygen. Jung *et al.* reported that YSZ thin films with various yttria concentrations ranging from 0.5% to 9.1 % were fabricated using YSZ metal targets with various Y:Zr composition ratios [14]. The relationship between the oxygen ion conductivity and doping concentration of the sputtered YSZ thin films was somewhat different from those of bulk YSZs. In particular, a 6.5% YSZ thin film showed the highest ionic conductivity at an operating temperature of 400°C, and a 3.2% YSZ thin film showed high performance at an operating temperature of 300°C [14]. In case of bulk YSZ, optimal doping concentrations are between 8~10% in terms of ionic conductivity. These findings reveal that the optimal acceptor doping concentrations of sputtered YSZ thin films are far different from those of bulk YSZs

Also, many studies have reported that the thermal energy during the sputtering process significantly influences the crystalline and microstructural properties of YSZ thin films [12,16]. The crystallinity of YSZ thin films deposited at a substrate temperature below 150°C are relatively weak, whereas YSZ thin films with a polycrystalline structure can be fabricated in a substrate temperature range of 200 to 600 °C [11,12,16].

Although ceria based electrolytes have higher ionic conductivity compared to the YSZ, it has several disadvantages, such as unstable chemical properties

during operation and high electric conductivity[17,18]. The electron conduction of GDC can occur poor open circuit voltages (OCVs) and leakage of current [5,6,17,18], thus GDC films are widely used as a functional layer of YSZ electrolyte. Swanson *et al.* reported that a GDC thin film deposited on an R-plane sapphire substrate had a polycrystalline structure with a dominant (111) orientation with an average grain size of 80 nm [18]. An epitaxial GDC thin film having a dominant (001) orientation was deposited on single-crystal CeO<sub>2</sub> supported by R-plane Al<sub>2</sub>O<sub>3</sub>. The epitaxial GDC thin films having an average grain size of 80 nm with a polycrystalline structure revealed superior ionic conductivity [18]. Several groups presented columnar GDC thin films with a cubic fluorite structure which had higher ionic conductivity than a 8% bulk YSZ, but had slightly lower ionic conductivity than a 20% bulk GDC [5,6].

The ionic conductivity of lanthanum-doped gallate (LaGaO<sub>3</sub>) with a perovskite structure is higher than that of GDC or YSZ [4,19]. In spite of its superior ionic conductivity, it undergoes gallium volatilization during a sintering process when nickel-based anode materials are used [20]. Strontium and magnesium-doped LaGaO<sub>3</sub> (LSGM) are also used as oxygen ion conductors. During the doping process, Sr and Mg are doped for La sites and Ga sites, respectively [4]. It was also reported that sputtered LSGM thin films have a different atomic concentration compared to the composition of the powder due to the different sputtering rates.

### 1.2.1.2 Pulsed laser deposition

A pulsed laser deposition (PLD) is a thin film fabrication method which uses a focused laser beam, as shown in Figure 1.4. Due to its clustering characteristics, it has a tendency for the chemical composition of the deposited film to be nearly the same as the target [21–23]. This method is commonly used to fabricate multi-component materials such as superconductors [24,25]. The uniformity of thin film deposited by PLD is considerably poor owing to the small active area of its laser plume [26].

YSZ and GDC films were fabricated under different PLD conditions of the chamber background pressure, target-sample (TS) distance, and substrate temperature by Gauckler *et al.* [23,27]. When the oxygen background pressure increased from 0.026 to 0.26 mbar, the surface of the film became more porous. As the substrate temperature increased from room temperature to 900 °C, the crystalline property changed to a polycrystalline structure from an amorphous structure. In particular, 400°C was the threshold temperature of crystallinity change. Without substrate heating, thin films deposited with a shorter TS distance showed better crystalline property because more heat from the laser plume was transferred to the substrate [28]. General YSZ thin films deposited by PLD are columnar structures [23]. Joo *et al.* reported that the activation energy of PLD YSZ thin film is very similar to that of bulk YSZ; they confirmed the activation energy of 0.93~1.10eV for PLD YSZ thin film, whereas that of bulk YSZ was 1.07eV [29]. To verify the substrate dependency in terms of the activation energy, Pt(111), Pt(200) and (001) sapphire were used as substrates to deposit PLD YSZ thin films.

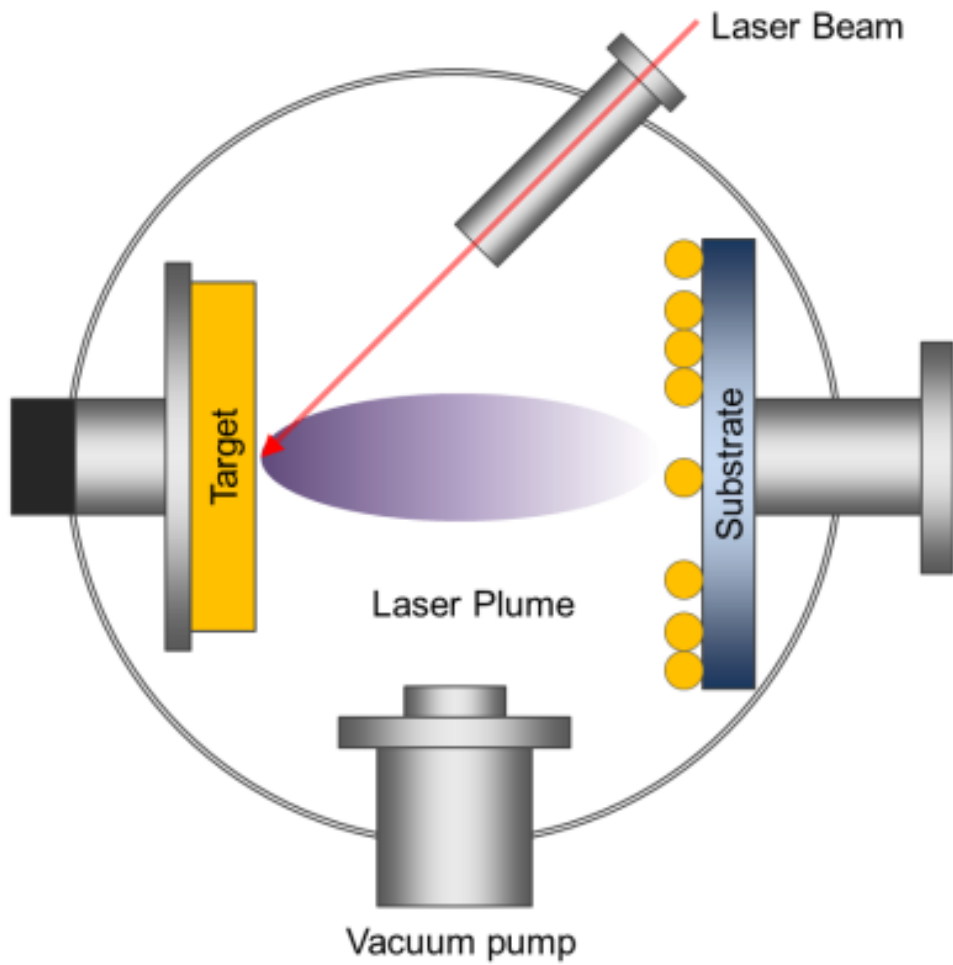


Figure 1.4 Schematic diagram of pulsed laser deposition devices.

The YSZ grain size of these films was 60 and 100 nm, corresponding to Pt(111) and sapphire(0001) substrates, respectively. However, there was no significant difference in the activation energy. The phase was a polycrystalline cubic structure which was identical to that of the bulk form. Heiroth *et al.* showed that 8% YSZ thin film fabricated by PLD had an activation energy of 1.08eV, whereas 3% YSZ thin film had an activation energy of 0.77~0.84eV, which is even lower than the value of 0.92eV for bulk form of 3% YSZ [30]. The 3% YSZ film had better adhesion than the 8% YSZ film, as the deposition was done under an oxygen-deficient condition. As a result, a metastable phase was dominant over the cubic structure [30]. There was a morphology difference in the YSZ thin films according to the substrate types. Rodrigo *et al.* deposited YSZ thin films on steel, Pd/MgO(100), Si(100), and MgO(100) to analyze the crystal structure and microstructure [31]. The YSZ thin films had a (111) oriented cubic structure and porosity of 3-5 % regardless of the substrate type. However, the grain size of the YSZ thin film deposited on Si(100) and MgO(100) was relatively small compared to that of YSZ thin films deposited on steel and Pd/MgO(100). Joo *et al.* investigated activation energy and structural properties of PLD GDC thin films [32]. The activation energy of GDC thin films below 500°C was 0.85eV, which is identical to that of the bulk form. On the other hand, the activation energy above 500 °C was 0.86 eV, which is greater than the value (0.76 eV) of the bulk form. The grain size of GDC thin film deposited on a Pt(111) and a sapphire(0001) substrate was 90 nm and 40 nm, respectively.

### 1.2.1.3 Atomic layer deposition

Atomic layer deposition (ALD) has been applied for fabricating electrolytes of TF-SOFC. ALD is modified chemical deposition method using the successive delivery of gas phase precursors. As shown in Figure 1.5, the deposition procedures are as follows:

Sequence 1: Precursor delivery to the substrate

Sequence 2: Inert gas (such as nitrogen, argon, helium) purging

Sequence 3: Second precursor delivery to the substrate

Sequence 4: Inert gas purging

In sequence 1, organometallic compounds of deposition materials (precursor) are deposited on the substrate and single atomic layer is formed by the chemisorptions of the substrate and precursors. In sequence 2, non-reacted precursors are eliminated by inert gas purging. In sequence 3, a second precursor is exposed to remove the organic ligands of first deposited precursor on the substrate. Finally, the chamber is purged out by inert gas in sequence 4.

One cycle of ALD consists of four sequences with which one atomic layer is deposited theoretically for each step. Therefore, ALD is a self-limiting process, which indicates that the deposition rate of the ALD cycle is constant. Thereby, it is

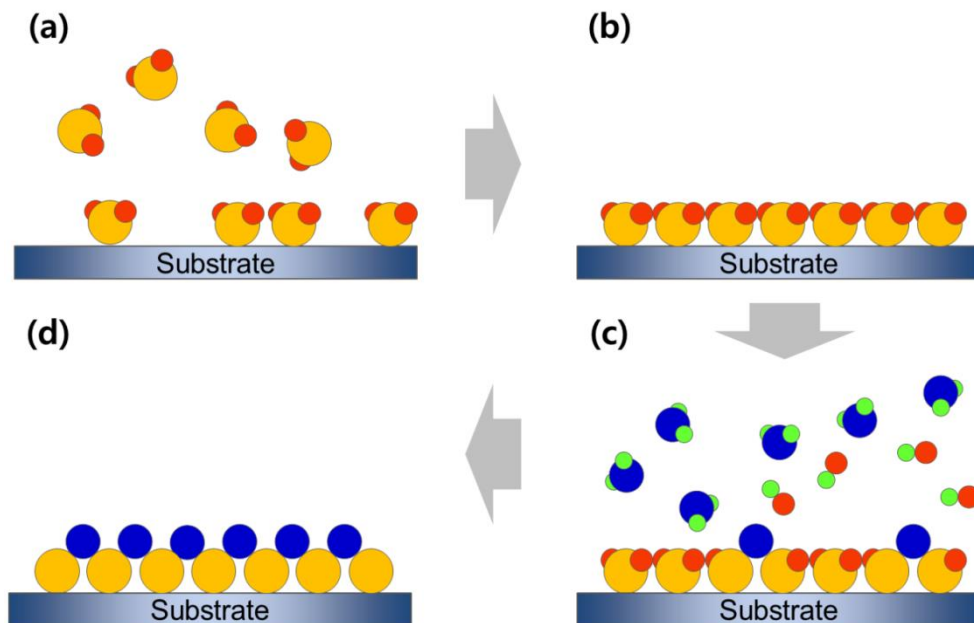


Figure 1.5 Schematic diagram of ALD processes: (a) A precursor delivery to a substrate, (b) purging an inert gas for neutralizing a process chamber, (c) The second precursor delivery to a substrate, (d) purging an inert gas for neutralizing a process chamber.

easy to control the film thickness by calculating the number of ALD cycles [33,34]. Additionally, it has the advantage of uniform and dense deposition on complex structures owing to the chemisorption between the substrate and the precursors. Oxide layers can be easily deposited by the application of ozone,  $H_2O$  or  $O_2$  reactant gases (second precursors).

Research on ZrO<sub>2</sub> and Y<sub>2</sub>O<sub>3</sub> deposition has been reported using ZrCl<sub>4</sub>, ZrI<sub>4</sub>, Cp<sub>2</sub>Zr(CH<sub>3</sub>)<sub>2</sub> and Zr[OC(CH<sub>3</sub>)<sub>3</sub>]<sub>4</sub> precursors and Y(thd)<sub>3</sub>, Y(Cp)<sub>3</sub> and Y(MeCp)<sub>3</sub> precursors respectively [35,36]. Combinations of ZrO<sub>2</sub> and Y<sub>2</sub>O<sub>3</sub> deposition into YSZ were first reported by Putkonen *et al.* using the Y(thd)<sub>3</sub> precursor for Y<sub>2</sub>O<sub>3</sub> deposition and Zr(thd)<sub>4</sub>, Cp<sub>2</sub>Zr(CH<sub>3</sub>)<sub>2</sub>, Cp<sub>2</sub>ZrCl<sub>2</sub> precursors for ZrO<sub>2</sub> deposition [37]. The Y<sub>2</sub>O<sub>3</sub> precursor and ZrO<sub>2</sub> precursor were deposited at a 1:1 cycle ratio. The combination of Y(thd)<sub>3</sub> / Zr(thd)<sub>4</sub> showed a deposition rate of 0.56 Å cycle<sup>-1</sup>, the combination of Y(thd)<sub>3</sub> / Cp<sub>2</sub>Zr(CH<sub>3</sub>)<sub>2</sub> showed a deposition rate of 0.79 Å cycle<sup>-1</sup>, and a combination of Y(thd)<sub>3</sub> / Cp<sub>2</sub>ZrCl<sub>2</sub> showed a deposition rate of 0.89 Å cycle<sup>-1</sup>. The deposition rates were 0.56 Å cycle<sup>-1</sup> for Y(thd)<sub>3</sub> / Cp<sub>2</sub>Zr(CH<sub>3</sub>)<sub>2</sub>, 0.79 Å cycle<sup>-1</sup> for the Y(thd)<sub>3</sub> / Cp<sub>2</sub>Zr(CH<sub>3</sub>)<sub>2</sub>, and 0.89 Å cycle<sup>-1</sup> for the Y(thd)<sub>3</sub> / Cp<sub>2</sub>ZrCl<sub>2</sub>. The impurities of these combinations are 0.4% carbon, 1.7% hydrogen, 0.5% fluorine for Y(thd)<sub>3</sub> / Zr(thd)<sub>4</sub>; <0.1% carbon, 0.13% hydrogen, 0.4% fluorine for Y(thd)<sub>3</sub> / Cp<sub>2</sub>Zr(CH<sub>3</sub>)<sub>2</sub>, 1.1% carbon; and 0.5~1% hydrogen, 0.3% fluorine for Y(thd)<sub>3</sub> / Cp<sub>2</sub>ZrCl<sub>2</sub>. These contamination amounts are within acceptable limits.

The ionic conductivity of ALD YSZ films were reported by Bernay *et al.* and Brahim *et al.* [38,39]. Bernay *et al.* used ZrCl<sub>4</sub> and Y(thd)<sub>3</sub> precursors for 8~9% YSZ and evaluated the ionic conductivity at room temperature [38]. The measured ionic conductivity was 3 x 10<sup>-11</sup> S cm<sup>-1</sup>, which is similar to 7 x 10<sup>-17</sup> S cm<sup>-1</sup> and 1.13 x 10<sup>-12</sup> S cm<sup>-1</sup> compared to previous research on bulk YSZ [38]. Because the operating temperature of a SOFC is considerably higher than room temperature, an evaluation of the ionic conductivity at an elevated temperature is required. Brahim *et al.* measured the ionic conductivity at 400°C using CpZrCl<sub>2</sub> and Y(thd)<sub>3</sub>

precursors for 9~11%  $\text{Y}_2\text{O}_3$ -doped YSZ film [39]. The evaluated ionic conductivity and activation energy were  $1.66\sim 4.52 \times 10^{-4} \text{ S cm}^{-1}$  and 0.3 eV, respectively which are least three times lower than the bulk values. Ginestra *et al.* fabricated 3% YSZ whose doping rates were lower than the typical doping rate of 8~10% and measured the ionic conductivity at 800°C. 3% YSZ deposited by ALD showed a tenfold higher value of ionic conductivity compared to that of 3% bulk YSZ [40]. This result is similar to sputtered YSZ, where the phase shift of nanofabricated YSZ according to the  $\text{Y}_2\text{O}_3$  doping rate can differ from the bulk status [14]. Without an extra heat treatment, the crystal structures of ALD films are reported as amorphous or polycrystalline. In the case of polycrystalline film, both cubic and tetragonal structures are observed. There are numerous variables in the ALD process such as the substrate material, the process temperature and the precursor type. Therefore, additional research is required to verify the relationships between these variables with clarity.

### 1.2.2 Overview of thin film SOFC structure

Yet there has been numerous structures of SOFCs by thin film applications reported, two major structure of thin film SOFCs attract researchers. The first structure is the free standing membrane on silicon-wafers (Figure 1.6 (a)). It is a structure of electrolyte on a silicon wafer and then, wafer is partially etched with etchant such as KOH to expose the surface of electrolytes. Then, electrode is deposited on the exposed surfaces. Smooth and uniform silicon wafer allows thin film electrolyte (<100nm) thus, performance is highest among other structures. However, it has problem of a mechanical strength of free standing electrolytes and electrodes, so active cell area is usually less than 100um x 100um [13].

The second structure is thin film SOFC on palladium film (Figure 1.6 (b)). Palladiums are hydrogen permeable material even in the bulk status, and it has high catalytic activity towards HOR reactions. Therefore simple thin film SOFCs can be fabricated by depositing thin film electrolyte and cathode on palladium sheet. However, it has problem of durability since volume of palladiums are gradually change during hydrogen penetration.

The third structure is thin film SOFC on porous substrates which is similar structure to conventional anode supported SOFCs (Figure 1.6 (c)). The difference between the conventional anode supported SOFCs and thin film SOFC on porous substrate is thickness of components. It has advantages of mechanical strength, because thin electrolyte and electrodes are supported by porous substrate. However, there is limitation of electrolyte thickness due to the roughness of porous substrates.

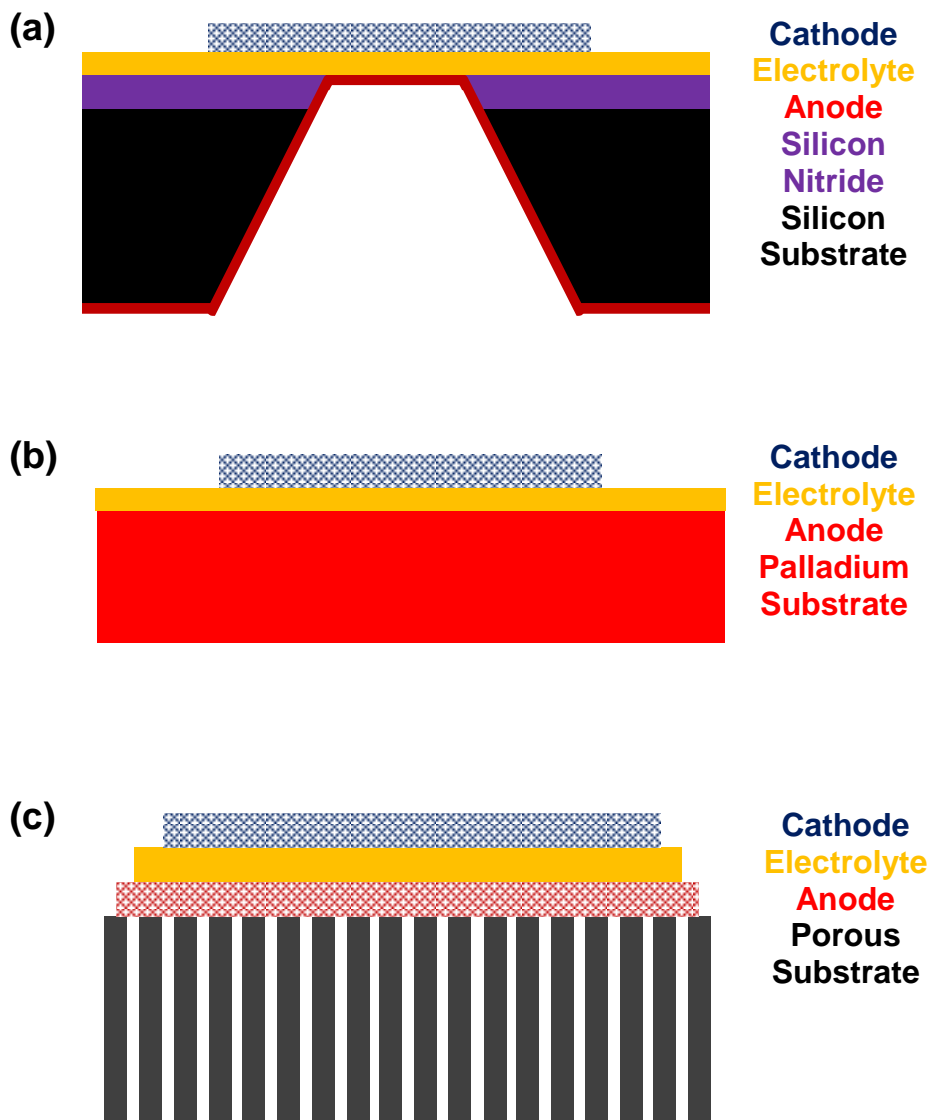


Figure 1.6 (a) Thin film SOFC structure of free-standing membrane, (b) thin film SOFC on hydrogen permeable palladium substrates, (c) thin film SOFC on porous anode substrates.

Usually the thickness of thin film electrolytes on porous substrates using porous substrates are between 500nm~3um [13,41,42].

Summary to above structure, it is important to fabricate thin film SOFCs which has thin electrolyte as possible with high mechanical strength and cell with large active area.

### 1.3 Single chamber operation of SOFCs

The modern concept of single chamber SOFCs is introduced by Hibino et al. at 2000 [43] and it used gas mixture of fuel and oxidant and delivered to the whole cell area without gas separators (1.7 (b)). In the case of conventional SOFCs, fuels and oxidants are separately delivered to an anode and a cathode respectively by separators to prevent mixing (1.7 (a)). Using gas separators are obvious for operating fuel cells, because mixture of fuels and oxidants can cause explosion and leakage of currents and voltages. To avoid these problems, single chamber operation of fuel cells uses selective catalyst on anodes and cathodes to prevent leakage of currents and voltage. For the anode materials, it has to be actively participated toward oxidation reaction of fuels, but catalytically inert to reduction reactions of oxidants. On the other hand, cathode materials have to be catalytically active towards oxidants reduction reactions, but inert to the oxidation reaction of fuels. The voltages and currents of single chamber operations are generated by the selective catalytic electrochemical reactions [44]. To avoid explosion of fuel and oxidant mixture, fuel cells are operated under gas mixing ratio below lower flammability limit and above upper flammability limit.

Single chamber operation of fuel cells has advantages of allowing various structures, independent toward electrolyte density and extra heat generation by exothermic reaction of partial oxidation reaction at anodes. On the other hand, single chamber operating conditions are forced at low efficient regime to avoid explosion of fuel and oxidant mixture. The selective catalysts for single chamber operation has to be more developed, since open circuit voltage are lower than that

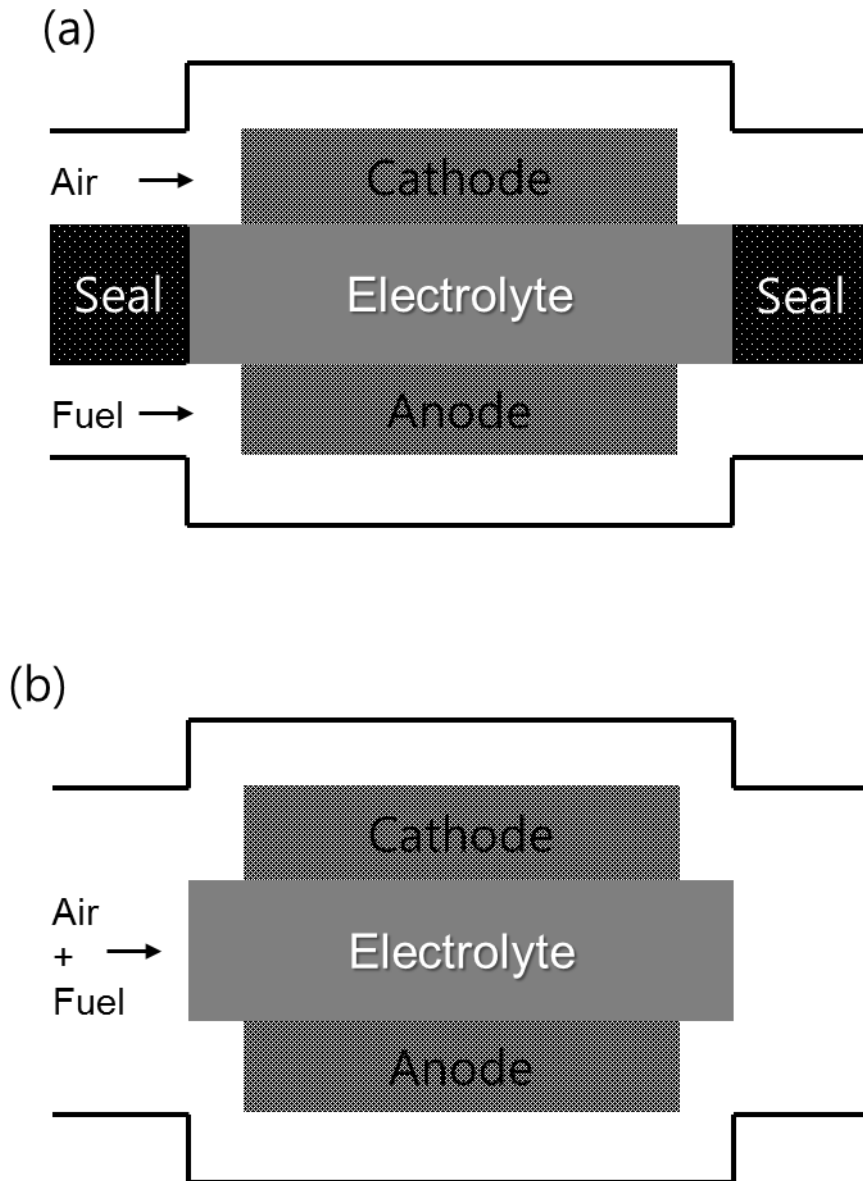


Figure 1.7 Schematic diagram of (a) dual chamber operation with gas separators and seal, (b) single chamber operation using mixture of air and fuel to the entire cell.

of dual chamber operation. The advantages and disadvantages of single chamber operation are listed at table 1.1 [44].

Table 1.1 The advantages and disadvantages of single chamber operation of SOFCs.

<b>Advantages</b>	<b>Disadvantages</b>
<ul style="list-style-type: none"> <li>■ Sealing and separator free design</li> <li>■ Less complex gas manifolding</li> <li>■ Convenient stack assembly</li> <li>■ Potential for miniaturization</li> <li>■ No need for gas-tight electrolyte</li> <li>■ Various cell designs</li> <li>■ Easier cell fabrication</li> <li>■ Compact and simplified designs</li> </ul>	<ul style="list-style-type: none"> <li>■ Development of highly selective and active catalysts</li> <li>■ Low efficiency by non-electrochemical reactions and limited operation conditions to avoid explosions.</li> <li>■ Low fuel utilization</li> <li>■ Risk of explosion by fuel and air mixture at high temperature.</li> </ul>

Although there are several issues to be improved for single chamber operation of SOFCs, it still attracts the researchers. The main reason is relatively emancipated structure due to the separator-free design. There are several designs with conventional structures, co-planar structures and all porous structures (Figure 1.8). The conventional structures are same to the dual chamber design without

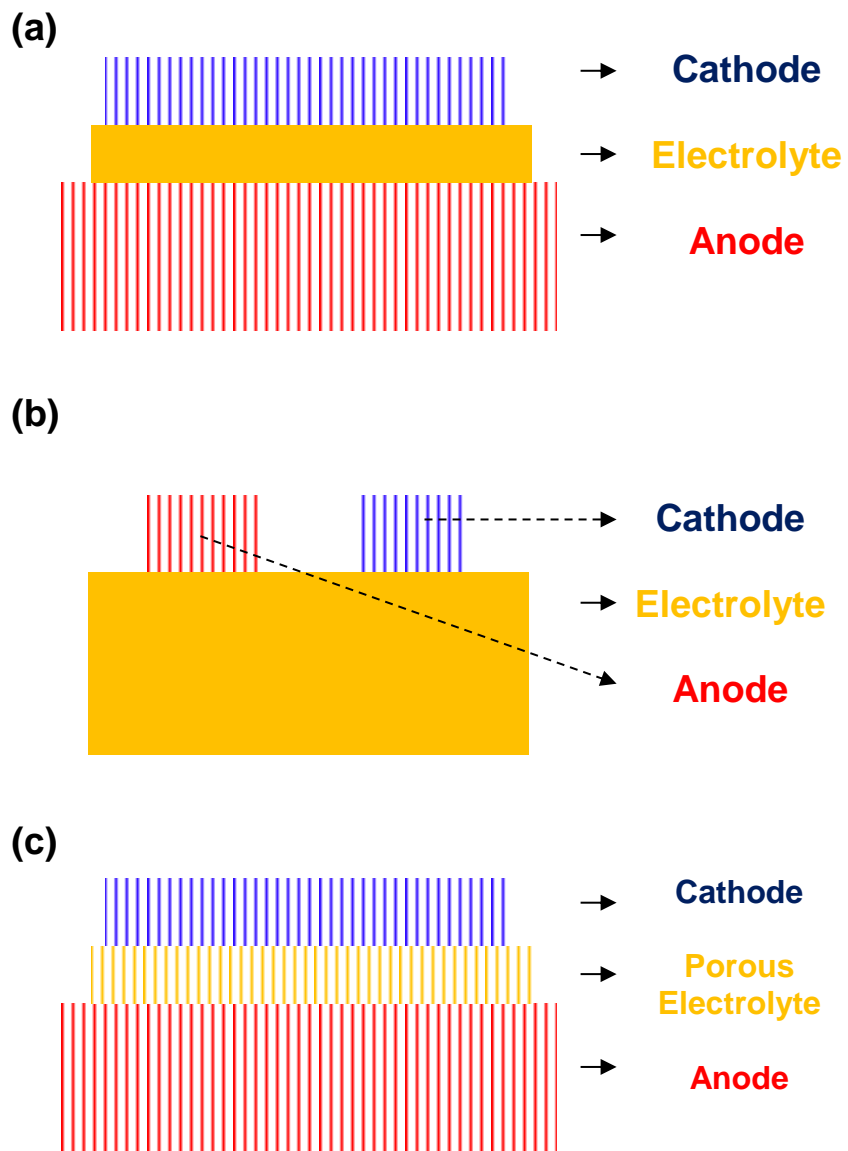


Figure 1.8 Designs of single chamber SOFCs. (a) Conventional, (b) co-planar and (c) all porous structure.

sealing and separators. It has advantages of allowing conventional cell fabrication technics and allowing anode, electrolyte and cathode supported design. Also performance could be enhanced by applying thin film electrolytes on electrodes supported design. The one thing special of co-planar structures is fabrication of electrodes on the same side of electrolytes (Figure 1.8 (b)). It has advantages of high voltage using just one electrolyte due to the fabrication of multiple electrode arrays. The design of figure 1.8 (c) is all porous structures using porous electrolytes. In this case, the performance is higher than that of using dense electrolyte due to the uniform flow of the gases. In this case, generated hydrogen at anodes easily penetrates through the cathodes causing the low open circuit voltage.

The anode reactions of single chamber SOFCs are basically partial oxidation of fuel by oxidants.



The equation (1.1) and (1.2) are partial oxidation reaction of fuel and (1.3) is electro catalysis of fuel oxidation. Through (1.1) and (1.2), hydrocarbons are changed into hydrogen which fuel cell can be used as a fuel. In case of the cathode,

it uses conventional oxygen reduction reaction if the cathode materials have selective catalysis.

It is important to choose the anode materials of single chamber SOFCs to secure the selective catalytic reaction. The former researchers used platinum as anodes, but it showed low open circuit voltage and performance. The performance and open circuit voltages of single chamber SOFCs are gradually improved by Hibino et al [43]. The Ni-SDC anode showed  $450\text{mW/cm}^2$  of power density at  $600^\circ\text{C}$  and after this paper, Ni based anodes are dominantly used. In case of using Ni-ceria based cermet such as Ni-SDC and Ni-GDC, the cell was properly operated under ethane, propane and butane at  $500^\circ\text{C}$ , but partial oxidation methane was not occurred in this temperature [45]. To operate the cell under single chamber operation using methane fuel, Hibino et al mixed small amount of PdO into Ni-ceria based cermet. The cell using small amount of PdO in anode showed 0.9V of open circuit voltage while pure Ni-ceria based cermet showed 0.1V of open circuit voltage. A ruthenium is also applied to the anode and it prevented carbon deposition and re-oxidation of the nickel.

In case of cathode materials, SSC was widely used after Hibino et al. [43] applied to the single chamber SOFCs and showed high performance. It is known that perovskite materials such as LSM, LSCF, BSCF are suitable for single chamber SOFCs. The sintering and operating temperatures are more sensitive to the performance due to the catalytic activity towards fuels [44]. The cathodic catalytic activity is only associated to the oxygen reduction reactions in the dual chamber operation, however, single chamber operation has to consider cathodic

catalytic activity toward anode gas. Thus, the factor influencing to the cathodic catalytic activity such as sintering temperature and operating temperature has to be carefully controlled.

The current collecting materials are also important factors to the single chamber SOFCs. The dual chamber cell usually use nickel or platinum mesh on the anode side, and platinum mesh on the cathode side. However, to maintain the selective catalytic activity of single chamber SOFCs, gold is widely used and platinum is only used in the anode side [44]. Using platinum as an anode current collection has advantages of accelerating partial oxidation reaction, thus cell temperature was higher than that of using gold as a current collecting material. The gold current collector is inert to the exothermic partial oxidation reactions, so we cannot expect the performance improvement. However, it has advantages of finding a clear tendency of the cell performance, because there are lesser factors influencing the cell performance. The cell operation is limited to under 800°C, while nickel-gold eutectic material can be generated and it has a poor catalytic activity towards anode reactions.

Single chamber operation of SOFCs has a possibility of explosion since it uses a gas of fuel and oxidants mixture. To prevent the explosion, the operating conditions are in above upper flammability limits and below lower flammability limits. In case of using methane as a fuel, it has lower flammability limits of 5% and upper flammability limits of 15% at the standard temperature and pressure condition (25°C, 1atm). The lower flammability limits and upper flammability limits linearly increases (equation (1.4)) and decreases (equation (1.5)) respectively,

while increasing operating temperature.

$$\text{LFL}(T) = \text{LFL}(25^\circ\text{C}) - \frac{0.75}{\Delta H} (T - 25^\circ\text{C}) \quad (1.4)$$

$$\text{UFL}(T) = \text{UFL}(25^\circ\text{C}) + \frac{0.75}{\Delta H} (T - 25^\circ\text{C}) \quad (1.5)$$

The flammability limits are often expressed as a different form such as  $R_{\text{mix}}$ .  $R_{\text{mix}}$  expresses the amount of hydrogen in the oxygen (equation 1.6).

$$R_{\text{mix}} = \frac{\text{Hydrocarbon}}{\text{O}_2} \quad (1.6)$$

The figure 1.9 illustrates the explosion range as a function of high flammability limits and low flammability limits. Through experimental results, single chamber SOFCs usually operated in range of 1.5 to 2.0 of  $R_{\text{mix}}$  value.

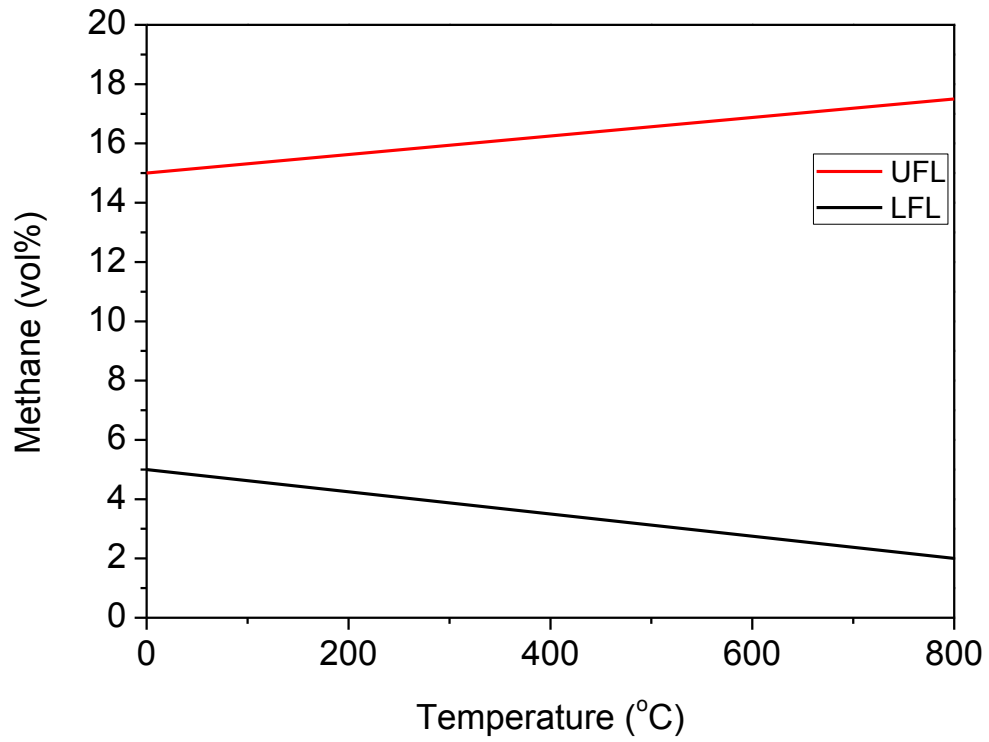


Figure 1.9 The upper flammability limit and lower flammability limit of methane as a function of temperature.

## Chapter 2 Thin film application to solid oxide fuel cells

(“Reproduced *The Journal of Power Sources* 307 (2016) 289-296”)

### 2.1 Thin film application to solid oxide fuel cell electrodes.

#### 2.1.1 Introduction

Solid oxide fuel cells (SOFCs) have the potential for being next-generation energy conversion devices due to their high energy conversion rates and clean emissions [1]. However, they require a high operating temperature above 800 °C due to the low ionic conductivity of the ceramic electrolyte and the sluggish surface kinetics of the electrode materials [2]. An operating temperature between 300 °C and 500 °C allows high system stability, fast start-up, convenient sealing, and the use of various materials. Several methods have been introduced to lower the operating temperature through new structures[13,21,26,46–48] and materials [8,34,49,50,42,51–53] Using a nano-fabrication technique for the electrode and electrolyte allows thin film electrolytes and maximum triple phase boundary (TPB) density of the electrode/electrolyte interface, which strongly affects the fuel cell performance enhancement [1].

Several electrode materials and their structures for low temperature operation have been presented to date [8,13,21,26,34,46–50,42,51–53]. However, cathode material is still the main bottleneck because conventional mixed conducting oxides for high temperature SOFC electrodes such as  $\text{La}_{1-x}\text{Sr}_x\text{Co}_{1-y}\text{Fe}_y\text{O}_3$  (LSCF),  $\text{La}_{1-x}\text{Sr}_x\text{MnO}_3$  (LSM),  $\text{La}_{1-x}\text{Sr}_x\text{CoO}_3$  (LSC),  $\text{Sm}_{1-x}\text{Sr}_x\text{CoO}_3$  (SSC), and  $\text{Ba}_{1-x}\text{Sr}_x\text{Co}_{1-}$

$\lambda\text{Fe}_y\text{O}_3$  (BSCF) show significantly poor catalytic activities and electronic conductivities in the low operating temperature (300 °C–500 °C) [54]. As the cathode oxygen reduction reaction requires higher activation energy than the hydrogen oxidation reaction, a noble metal catalytic electrode such as platinum (Pt) is still the best material for the cathode of low temperature solid oxide fuel cells (LT-SOFCs) as well as polymer electrolyte fuel cells (PEFCs). Pt electrodes used for LT-SOFCs are usually fabricated using thin film fabrication techniques based on physical vapor deposition (PVD). Thin film fabrication techniques are used because they can help easily control the grain and pore structures of the electrode on the nanometer scale [8]. Metal electrodes for LT-SOFCs usually have highly porous nanostructures that provide an increased supply of gas and TPB. However, due to the high surface area of a nano-porous structure, the nanofabricated thin film electrode has poor thermo-mechanical stability, which results in rapid structural and performance degradation [55]. According to previous research of LT-SOFCs [34,42,56], performance degradation results mainly from the microstructural coarsening of thin-film Pt electrode. Even though the operating temperature of LT-SOFCs is far lower than that of typical SOFCs, coarsening occurs within a few hours. As the overall reactions of a fuel cell are highly exothermic especially in the high current regime, a similar phenomenon is observed with PEFCs even though the operating temperatures of PEFCs are generally below 100 °C. Thus, using Pt as an electrode material for the development of fuel cells is still challenging regardless of the operating temperature.

In metallurgical research areas, dispersion hardening is one of the most

effective methods used to enhance the heat resistance of metals [57]. Uniform dispersion (~1% by weight) of thermally stable oxide nanoparticles (<50 nm) in metals provides thermal stability by preventing microstructural deterioration [58]. In the case of Pt hardening, zirconia and rhodium are commonly utilized for the dispersion particles. According to Zhang et al., Pt alloys that contain both yttrium (Y) and zirconium (Zr) have decent thermal stability. While the microstructures of pure Pt changed at 450 °C [59], the microstructures of Pt, Y, and Zr alloys maintained at 1,200 °C for over 100 hours.

Thermal barrier coatings are also used for preventing the thermal deterioration of a metal. They use plasma spraying deposition for coating stable ceramic materials such as zirconia or alumina [60]. Usually, dispersion hardening and thermal barrier coatings are used for the bulk materials[57–60].

This paper presents a platinum-based composite electrode that was synthesized using nanofabrication. First, we investigated the thermal stability of the electrode structure that was fabricated using both dispersion hardening and a thermal barrier coating. We used a sputtering system instead of the conventional methods discussed above. The Pt-ceramic composite electrodes were fabricated with various ratios to find the optimal value, and their microstructures were investigated to evaluate the thermal stability. Last, the electrochemical characterizations were performed using these electrodes as fuel cell cathodes. We used gadolinium doped ceria (GDC) as a dispersion and thermal barrier coating material. Numerous studies have demonstrated that applying doped ceria to the interface of an yttria-stabilized zirconia (YSZ) electrolyte and Pt cathode decreases

the reaction resistance. Furthermore, the composite structure of Pt and GDC would generate a mixed ionic electronic conductor (MIEC) path as doped ceria is a highly ionic conducting material.

### 2.1.2 Experimental

Figure 1 illustrates the Pt and GDC nanocomposite electrodes that were fabricated using a thermal barrier coating and the dispersion hardening methods. The background pressure of the sputter chamber was maintained at 6.66 Pa (50 mTorr) by a continuous flow of argon gas. The electrodes for the thermal barrier coating were fabricated by sequential deposition of Pt and GDC. The electrodes for dispersion hardening were fabricated by simultaneous deposition (co-sputtering) of Pt and GDC. The deposition parameters for the thermal barrier-coated samples and the dispersion-hardened electrode samples are listed in Tables 1 and 2, respectively. We modified the deposition time to maintain a uniform thickness (~150 nm). These electrodes were applied to the fuel cell and operated at 500 °C for an hour at a heating rate of 6 °C min<sup>-1</sup> and were observed for any morphological changes. Scanning electron microscopy (Zeiss Supra 55VP, Carl Zeiss, Germany) was used to obtain surface images of the electrodes.

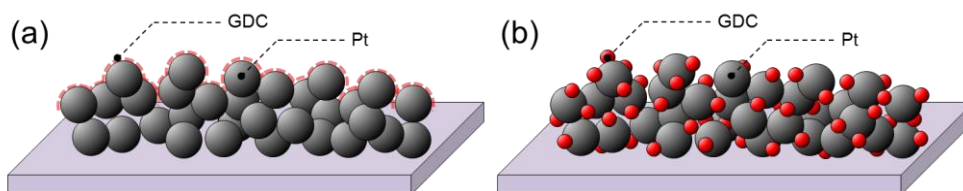


Fig. 2.1 Schematic image of (a) the thermal barrier GDC coating on a Pt electrode and a (b) dispersion-hardened Pt / GDC obtained by co-sputtering.

Table 2.1 Deposition parameters of the thermal barrier GDC coated Pt electrodes

	<b>Pt power</b>	<b>GDC power</b>	<b>Time</b>
<b>5 nm-GDC coated on 150 nm Pt</b>	100 W	50 W	10 min Pt , 6 min GDC
<b>10 nm-GDC coated on 150 nm Pt</b>	(15 nm min <sup>-1</sup> )	(0.8 nm min <sup>-1</sup> )	10 min Pt , 12 min GDC

Table 2.2 Deposition parameters of dispersion-hardened Pt and GDC co-sputtered electrodes

<b>Samples with vol%</b>	<b>Pt power</b>	<b>GDC power</b>	<b>Time</b>
<b>Pt 100%</b>	100 W (15 nm min <sup>-1</sup> )	0 W	10 min
<b>Pt 95% / GDC 5%</b>		50 W (0.8 nm min <sup>-1</sup> )	9 min 30 sec
<b>Pt 90% / GDC 10%</b>		100 W (1.6 nm min <sup>-1</sup> )	9 min
<b>Pt 80% / GDC 20%</b>		210 W (3.05 nm min <sup>-1</sup> )	8 min

To fabricate the fuel cell sample, the Pt/GDC composite cathode and NiO anode were deposited on both sides of the 500-um-thick YSZ disk electrolyte. Performance measurements of the samples were conducted at a measurement temperature of 500 °C using a custom-made test station. Pure dry hydrogen was supplied to the anode side while the cathode side was exposed to air for natural oxygen supply. The electrochemical characterization was conducted using a Solartron 1287 electrochemical interface and a 1260 impedance analyzer.

### **2.1.3 Results and discussion**

#### **2.1.3.1 Thermal stability of the Pt-based nanocomposite electrode**

Surface SEM images of the GDC thermal barrier coating on Pt electrodes are presented in Fig. 2. As mentioned above, the pure Pt electrodes underwent significant morphological changes at the elevated temperature due to agglomeration. Compared with the pure Pt electrode, the thermal barrier coated electrodes showed superior thermal stability with the thin GDC layer. In the case of the conventional bulk thermal barrier coating, the layers are much thicker (um-mm scale) compared to our research [60]. For current collection on the cathode side, ceramic coatings that are a few nanometers thick are allowed for us. So we are concerned that the prevention of heat transfer of the thin oxide layer (~5–10 nm) would be less effective and limited at the surface. Since the total thickness of the electrodes was thin (~150 nm), the prevention of surface coarsening was maintained the entire nanostructure. The FE-SEM results of the morphology

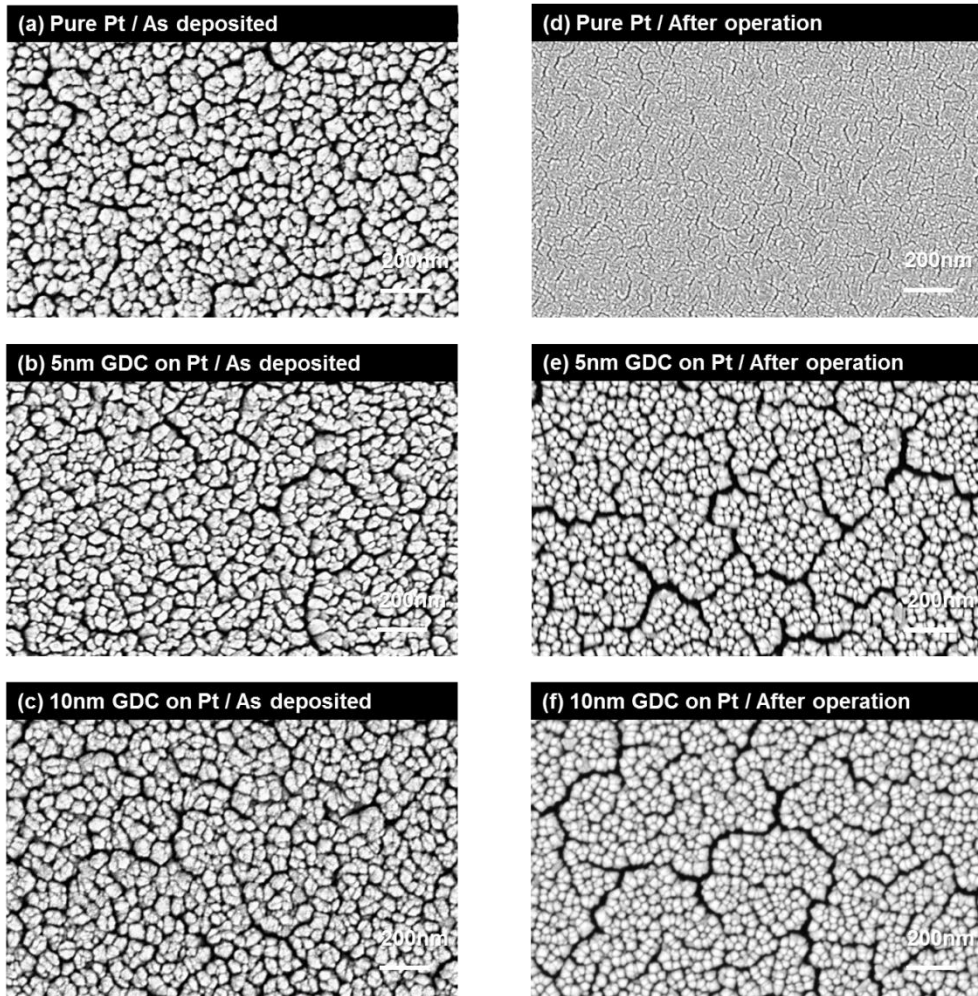


Fig. 2.2 Surface SEM images of the pure Pt and thermal barrier GDC coating on Pt.

Electrodes of before [(a)Pure, (b)5nm-GDC coated, (c)10nm-GDC coated] and after [(d)Pure, (e)5nm-GDC coated, (f)10nm-GDC coated] operating at 500°C for an hour.

analysis of GDC coated Pt indicate that the thermal barrier coating with a thin oxide layer (a few nanometers thick) can be used for thin film nanostructures.

Figure 3 presents the surface images of the dispersion-hardened Pt and GDC nanocomposite electrodes before and after operation (heated 500°C at 1 hour). Electrodes with different Pt and GDC ratios are fabricated by applying different sputtering powers. The dispersion-hardened samples also showed superior thermal stability and did not undergo significant morphological changes regardless of the GDC to Pt ratio in the range of 5~20%. This signifies that GDC matrices hinder the movement of Pt and dispersion hardening could also be used for nanostructures. The 90% Pt / 10% GDC (Fig. 3(b)) and 80% Pt / 20% GDC (Fig. 3(c)) samples have higher surface areas due to their relatively smaller grain sizes, which increase heat absorption. However, they showed good thermal stability.

As the ratio of GDC was increased from zero vol% to 20 vol%, there was a significant difference in the surface morphologies. In the case of the high Pt containing samples (pure Pt and 95% Pt / 5% GDC), grains were aggregated with irregular shapes and nano-pores were created around the clusters. On the other hand, the grains of the relatively low Pt containing samples (90% Pt / 10% GDC and 80% Pt / 20% GDC), showed a regular and independent distribution of grain. It is reported that the formation of clusters (Pure Pt and 95% Pt / 5% GDC) requires a driving force such as thermal energy [19]. In our case, the driving force would be generated during the deposition process since no additional energy was created after the deposition. Plasma heat is the only driving force that can provide particles into high energy during the sputtering process. When the particles with high energy

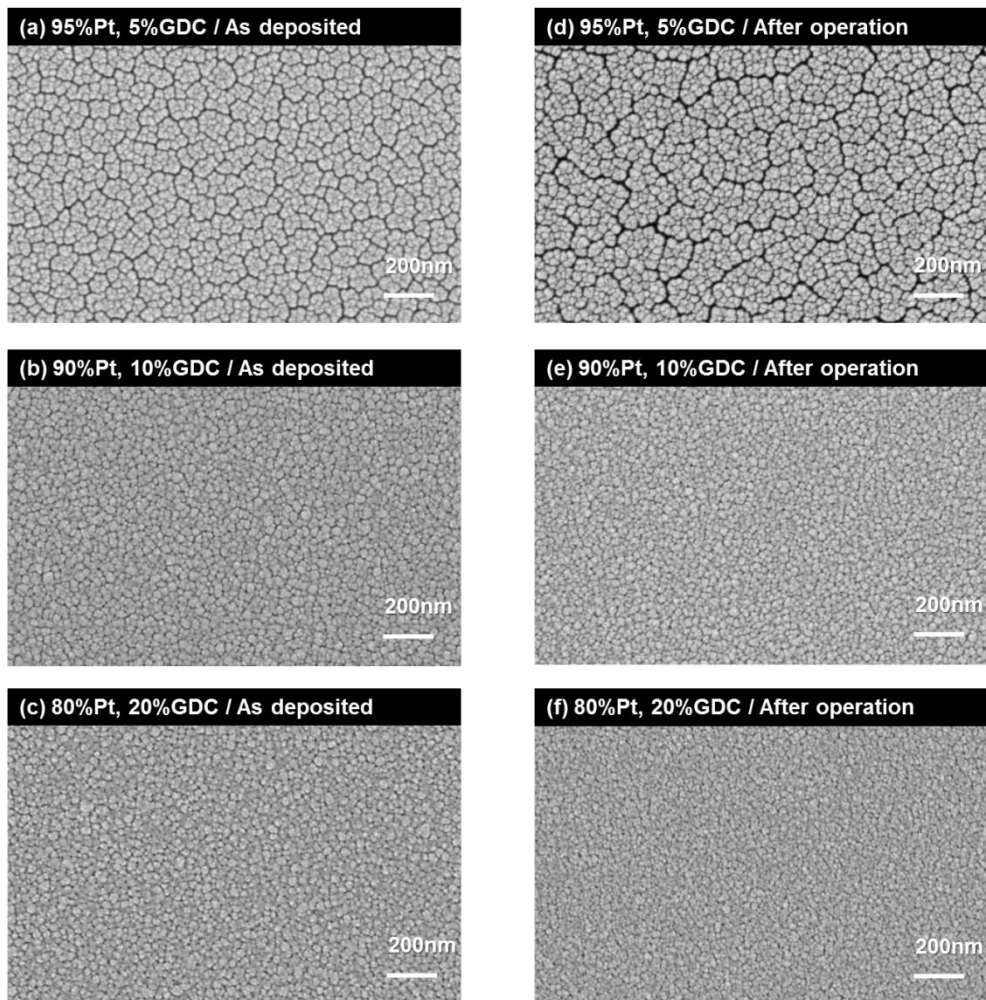


Fig. 2.3 Surface SEM images of dispersion hardened Pt – GDC electrodes by co-sputtering. Electrodes of before [(a)95% Pt / 5% GDC, (b)90% Pt / 10% GDC, (c) 80% Pt / 20% GDC] and after [(d)95% Pt / 5% GDC, (e)90% Pt / 10% GDC, (f) 80% Pt / 20% GDC] operating at 500°C for an hour.

arrive at the surface of the substrate, they tend to move and aggregate with nearby particles to minimize their free energy [61]. Thus, high Pt containing electrodes (Fig. 2(a) and Fig. 3(a)) show large sized pores located around clusters, which indicates the movement and aggregation of grains. The low Pt containing samples (Fig. 3(b) and (c)), however, have relatively smaller pores and individual grains. Individual grains are observed because the higher concentration of stable oxide particles prevents the generation of clusters by suppressing the movement of grains.

### **2.1.3.2. Cell application and electrochemical analysis**

To investigate the relationship between microstructures and electrochemical properties, fuel cells were fabricated and tested. To eliminate the factors – other than the composite cathode – that affect cell performance, thick commercial (500  $\mu\text{m}$ ) YSZ pellets and NiO were used as the electrolyte and anode, respectively. Figures 4 and 5 show the fuel cell current-voltage (I-V) measurement of each electrode at initial and after 1 hour, respectively. In both cases, the peak power densities of Pt and GDC composite electrodes improved considerably compared with that of pure Pt.

According to the initial fuel cell performance (Fig. 4 (a)), thermal barrier coated electrodes achieved better performance than pure Pt electrodes regardless of thickness. Because the as-deposited morphology of these three electrodes is nearly identical and the interface between Pt and electrolytes is the same, we believe that the slight difference in performance is due to the coarsening of Pt by thermal

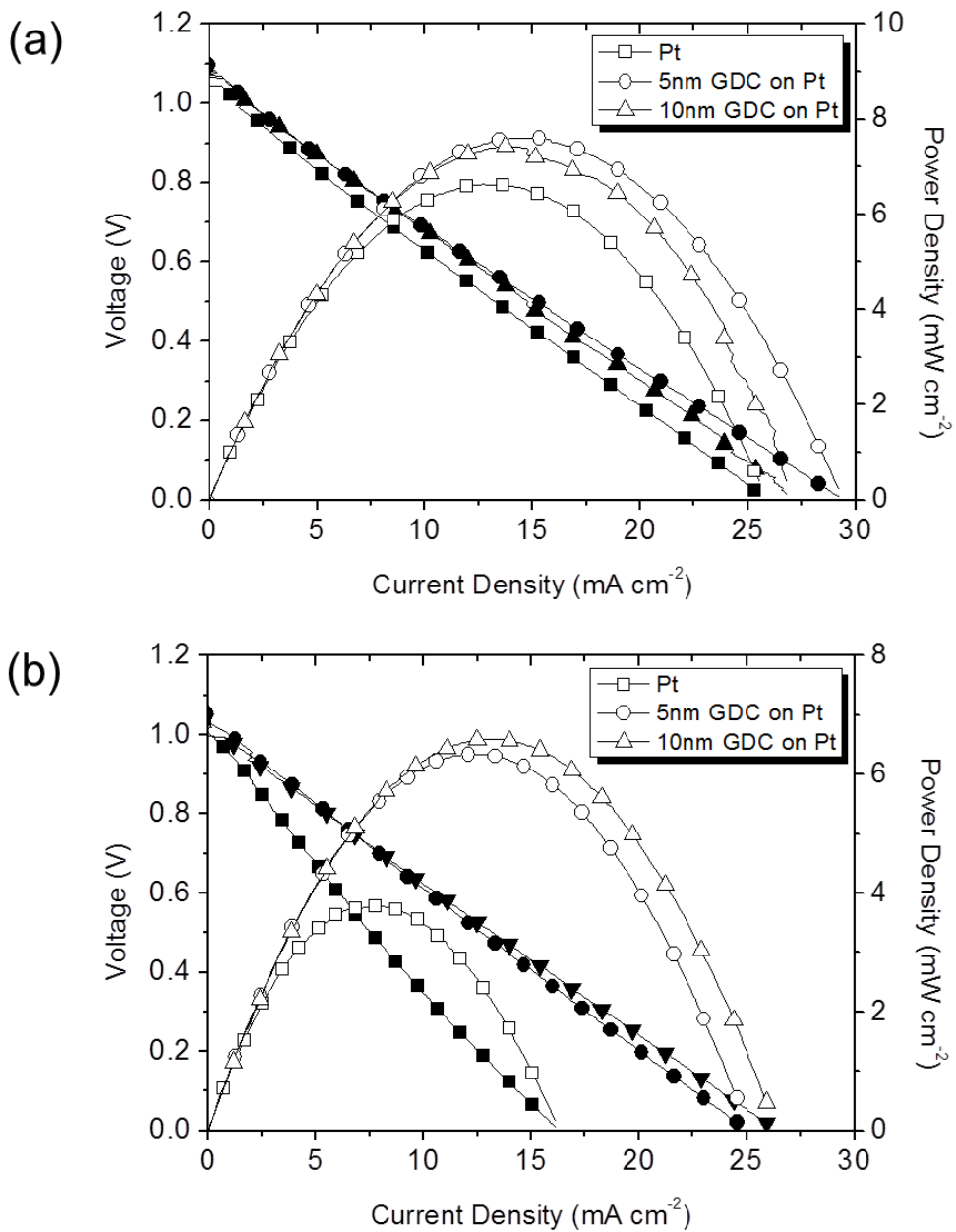


Fig. 2.4 (a) Initial and (b) 1 hour after I-V behaviors and power densities of thermal barrier GDC coating on Pt electrodes at 500 °C.

energy during temperature elevation of furnace. It is reported that the morphology of the nanostructured Pt can change even at 400 °C [56]; therefore, the coarsening of the pure Pt sample could occur before the furnace reaches 500 °C . After 1 hour of fuel cell operation, the performance of the pure Pt electrode showed nearly half of its initial peak power density while the GDC coated Pt electrodes showed only about 10–15% degradation. Additionally, the 10-nm-GDC coated Pt electrode showed better thermal stability since the surface concentration of stable oxide is higher than that of the 5 nm-GDC coated Pt electrode.

In the case of Pt and GDC co-deposition (Fig. 5), ion conducting GDC would function as a mixed electronic and ionic conductor. Also, according to previous research [62–64], the surface oxygen kinetics of the GDC/Pt interface were superior to those of the YSZ/Pt interface due to high surface exchange coefficient of GDC. Thus, the composite electrode of Pt and GDC would reduce the cathodic polarization resistance by enhanced oxygen reduction kinetics. Therefore, the co-sputtered electrodes of Pt/GDC had a higher peak power density than the GDC thermal barrier coated Pt electrodes. Among the dispersed hardened electrodes, the 95% Pt / 5% GDC electrode had the highest peak power density while the 90% Pt / 10% GDC and 80% Pt / 20% GDC electrodes had similar values. Compared with the other Pt and GDC co-sputtered electrodes, the 95% Pt / 5% GDC electrode has larger pores and a higher porosity, which leads to an increase in the TPB density and gas supply. Thus, the performance differences between the samples are mainly due to the microstructures of the electrodes. Detailed information of the cell performance is provided in Table 3.

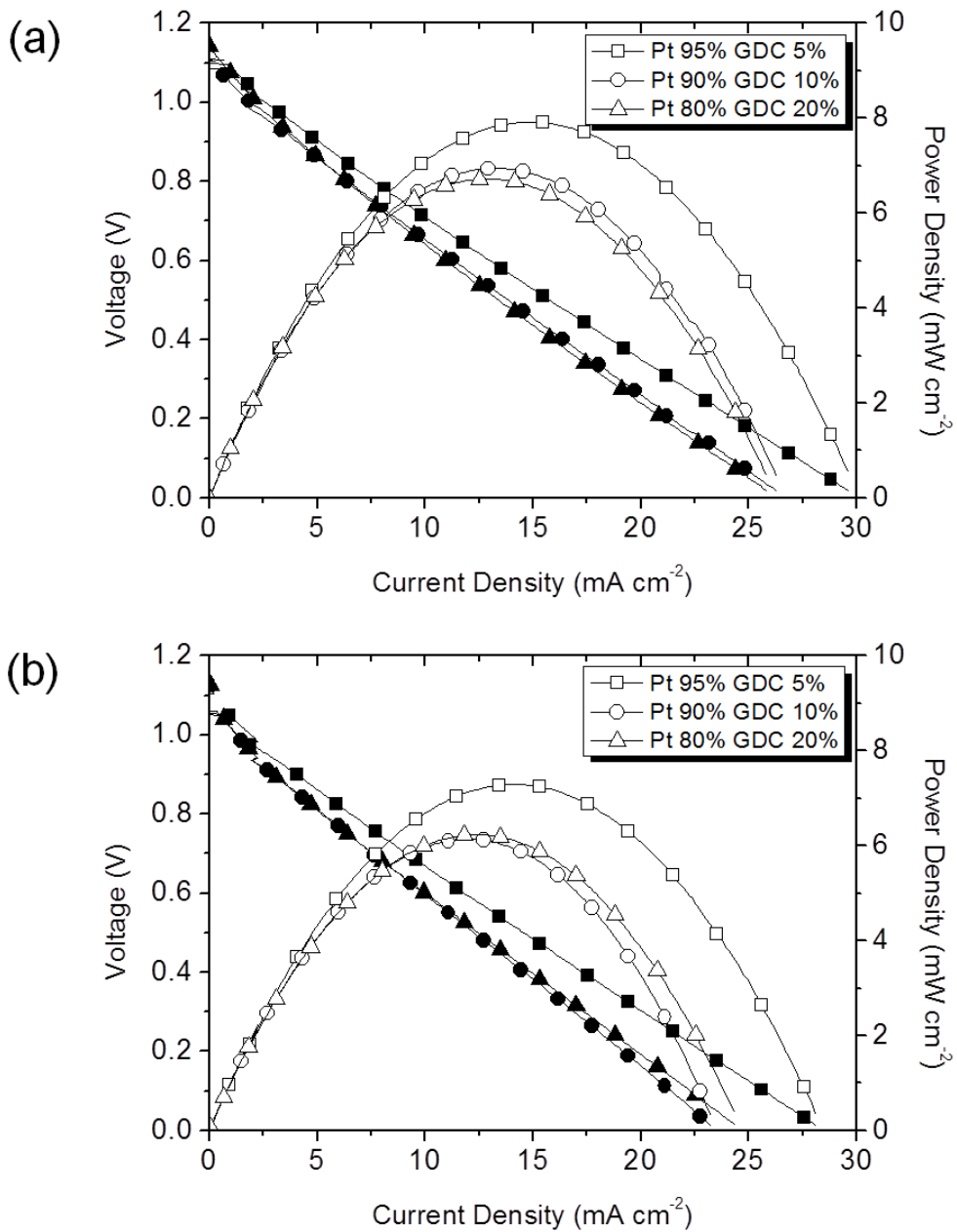


Fig. 2.5 (a) Initial and (b) 1 hour after I-V behaviors and power densities of dispersion-hardened Pt / GDC co-sputtered electrodes at 500 °C.

As shown in Table 3, the peak power density of the cells decreased by about 7–43% after 1 hour of operation at 500 °C. The SEM images clearly show that the pure Pt electrode suffered severe structural degradation. The cell performance decreased by about 43% mainly due to the loss of porosity and reduced TPB density which was caused by coarsening. Previously, a similar result was reported in which the peak power density decreased by about 50-60% when a pure Pt electrode was used and operated at 500 °C [55] for an hour.

To further evaluate the different cell performances and degradation factors, electrochemical impedance spectroscopy (EIS) data was obtained (Table 4). First, we concerned about the reliability of EIS data, since performance degradation could occur during EIS measurement. Reason of the degradation could be predicted by observing FE-SEM images of the electrodes, but the precise reason of degradation cannot be explained without the EIS data.

Since the ohmic resistances of all the cells were between 24.5 ohm cm<sup>2</sup> and 25.0 ohm cm<sup>2</sup>, we normalized the x-axis by eliminating the ohmic resistance value for convenient comparison. Furthermore, EIS measurements were performed in the frequency range of 2 MHz to 2 Hz at 0.5 V to observe the reaction resistance at the electrode/electrolyte interface, and we compared the I-V and EIS data. The tendencies of the peak power density and reaction resistance seem to be similar. The performance improved mainly because of the reduced electrode interface resistance, as expected. The 95% Pt / 5% GDC sample showed the smallest reaction resistance and degradation percentage, while pure Pt sample showed the highest resistance and degradation percentage.

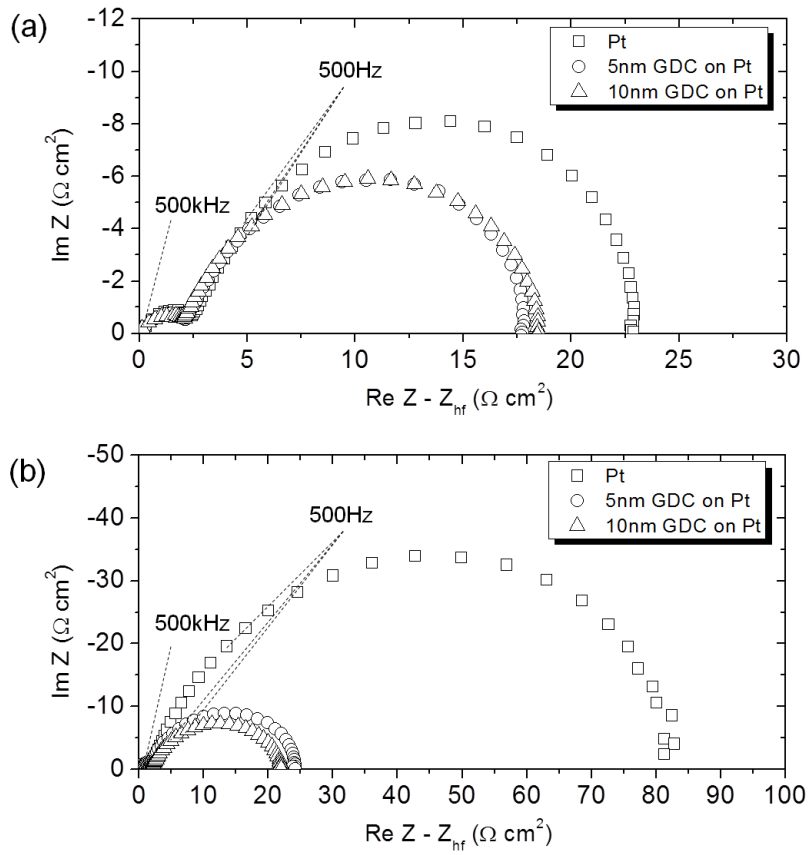


Fig. 2.6 (a) Initial and (b) 1 hour after EIS analysis of thermal barrier GDC coating on Pt electrodes at 500 °C.

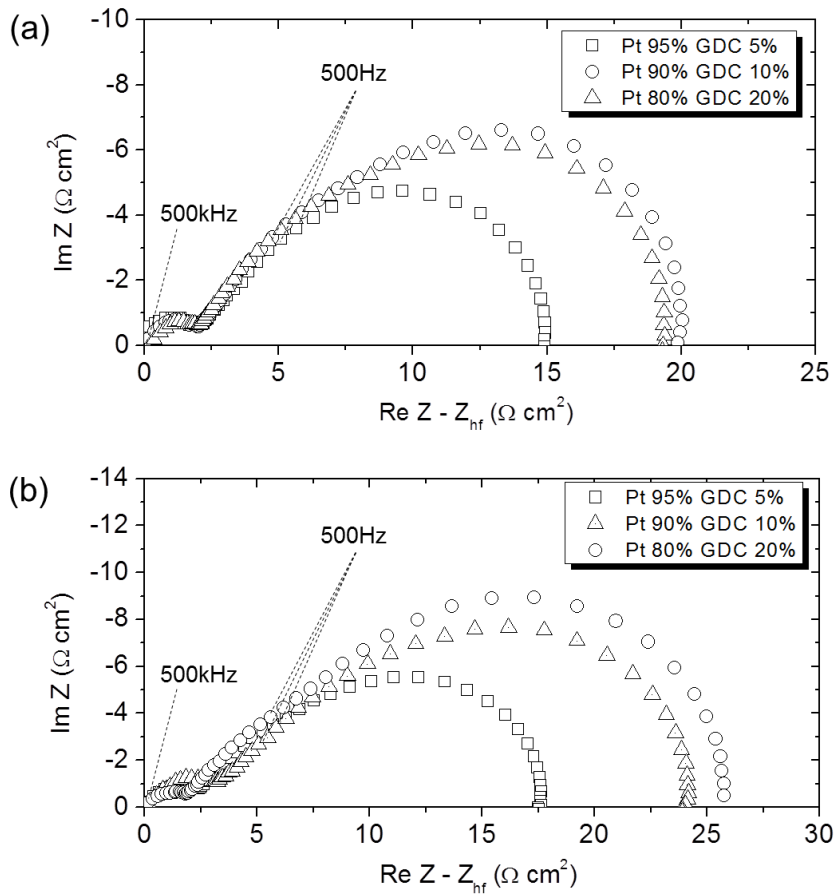


Fig. 2.7 (a) Initial and (b) 1 hour after EIS analysis of dispersion-hardened Pt / GDC co-sputtered electrodes at 500 °C.

Table 2.3 Initial performance, 1 hour after performance, and degradation percentages of cells using Pt / GDC composite electrodes.

	<b>Initial performance</b> (mW cm <sup>-2</sup> )	<b>1 hour after performance</b> (mW cm <sup>-2</sup> )	<b>Degradation</b> (%/h)
<b>Pure Pt</b>	6.63	3.77	43.1
<b>5 nm-GDC on Pt</b>	7.61	6.34	16.6
<b>10 nm-GDC on Pt</b>	7.42	6.60	11.0
<b>Pt 95% / GDC 5%</b>	7.91	7.30	7.7
<b>Pt 90% / GDC 10%</b>	6.94	6.13	11.6
<b>Pt 80% / GDC 20%</b>	6.72	6.20	7.7

Table 2.4 EIS measured initial and 1 hour after reaction resistances and resistance increments of the cells using Pt / GDC composite electrodes

	<b>Initial reaction resistance</b> (Ω cm <sup>2</sup> )	<b>1 hour after reaction resistance</b> (Ω cm <sup>2</sup> )	<b>Resistance Increment</b> (%)
<b>Pure Pt</b>	22.8	81.3	255.2
<b>5 nm-GDC on Pt</b>	17.7	24.2	36.7
<b>10 nm-GDC on Pt</b>	18.4	22.0	19.5
<b>Pt 95% / GDC 5%</b>	15.5	17.5	19.3
<b>Pt 90% / GDC 10%</b>	19.8	26.1	31.8
<b>Pt 80% / GDC 20%</b>	18.3	24.3	32.7

In the case of GDC coated Pt, the cathodic reaction resistance is caused mainly by the Pt/YSZ interface since GDC only exist at the surface of the Pt. Also, co-sputtered electrodes have the GDC/Pt interface as well as the Pt/YSZ interface; therefore, a diverse analysis of EIS data using morphology and reaction kinetics is required. As the surface morphologies of the 90% Pt / 10% GDC samples and 80% Pt / 20% GDC samples were nearly identical, the difference in performance is likely due to the different ratio of GDC. However, there is no particular performance difference between these samples. Moreover, the highest performance was obtained by the 95% Pt / 5% GDC electrode, which has a lower GDC ratio and a larger pore size. Although the amount of GDC ceramic to Pt increased, the peak power density of the fuel cell did not; rather, it showed saturation behavior. This demonstrates that the surface morphology is a dominant factor in using nanoporous metal electrodes for LT-SOFCs.

Last, we measured the current output of electrodes at 0.7 V to observe long term stability. First, the Pt electrode was selected as the reference. Then, the 10 nm-GDC coated Pt sample and the 95% Pt /5% GDC dispersion hardened sample were selected because they showed higher performance and stability among the homogenous deposition methods. According to Fig. 8, the pure Pt cathode showed constant degradation during measurement. Serious performance degradation of pure Pt sample was similarly observed in a research study by Y.B. Kim et al.[55], who used the same deposition method and temperature condition. The 10 nm-GDC coated Pt sample and 95% Pt / 5% GDC dispersion hardened sample exhibited superior thermal stability without significant performance degradation. Although a

slight degradation was observed in the first 3000 sec, a stable and constant current output was observed afterwards. Since the current output was stabilized within 1 hour, there was no particular difference between 1 hour and 3 hour degradation.

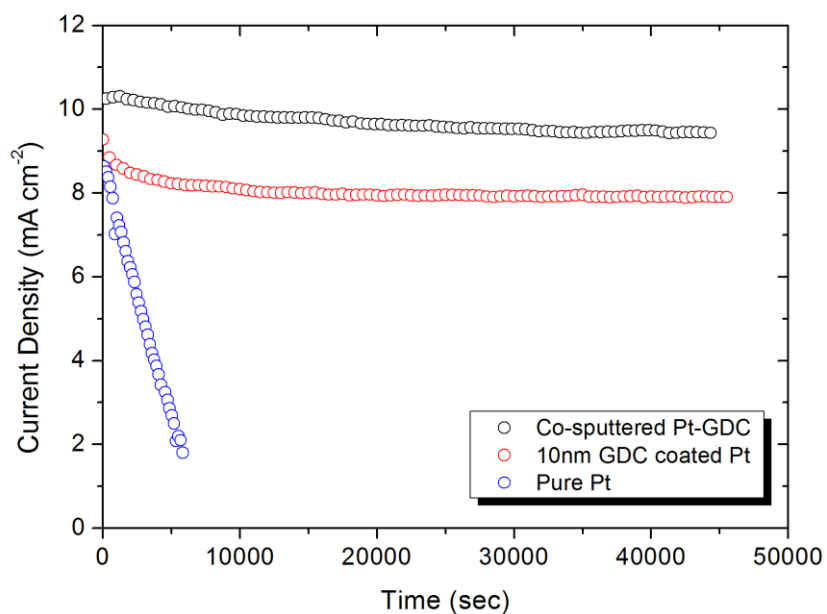


Fig. 2.8 12 hour potentiostatic data of pure Pt, 10nm-GDC coated Pt and co-sputtered 95% Pt / 5% GDC electrodes at 0.7V.

#### **2.1.4. Conclusion**

Thermal barrier coating and dispersion hardening methods were used to improve the thermal stability of nano-porous Pt electrodes. While the pure Pt electrode suffered serious performance degradation due to coarsening at an operating temperature of 500 °C, the thermal barrier coating and dispersion-hardened Pt/GDC electrodes showed superior thermal stability and significant performance enhancement. Different film morphology was observed using the various deposition techniques and GDC ratios, and electrochemical analysis was performed to further investigate the fuel cell performance.

## **2.2 Thin film application to solid oxide fuel cell electrolytes.**

In the past, a thin film YSZ was usually fabricated by sputtering of ceramic targets. Using ceramic as a sputtering target requires radio frequency power sources and copper plate bonding by indium to the targets. Applying high power could easily damage the ceramic target, so there is limitation of RF bias, which causes the low deposition rates.

The reactive sputtering is a technique using mixture of oxygen or nitrogen in the sputtering gas to fabricate an original target material in oxides or nitrides films. Metal targets are usually used for reactive sputtering which allows a high power to the target. The films with more various structures and composition can be fabricated by adjusting the sputtering conditions such as power, gas flow, chamber pressure, ratio of gas mixture and target to substrate distance.

For above reasons, we used metal Y/Zr alloy to fabricate YSZ film electrolyte by reactive sputtering, instead of using ceramic targets. Reactive sputtering of Y/Zr metal targets using Ar/O<sub>2</sub> mixture gas has advantages of allowing both DC and RF power sources, crack free targets, high deposition rates [20]. However, the morphology, crystallinity and elemental composition of films prepared by the reactive sputtering are much more sensitive compared to the conventional sputtering. Thus, morphology, composition and crystallinity have to be observed by devices such as FE-SEM, XPS and XRD.

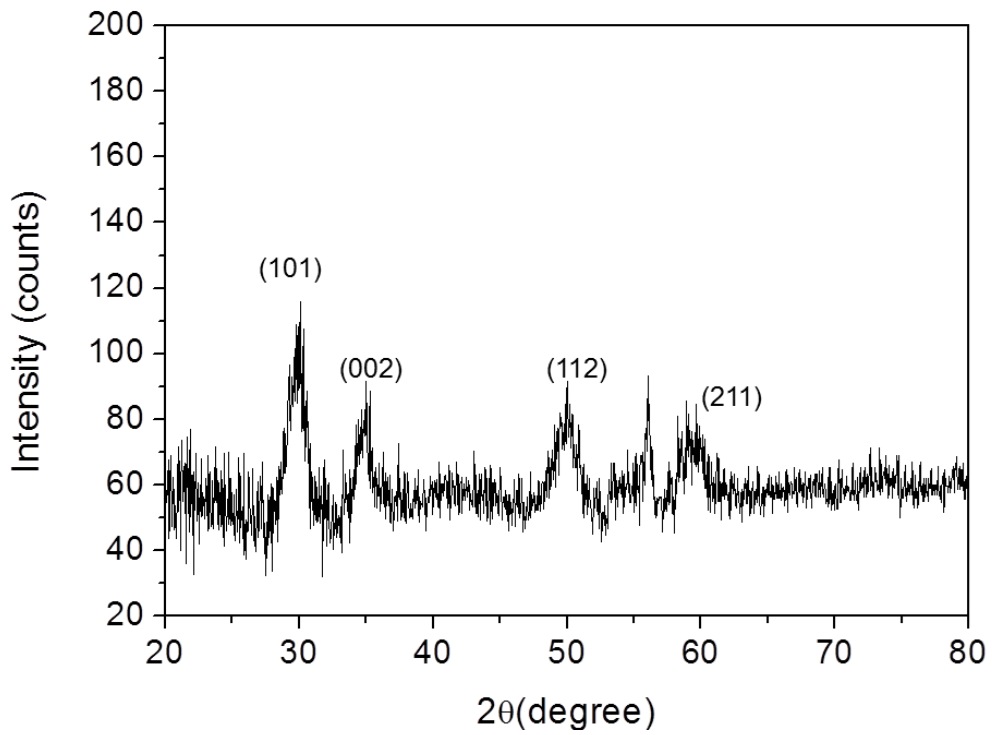


Fig.2.9 XRD patterns of thin film YSZ prepared by reactive sputtering of Y/Zr metal targets.

First, we fabricated 50nm of YSZ film to the Si-wafer for the precise measurements of the XPS and XRD. A Y/Zr metal alloy was used as a sputtering target and the pressure of sputter chamber was maintained 5mtorr with 80:20 ratio of Ar : O<sub>2</sub>. The XPS results (Table 2.5) shows that YSZ film electrolyte using Y/Zr metal alloy has ratio of approximately 11% of Y<sub>2</sub>O<sub>3</sub> and 89% of ZrO<sub>2</sub>.

Table 2.5 XPS data of YSZ film prepared by reactive sputtering of Y/Zr metal alloy

Name	Atomic%
O1s	63.29
Y3d	7.15
Zr3d	28.98
C1s	0.59

The ratio between metals and oxygen shows the film is fully oxidized without the phase of metals. YSZ electrolytes shows best ionic conductivity in range of 7~10% of Y<sub>2</sub>O<sub>3</sub>, and our fabrication nearly satisfy the requirements. According to the figure 2.9, XRD peaks shows (101), (002), (112) and (211) which indicating the polycrystalline structure of thin film YSZ. According to the analysis of the YSZ film on Si-wafer, composition and crystallinity seems suitable for using as an electrolyte.

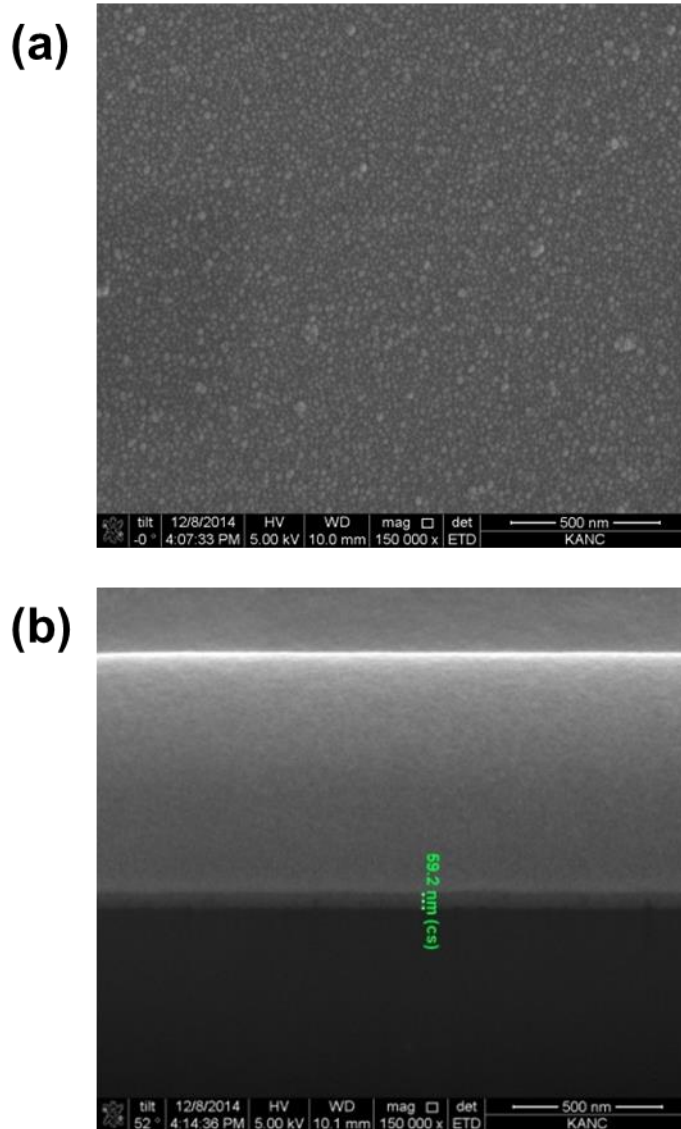


Figure 2.10 FE-SEM analysis of (a) surface, (b) cross-sectional images of YSZ film by reactive sputtering of Y/Zr metal alloy using Ar + O<sub>2</sub> mixture gas.

Figure 2.10 shows the FE-SEM analysis of 60nm YSZ film by reactive sputtering of Y/Zr metal alloy using Ar + O<sub>2</sub> mixture gas. Even though thickness of

the film is ultra-thin, surface morphology seems dense with nano grains. According to the Huang et al's research [56], nano grain of electrolyte improved performance of cell due to the enhanced oxygen reduction and exchange rate at the interface of electrolyte and cathode. Thus applying above thin film nano crystalline YSZ by reactive sputtering is expected to enhance the performance of thin film SOFCs.

## Chapter 3 Operation of thin film SOFCs using direct methane Fuels

### 3.1 Introduction

Although there are several fuel cell types by different electrolyte and operating temperature, they usually use hydrogen as a fuel. Over 95% of hydrogen is however achieved by reforming hydrocarbons and nearly 30% of the fuel is lost during the reforming procedure [65]. Furthermore hydrogen has serious problem of storage. A liquid form of hydrogen requires expensive devices such as cryogenic storage and large energy is needed to cool down hydrogen below  $-250^{\circ}\text{C}$ . A capability of metal hydrides is generally below 10 wt. %, so weight problem of hydrogen storage systems still remains. A hydrocarbons, on the other hand, has more than a 2–3 times bigger energy density and easy to storage in a liquid form.

In past, systems of hydrocarbon fuel – reformer – fuel cell stack are introduced to utilize hydrocarbon fuels [1]. About a decade, it has been found that the hydrocarbons can be directly used as a fuel without reforming [3]. The direct utilization of hydrocarbon requires high temperature (generally over  $500\text{-}600^{\circ}\text{C}$ ) thus the research of the direct hydrocarbon fuel cells generally use platform of the solid oxide fuel cell.

Solid oxide fuel cells, as known as SOFCs are high temperature ( $700^{\circ}\text{C} >$ ) operating fuel cell due to the ionic conductivity of the electrolyte. For the practical applications, it is required to lower the operating temperature of SOFC in the range of  $500\text{-}600^{\circ}\text{C}$  [[2]]. In this temperature range, we can maintain the advantages of

SOFC such as high efficiency, fuel flexibility and low cost materials while avoiding the disadvantages of sealing, thermal degradation and heat managements.

Applications of nano fabrication on the fuel cells significantly decreased thickness of the electrolytes and increased triple phase boundary through improved nanostructures of electrodes. Several studies have been demonstrated SOFC in the temperature range of 300-600°C using various fabrication method and structures[[8,13,21,46–48,52,64]]. In the past, Pt was popularly used as an electrode because fine and porous nanostructure is simply achieved by sputtering. Recently, Ni based anode and perovskite cathode such as LSCF, LSC has been introduced as a thin film SOFC's electrodes. Since there are a few researches about direct hydrocarbon thin film SOFC, it is required to fabricate a thin film SOFC which can be operated with direct hydrocarbons.

In case of using conventional NiO-YSZ for the anode, long time operating with hydrocarbon can cause serious performance degradation due to carbon deposition on the anode. Using ceramic based anodes such as CeO<sub>2</sub> or including catalyst such as copper or palladium were introduced to solve carbon deposition and performance enhancement[66]. Recently, including ruthenium on the anode showed full oxidation of hydrocarbon fuels and improved performance. T. hibino et al.'s research showed similar performance to the hydrogen using NiO-GDC-Ru anode with hydrocarbon fuels (methane, ethane, propane) and furthermore, no significant performance degradation was observed during the operation [45].

Our research goal is to combine advantages of nano fabricated SOFC and direct utilization of hydrocarbons. For direct utilization of hydrocarbon without

reforming, the cell was operated at 500°C with NiO-GDC-Ru anode. We also tried to improve the nano structures of anode by sputtering method to secure maximum triple phase boundary.

### 3.2 Experimental

Anodized aluminum oxide (AAO) was used for a nano porous substrate and it has 100µm of thickness, 80nm of pore size and 10% of porosity. On the account of a regular pore distribution and low tortuosity, AAO is recently become a widespread substrate for thin film SOFC. Anode, electrolyte and cathode were deposited by using sputtering system.

The optimal anode structure we expected was uniform mixture of Ru / Ni / GDC and it require co-sputtering of three targets with three power sources. However, our system has only 2 power sources, thus we used structure of AAO / Ru / Ni – GDC (Fig. 3.1). Ru / Ni – GDC structure was introduced by Z. Shao et al's work[67] and showed proper performance using hydrocarbon fuels. The ruthenium was deposited on the AAO substrate with the thickness of 30nm. On the surface of Ru on AAO, 400nm thick Ni and GDC composite was co deposited by co-sputtering method.

The 1µm thick yttria stabilized zirconia (YSZ) electrolyte was deposited on the anode by sputter. We used Y/Zr metal alloy and the pressure of sputter chamber was maintained 5mtorr with 80:20 ratio of Ar : O<sub>2</sub> for the reactive sputtering. 200nm thick nano-porous Pt was used as a cathode.

Electrochemical measurements of the cell were conducted at 500 °C by a custom-made test station. The anode was supplied with hydrogen and methane, which was saturated with H<sub>2</sub>O at room temperature and the cathode side was exposed to air for natural oxygen supply. The flow rate of the fuel at the anode was

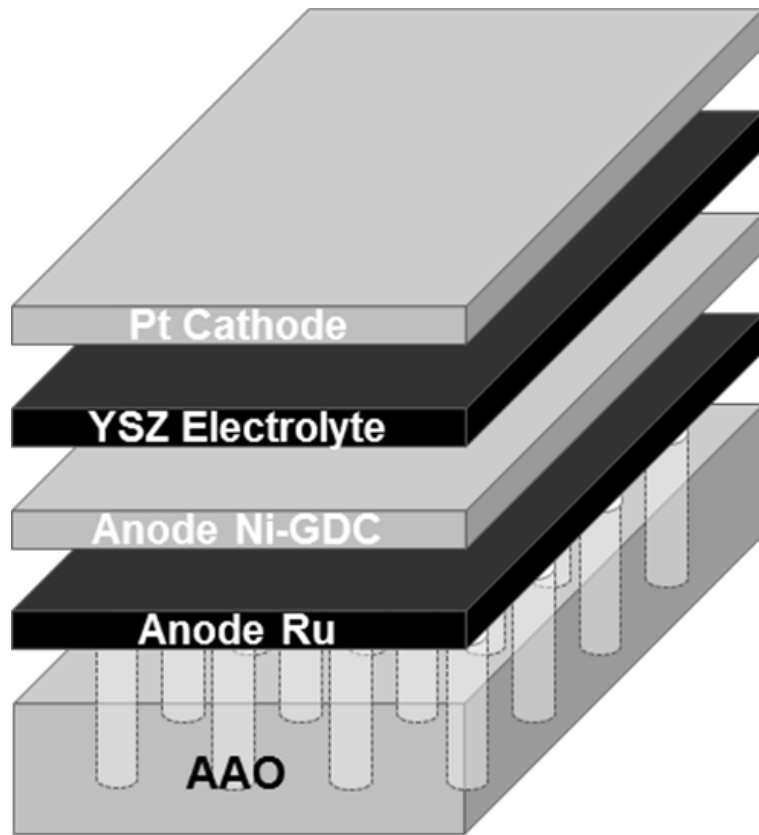


Figure 3.1 Cell image of thin film SOFC using direct hydrocarbon as a fuel.

100sccm for the both hydrogen and methane. Solartron 1287 electrochemical interface and a 1260 impedance analyzer were used for electrochemical characterization.

### 3. Result and Discussion

The most important thing in the operation of SOFC using hydrocarbon is anode material and structure. When using hydrogen as a fuel, porous platinum perform as an anode sufficiently, even though the thickness is less than 100nm [13]. When using hydrocarbons however, structure and material need to be chosen carefully because of hydrocarbons complex reforming procedure. The initial temperature of reforming is known to be over 500°C~600°C, it is also required to fabricate the thermally stable anode in this temperature region. Nano fabricated electrodes have increased surface area due to smaller grains and pores compared to the conventional electrodes. Although increased surface area of electrodes has advantages of high catalytic activity and improved TPB area, it is also favorable condition for thermal deterioration. In particular, this problem was usually found in the metal electrodes and several studies have been proposed the solutions [55,68]. As shown in the figure 3.2 (a),(b), pure Ni electrode shows thermal deterioration with aggregated grains and pores. This structure has a low catalytic activity due to the low surface area, and fuel supply is also unavailable. Although there was morphological change of Ni-GDC co-sputtered electrodes, nano grains and pores were maintained even after the annealing temperature of 600°C.

Method of increasing the thermal durability of metals by mixing ceramic is known as dispersion hardening, and it was usually applied for the bulk status materials. By uniformly mixing a small amount of the stable ceramic powder to the metals, matrices of ceramics limit the movement of the metals and prevent the microstructural deterioration[57,58]. In our case (figure 3.2 (c), (d)) GDC perform

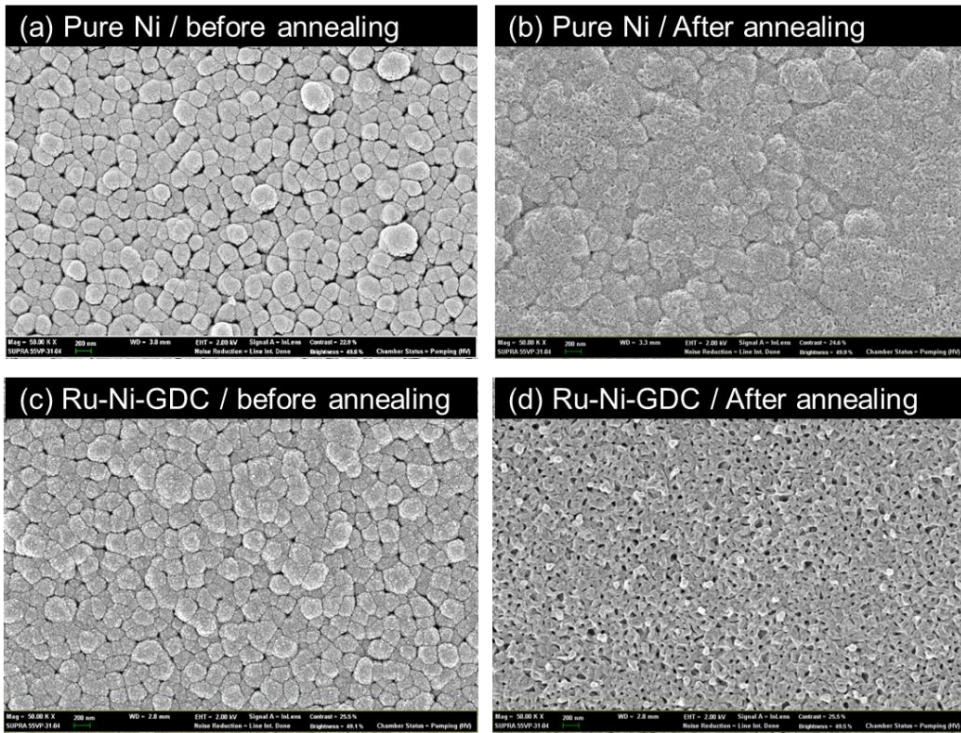


Figure 3.2 FE-SEM analysis of Ni based anodes. As deposited samples of (a) Ni and (b) Ru/Ni-GDC. Samples after Sintering at 600oC. (a) Ni and (b) Ru/Ni-GDC.

as a ceramic material which prevents the aggregation of nano structured Ni. It is difficult to fabricate thin, dense and pinhole free electrolyte on the porous substrate using physical vapor deposition techniques. In the case of using physical vapor deposition as an electrolyte deposition, the morphology of the film is similar to the morphology of the porous substrate. For this reason previous researches used functional layer by chemical vapor deposition method[41] or avoided using porous substrate[13,46,47].

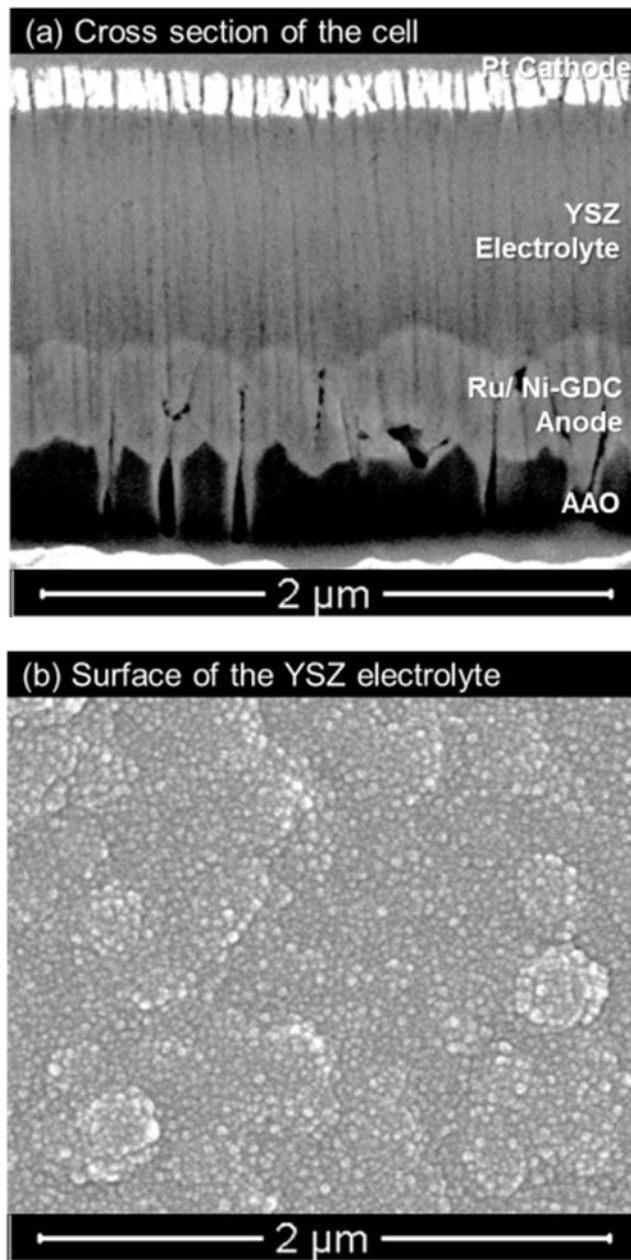


Figure 3.3 FE-SEM analysis of (a) cross section of the cell and (b) surface of the YSZ electrolyte.

According to figure 3.3, surface and cross sectional image of the YSZ film on the AAO substrate seems fully dense and pinhole free. Applying the methods described above, cell was fabricated with the structure of AAO/Ru/NiO-GDC/YSZ/Pt and measured at 500°C. The cell measuring temperature was chosen to prevent carbon deposition at the anode and deterioration of the cell. If the operating temperature is below 500°C, it has high possibility of carbon deposition due to Boudouard reaction ( $2\text{CO} = \text{C} + \text{CO}_2$ ). Temperature over 700°C has also high possibility of carbon deposition due to the pyrolysis of methane ( $\text{CH}_4 = \text{C} + 2\text{H}_2$ ). Thus operating temperature of SOFCs using direct hydrocarbon are usually between 500°C-700°C.

Figure 3.4 shows the performance of the cell using hydrogen and methane evaluated at 500°C. The peak power density of the cell using hydrogen and methane was  $87\text{mW cm}^{-2}$  and  $76\text{mW cm}^{-2}$  respectively. Theoretically, the performance of SOFC using hydrocarbon is higher than using hydrogen. However, the actual performance is usually higher using hydrogen. According to park et al.'s work, peak power density was more than twice bigger using hydrogen compared to the hydrocarbon fuels[69]. Steam-methane reforming process has high efficiency (>90%) over 800°C - 900°C[65], thus operating at temperature between 500-700°C has high possibility of decreased performance. Copper, palladium, ruthenium and ceria based material was applied to the anode to overcome the low efficiency of anode reaction. Recently, mixture of nickel, ruthenium and doped ceria is known as the best anode material for using direct hydrocarbons. According to the T.Hibino et al.'s work[45], the performance of the cell using Ni-Ru-GDC anode was similar

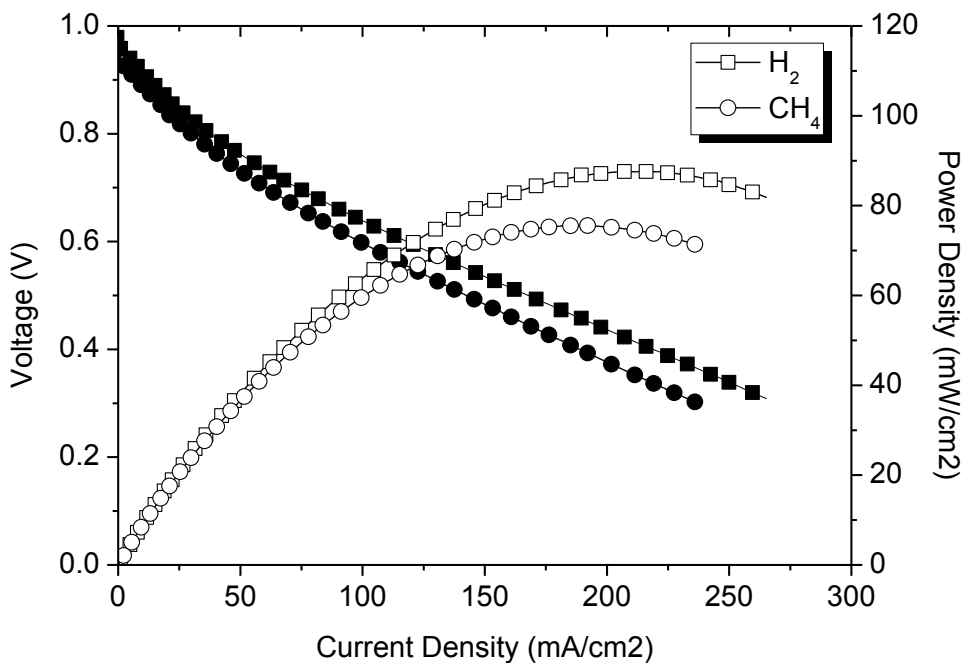
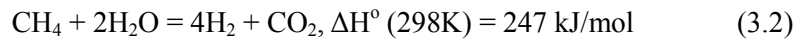


Figure 3.4 Performance of thin film SOFC using different fuels at 500°C. The fuels were supplied with fully humidified hydrogen and methane at room temperature. The flow rates of fuels were 100sccm.

regardless of the fuel (hydrogen, methane, ethane, propane) at 600oC. Our cell used same material and shows only ~10% of performance difference between hydrogen and hydrocarbons. We expect the gap between the performances will decrease if we make the anode with full mixture of Ni-Ru-GDC instead of using separate layer of Ru / Ni-GDC.

To further verify the precise reason of the performance difference between

hydrogen and methane, electrochemical impedance spectroscopy (EIS) data was obtained. According to the impedance spectra shown in figure 3.5, we can clearly observe the difference of the electrode resistance. The reforming reaction of the methane is highly endothermic (equation (3.1), (3.2)), thus it can cause a temperature drop to the cell.



Since there was no difference in ohmic loss, we can conclude that the endothermic reaction of methane reforming does not effect to the cell performance. However, electrode resistance was  $4.5\text{ohm cm}^2$  using hydrogen and  $7\text{ohm cm}^2$  using methane indicating that the performance difference is generated by the difference of the electrode resistance.

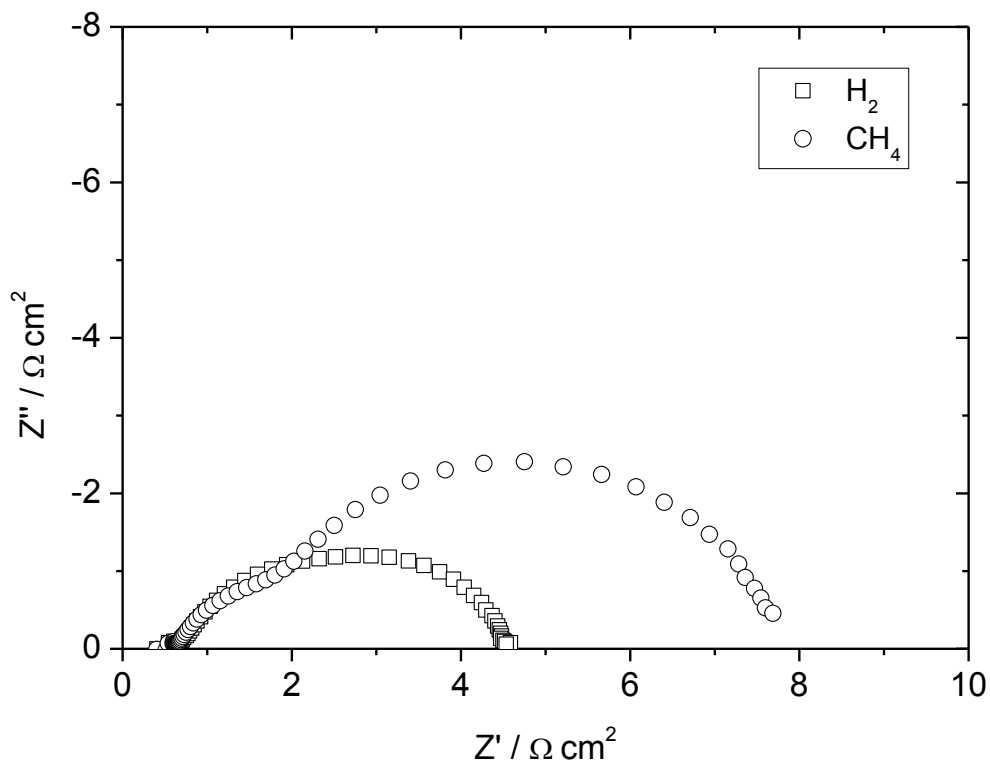


Figure 3.5 Impedance spectra of SOFC using different fuels at 500oC. The measurement was taken at OCV.

### **3.4 Conclusion**

Thin film SOFC based on nano porous AAO has been fabricated using Ru/NiO-GDC anode. The fabricated anode has fine nano structure and thermal durability is superior compared to the conventional Ni anode. Two different fuels (hydrogen, methane) were used to verify the feasibility of direct methane operation and it showed only 10% of performance difference. We used ruthenium and Ni-GDC layer separately due to the technical problems, however we expect the performance difference could be decreased by mixing ruthenium to the entire anode structure.

## Chapter 4 Single Chamber Operation of Thin Film SOFCs

### 4.1 Introduction

As mentioned in chapter 1, single chamber operation of SOFCs has advantages of less restrained designs and high performances. It can easily avoid the pinhole and density issues of thin film electrolyte, since single chamber operation doesn't require dense and gas-tight electrolyte [44]. The conventional ceramic processes have difficulties in the fabrication of controlling porosity and particle size of electrodes, however, it can be easily controlled through thin film fabrications. It is important in single chamber SOFCs to manage the porosity and particle size to control the selective catalytic activity. Application of thin film electrolyte is a huge advantage in single chamber operation because the effect of performance improvement by thinner electrolyte is bigger than that of dual chamber operation [43].

In this chapter single chamber SOFC was fabricated on the AAO substrate using Ni-based and Ru-based anodes, YSZ electrolyte and perovskite cathodes. Sputtering and pulsed laser deposition was used to develop cells with high stability and performance. Thus, the basic skill from chapter 2 and 3 was again applied to the fabrication. The dispersion hardening skill was used to fabricate porous and stable nano-structured electrodes and cubic, polycrystalline YSZ thin film by reactive sputtering of Y/Zr metal alloy was applied for electrolyte fabrication. The Au was applied to the cathode to improve electric conductivity, since Au is a highly electric conductive and catalytically inert to the parasitic reactions.

## 4.2 Experimental

The thin film single chamber SOFC was fabricated on the porous AAO substrates with 80nm of pore size and 100um of thickness. For anode deposition, we used nickel based anodes and ruthenium based anodes with sputtering. To enhance thermomechanical stability, GDC was mixed by co-sputtering method. The sputtering chamber was maintained 30mtorr with Ar gas and 200W of DC power was applied to the nickel and ruthenium target. We applied 50W of RF power to the GDC target for co-sputtering. The thin film YSZ electrolyte was fabricated by sputter, using Y/Zr metal alloy with reactive sputtering. The base pressure of sputtering chamber was maintained 5mtorr during sputtering. A 200W of RF power was applied to the Y/Zr metal alloy target and substrate was rotated for uniform deposition. For the cathode, we used both sputtering and PLD for perovskite (SSC, LSCF) deposition. To improve porosity of perovskite cathode film by sputtering, we mixed Au by co-sputtering to increase porosity. Au film by sputtering was also used as a current collecting layer of PLD deposited cathode films.

Electrochemical measurements of the cell were conducted between 500 °C – 600°C by a custom-made test station. The cell was supplied with mixture of methane and air. The fuel and air mixture was maintained in the value of  $R_{\text{mix}}=2$ . Solartron 1287 electrochemical interface and a 1260 impedance analyzer were used for electrochemical measurement.

## 4.3 Results and discussion

### 4.3.1 Characterization of anode materials and structure

The nickel based electrodes are most widely used anodes in area of conventional single chamber SOFCs, therefore, Ni-GDC anodes were fabricated on the AAO substrate. The figure 4.1 shows the surface and the cross-sectional image of the Ni-GDC electrodes by FE-SEM. Figure 4.1 (a) shows the surface of as-deposited Ni-GDC electrodes and Figure 4.1 (b) shows the surface of Ni-GDC electrodes after annealing at 650°C. Although we mixed GDC ceramic in the Ni electrodes to prevent aggregation, there were significant morphological differences between as-deposited and heat-treated sample. In case of the Pt-GDC sample in chapter 1, the operating temperature was 500°C, thus less heat energy was delivered to the electrodes. However, single chamber operation of SOFCs using methane as a fuel requires more than 650°C, so the electrodes were heat treated at 650°C. Although the surface morphology of the heat treated Ni-GDC samples look porous, we cannot guarantee the pores are fully open through the AAO substrate. Thus, we measured cross-sectional FE-SEM images of as-deposited and heat treated Ni-GDC sample (Figure 4.1(c), (d)). According to the cross-sectional image of as-deposited Ni-GDC (Figure 4.1(c)), pores are fully connected to the AAO substrate. In case of the cross sectional images of heat treated Ni-GDC (Figure 4.1(d)), however, pores are closed which will block the flow of fuels. A partial oxidation reaction in anodes requires high catalytic activity [43], thus improvement of Ni-GDC structure by co-sputtering is required. We tried to fabricate durable and porous electrodes of Ni-GDC by controlling co-sputtering conditions, however, it

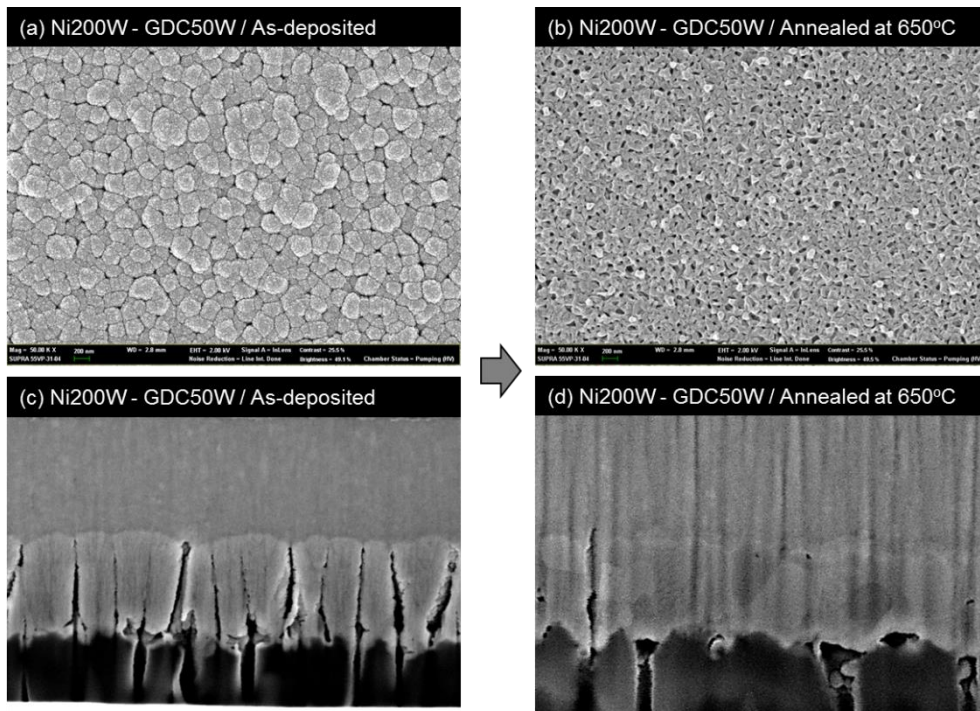


Figure 4.1 The surface and the cross-sectional image of the Ni-GDC electrodes by FE-SEM. (a) Surface image of as-deposited Ni-GDC, (b) surface image of heat-treated Ni-GDC at 650°C, (c) cross-sectional image of as-deposited Ni-GDC, (d) cross-sectional image of as-deposited Ni-GDC

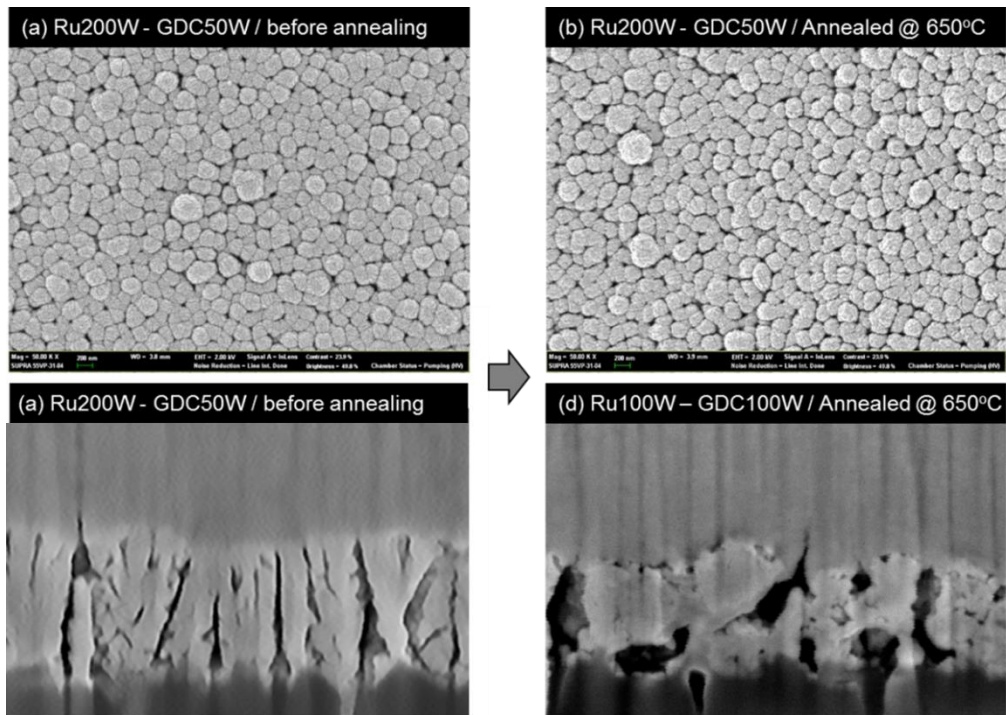


Figure 4.2 The surface and the cross-sectional image of the Ru-GDC electrodes by FE-SEM. (a) Surface image of as-deposited Ru-GDC, (b) surface image of heat-treated Ru-GDC at 650°C, (c) cross-sectional image of as-deposited Ru-GDC, (d) cross-sectional image of as-deposited Ru-GDC

was unable to avoid aggregation of electrodes after heat treating. Thus we changed the base material of anodes from Ni to Ru.

The figure 4.2 shows the surface and the cross-sectional image of the Ru-GDC electrodes by FE-SEM. Although as-deposited surface images of the Ru-GDC (Figure 4.2 (a)) electrode seems similar to the case of Ni-GDC electrode (Figure 4.1 (a)), the thermomechanical stability was further improved (Figure 4.2 (b)). Furthermore, cross sectional image of the Ru-GDC by FE-SEM shows nano-dendritic structure. A dendrite is a characteristic tree-like structure which has numerous nano-spikes, and it usually grow by undercooling of metals after melting. Thus, Ru-GDC anodes have superior catalytic activity due to the increased active area compared to the Ni-GDC electrodes.

To evaluate the performance of Ni-GDC and Ru-GDC electrodes, thin film fuel cells with 600nm YSZ electrolyte and 200nm Pt cathode were fabricated. To clearly observe the performance of anodes, cell was operated under dual chamber condition using methane and air of  $R_{\text{mix}}=2$  to the anodes. The cathode side was exposed to air for natural oxygen supply. In this configuration, reactions of anode side are same to single chamber condition and we can minimize the variables of cathodes reactions influencing the cell performance.

Figure 4.3 shows the cross sectional images of thin film SOFCs using Ni-GDC and Ru-GDC as an anode material. The image was taken after operation to observe the thermomechanical stability of anodes and evidence of carbon deposition. The thickness of anode, electrolyte and cathode were 400nm, 600nm and 200nm respectively.

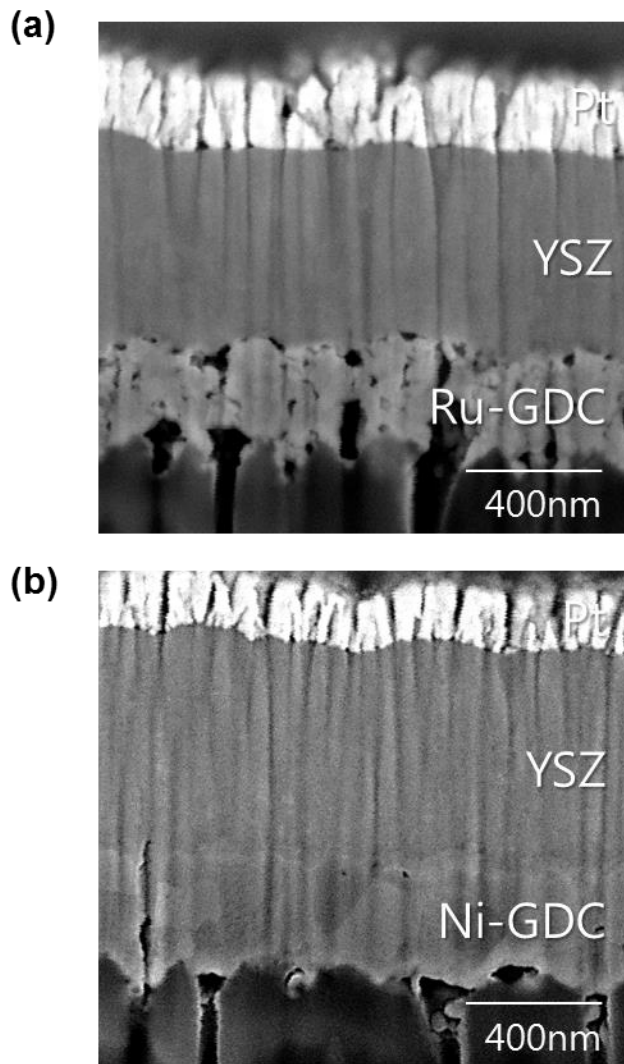


Figure 4.3 Cross sectional images of thin film SOFCs using (a) Ni-GDC and (b) Ru-GDC as an anode material.

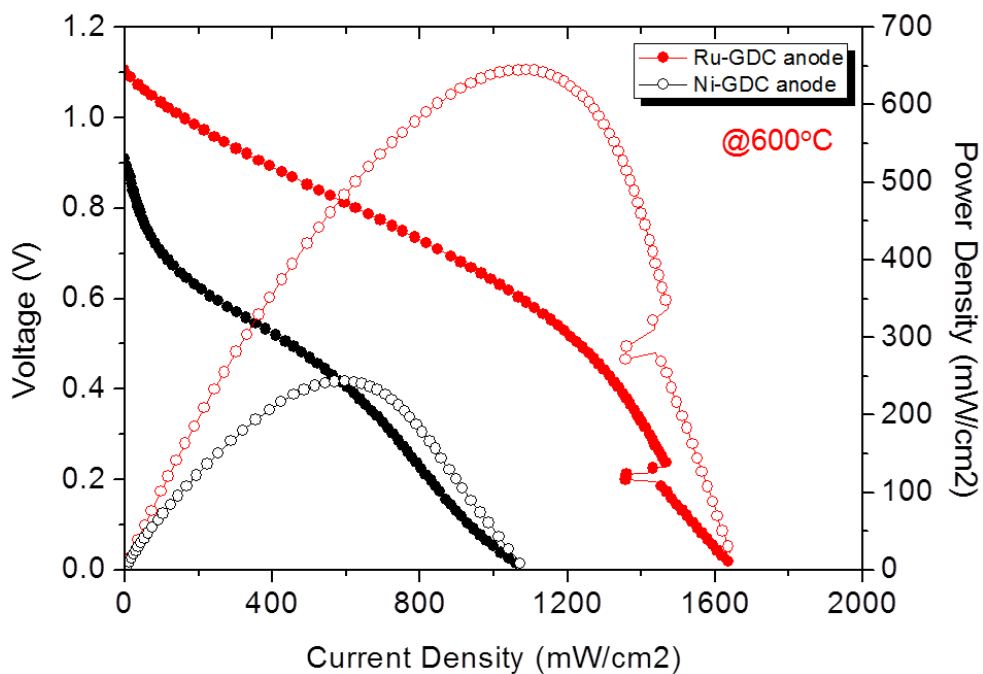


Figure 4.4 I-V curves of thin film SOFCs using (a) Ni-GDC and (b) Ru-GDC as an anode material. The cell was operated under dual chamber configuration of 600°C, and mixture of methane and air of  $R_{mix}=2$  was supplied to the anode side. The cathode was exposed for natural air supply.

The i-V and power density curves of the thin film fuel cells using Ni-GDC and Ru-GDC as anodes are shown in figure 4.4. Open circuit voltages of the thin film SOFC using Ni-GDC cell showed 0.92V while the thin film SOFC using Ru-GDC cell showed 1.1V. It reveals that the Ru-GDC anodes have more selective catalytic reaction toward anode reaction[44]. Furthermore, there were significant difference of peak power density of the thin film SOFC using Ni-GDC

(250mW/cm<sup>2</sup>) and Ru-GDC (650mW/cm<sup>2</sup>). According to the figure 4.3 Ni-GDC at the operating temperature seems dense which led to a block of the gas flow. The mass transport losses of Ni-GDC cell were observed after 500mA/cm<sup>2</sup> of current density. In case of Ru-GDC cell, the mass transport losses are observed after 1000mA/cm<sup>2</sup> so it is clear that the difference of catalytic selectiveness and nano-structure are main reasons of performance difference.

#### **4.3.1 Characterization of thin film perovskite electrodes for cathode.**

In previous section, we successfully developed Ru-GDC electrodes for anodes. For single chamber operation, we have to change the Pt cathode into electrodes which have selective catalytic cathode reaction. As mentioned before, perovskite materials are known as selective cathode catalyst for single chamber SOFCs, so in this section perovskite materials were developed by thin film fabrication technic. First we used sputter for fabrication of thin film SSC. The sputtering chamber was maintained 50mtorr with Ar gas and 100W of RF power was applied to the ceramic SSC target. The measured deposition rate of the SSC was 100nm/hour. According to the figure 4.5 the film was too dense for using as a cathode. Usually, film deposited by metal target at 50mtorr of chamber pressure shows porous structures [70], however, using ceramic target showed dense film regardless of chamber pressure.

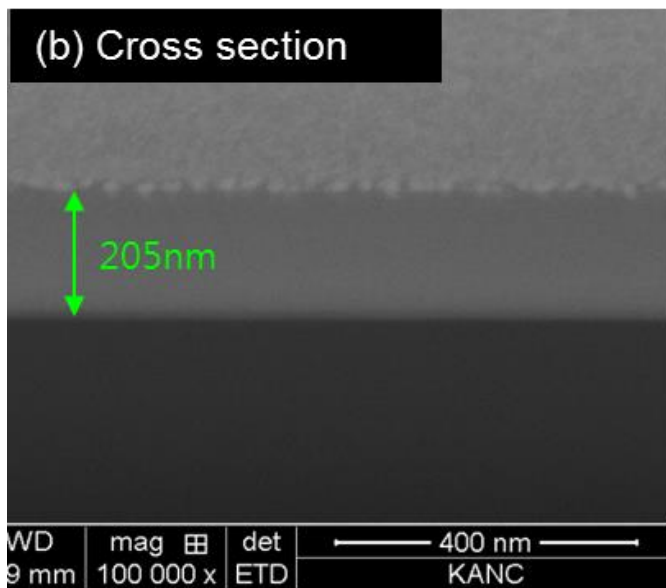
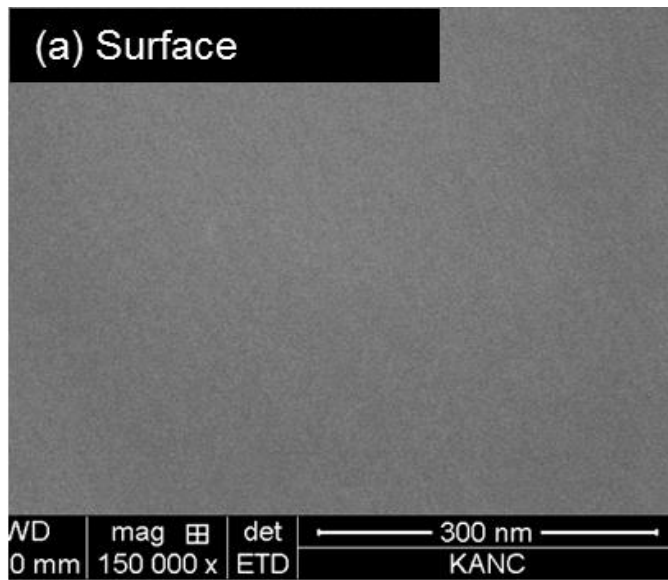


Figure 4.5 Surface and cross sectional FE-SEM image of thin film SSC electrode by sputtering. The sputtering condition was 50mtorr of Ar chamber pressure and 100W of RF power to ceramic SSC target.

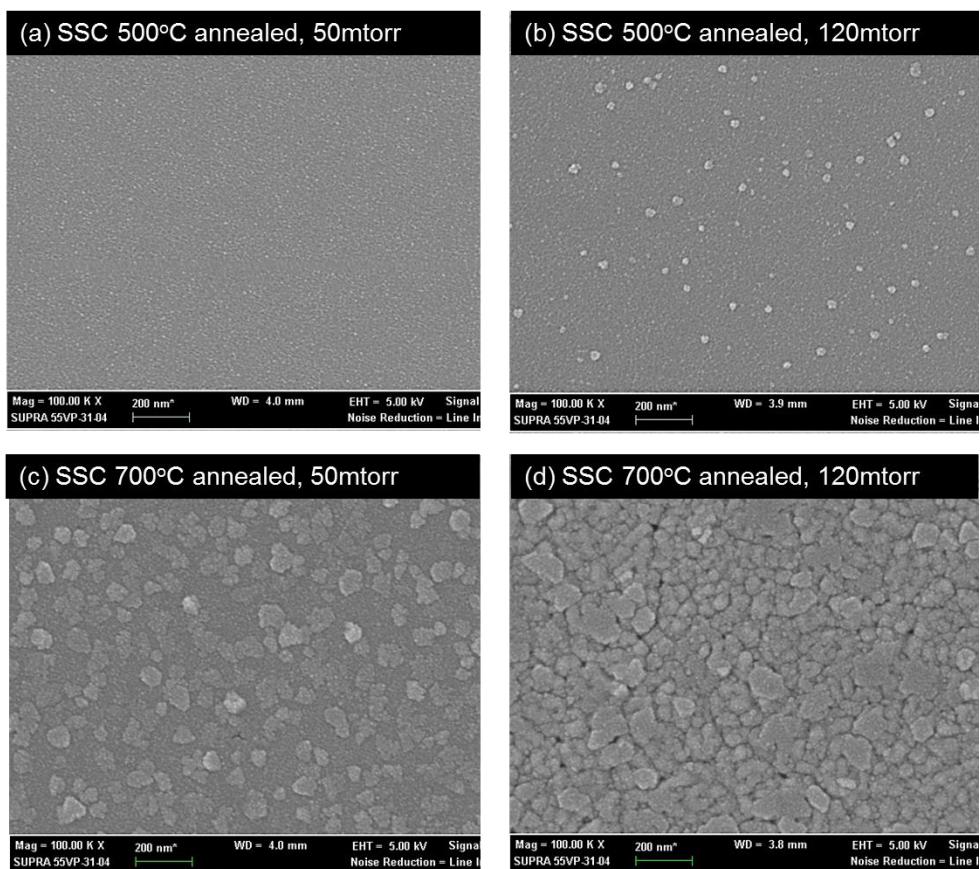


Figure 4.6 Surface and FE-SEM image of thin film SSC electrode after heat treatment by sputtering. (a) 500°C heat treated with 50mtorr of Ar chamber pressure, (b) 700°C heat treated with 50mtorr of Ar chamber pressure, (c) 500°C heat treated with 120mtorr of Ar chamber pressure, (a) 700°C heat treated with 120mtorr of Ar chamber pressure, .

To improve the porosity of the sputtered SSC cathode, we increased the pressure of sputter chamber and annealed the sample in range of 500°C to 700°C

(figure 4.6). The surface porosity of sputtered SSC film was improved as the annealing temperature and chamber pressure increased. Additionally, the grains of the film were also increased as the annealing temperature and chamber pressure increased. During the annealing process, SSC nano-grains tend to grow into bigger to minimize the surface energy. In case of increasing pressure of sputter chamber, sputtered particles are relatively more scattered by increased concentration of Ar in the chamber. Thus, relatively bigger SSC particles are generated during sputter.

The both 50mtorr and 120mtorr deposited and 700°C heat-treated SSC cathodes were applied to the cell for performance evaluation. In this case, we used 500um YSZ pellet as an electrolyte, because thin film SOFCs on AAO cannot secure thermomechanical stability under 700°C of heat treatment. Thus, SSC was deposited on a 500um YSZ pellet and then, it was heat treated at 700°C. After heat treatment, Pt anode was deposited on the other side of the YSZ pellet and tested under dual chamber condition using hydrogen. In this configuration, we can clearly evaluate the performance of SSC film.

Figure 4.7 shows the open circuit voltage of the fuel cell with SSC film on the cathode. In case of the cell using 50mtorr deposited SSC as a cathode, there was serious fluctuation of voltage before the cell reached 600°C. According to the above FE-SEM analysis of 50mtorr deposited SSC film, we suspect that the film was too dense to create a fuel cell reaction below 600°C. Even though the catalytic activity was improved due to the increased roughness of the surface, it cannot

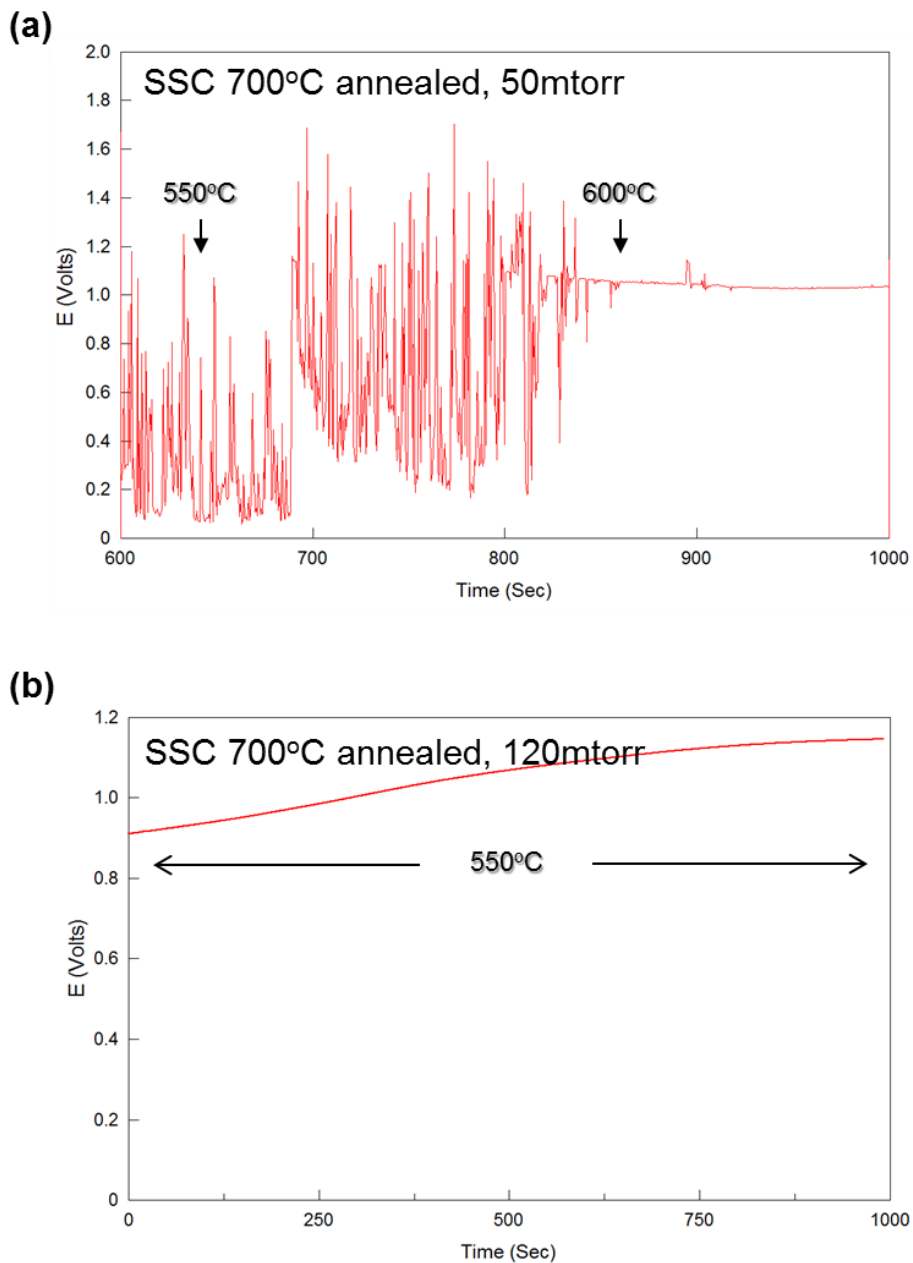


Figure 4.7 Open circuit voltage measurements of cell using (a) 700°C heat-treated SSC fabricated under 50mtorr of sputtering chamber, (b) 700°C heat-treated SSC fabricated under 120mtorr of sputtering chamber.

create TPB area without any pores, so the cell using 50mtorr of deposition condition required over 600°C of heat energy to create the proper open circuit voltage. In case of 120mtorr deposited SSC film, it showed 1.1V of open circuit voltage at 550°C. The voltage seems stable than that of 50mtorr deposited SSC and showed saturation behavior after 10minutes. According to the figure 4.5(d), several pores are created around the grains. Since material and average grain size of 50mtorr and 120mtorr deposited SSC films are similar, it is clear that porosity of the films was the main reason of different open circuit voltage tendency. However, once again, it was unable to measure i-V and EIS of 120mtorr cell due to the low current of the cell.

To improve the porosity issues of sputtered SSC film, we used co-sputtering method. In chapter 2, we observed that when the ratio of metal increased in the composite of metal and ceramic, porosity was increased. Gold was used as a co-sputtering material with SSC because it has high conductivity and inert to the anode reaction. To fabricate Au-SSC with a ratio of 30:72 (in vol%), 200W of RF power to the SSC ceramic target and 50W of DC power to the Au target were applied. The Au-SSC with a ratio of 60:40 (in vol%) was fabricated under sputtering condition of 200W of Rf power to the SSC target and 100W of DC power to the Au target. Figure 4.8 shows the surface analysis of Au-SSC film with different ratio. The grain size and porosity was increased as the ratio of Au increased. It showed similar tendency of Pt-GDC nano-composite electrode in chapter 2. To evaluate electrochemical performance of Au-SSC cathode, fuel cell was fabricated using 500um YSZ pellet.

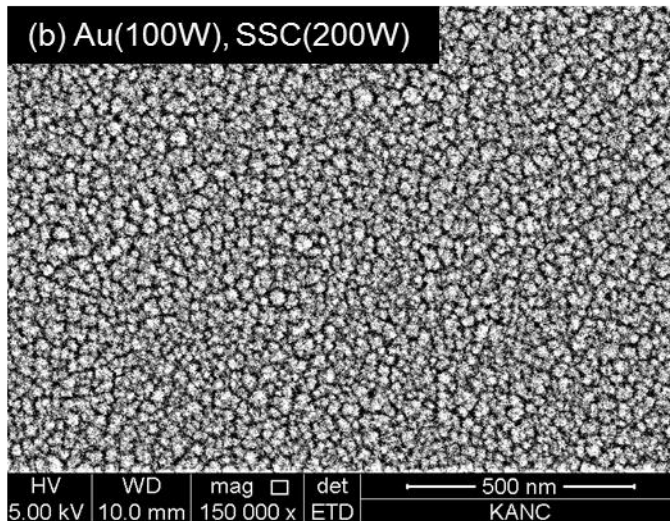
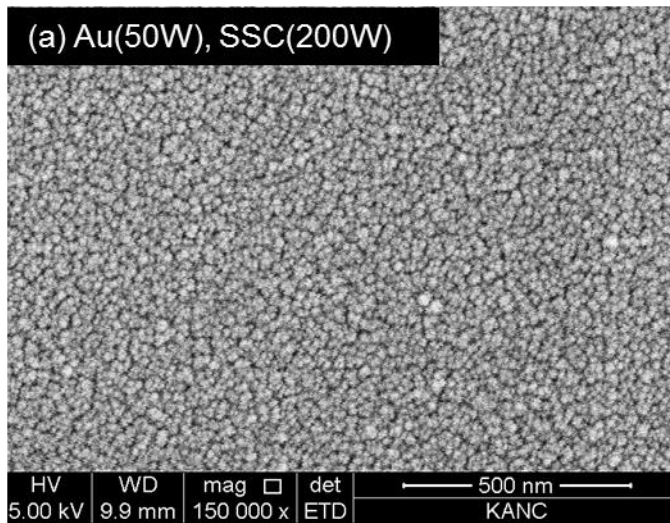


Figure 4.8 Surface FE-SEM analysis of Au-SSC with a co-sputtering condition of (a) 50W of DC power to the Au target and 200W of RF power to the SSC target, (b) 100W of DC power to the Au target and 200W of RF power to the SSC target.

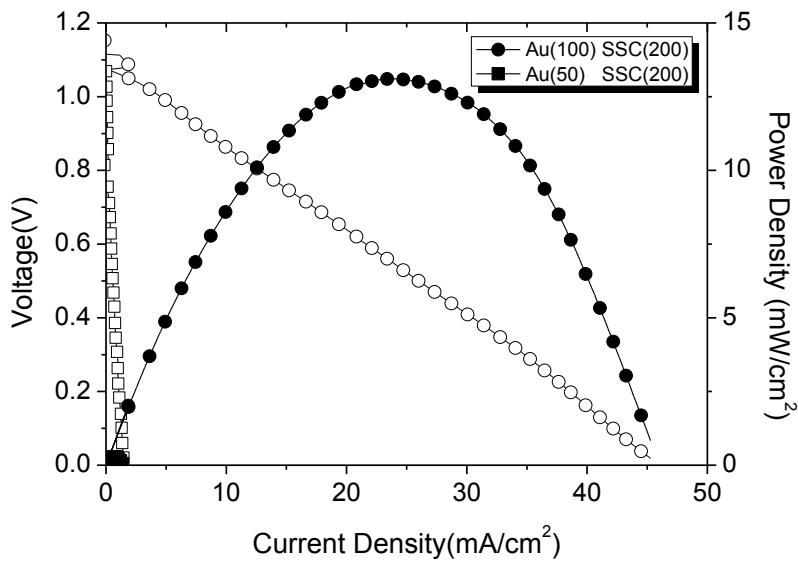


Figure 4.9 I-V and power density curves of fuel cell with Au-SSC cathodes on 500um YSZ pellet.

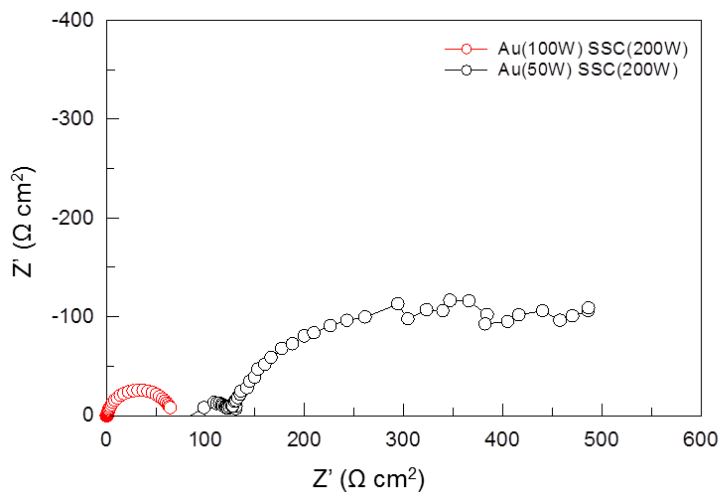


Figure 4.10 Impedance Spectra of fuel cell with Au-SSC cathodes on 500um YSZ pellet.

The Pt anode was used as an anode and the cell was tested under dual chamber condition at the temperature condition of 550°C.

As shown in figure 4.9 and 4.10, it was able to measure i-V and EIS characteristics, since the Au-SSC thin film cathode has enough TPB to create electricity. In case of Au(50W) SSC(200W) deposited cell, the peak power density was 1mW/cm<sup>2</sup> while Au(100W) SSC(200W) deposited cell was 13mW/cm<sup>2</sup>. The ohmic losses of the cells are far different even though we used same electrolyte and anode, therefore the main reason of the performance differences are generated at the cathode. To clearly observe the factors influencing the performance difference, EIS was measured. According to figure 4.10, ohmic loss of Au(100W) SSC(200W) cell was nearly 75Ωcm<sup>2</sup> smaller than that of Au(50W) SSC(200W). Since the Au (100W) SSC(200W) cathode has more Au ratio in the cell, we conclude that the improved current collection and electrode conductivity enhanced the cell performance

Furthermore, cathodic reaction resistance of Au(100W) SSC(200W) cell was nearly 10time smaller than that of Au(50W) SSC(200W) which led to a superior catalytic activity. Since the grain size of Au(50W) SSC(200W) cathode is smaller than that of Au(100W) SSC(200W) cathode, it is obvious that smaller catalyst have higher catalytic activity toward the reaction due to an increased surface area. However, the performance of Au(100W) SSC(200W) cathode, which has bigger size of catalyst showed higher catalytic activity. If the overall cathode kinetics happen on the surface of catalyst regardless to the porosity, the reaction resistance

of Au(50W) SSC(200W) cathode will be smaller than that of Au(100W) SSC(200W). However, oxygen reduction reactions are concentrated at the interface of electrolyte and electrode. Thus, porosity is also important factor of fuel cell operation, and the difference of porosity between Au(50W) SSC(200W) cathode and Au(100W) SSC(200W) cathode generated the difference of reaction resistance.

According to the experimental results of SSC cathode film by sputtering, it is required to fabricate porous and conductive film. We used pulsed laser deposition to overcome the restrain of sputtering method. The deposition unit of pulsed laser deposition is bigger than that of sputtering [71], so it is convenient to make porous ceramic films. The characteristic of films by pulsed laser deposition are related to chamber pressure, substrate temperature and target to substrate distance. In this case we used LSCF target for deposition of perovskite film and the chamber pressure was maintained during deposition in range of 50mtorr to 200mtorr. The LSCF film was deposited at room temperature and target to substrate distance was 5cm.

Figure 4.11 shows FE-SEM analysis of LSCF film by pulsed laser deposition. As the chamber pressure of pulsed laser deposition is increased, porosity of the film was increased and the grain was individually dispersed without nearby connection. If the pressure of the chamber increases, the particles of LSCF have more opportunities of scattering in the chamber and grow into larger particle before it reaches to the substrate. Thus, porous and individual grains are grown on the substrates.

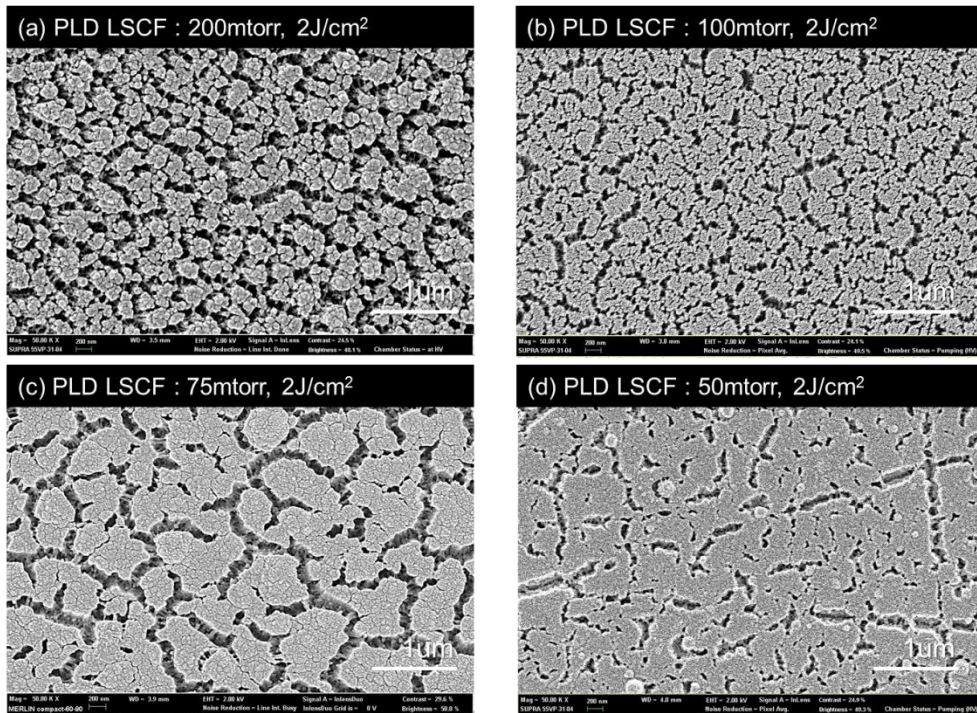


Figure 4.11 Surface FE-SEM analysis of LSCF by pulsed laser deposition at the chamber pressure of (a) 200mtorr, (b) 100mtorr, (c) 75mtorr, (b) 50mtorr

We tested all the cathodes in figure 4.11 and only 75mtorr deposited cell showed proper performance. In case of 200mtorr, 100mtorr deposited LSCF, it has high porosity but the grains are distributed individually. When we deposit current collecting Au layer by sputter, the pores are blocked or distributed individually without any current collecting effects. Although these samples have more catalytic area, individual growth of nano-grained structure is unfavorable for current collection. On the other hand, 75mtorr deposited LSCF has connection between other grains. Thus, current collecting layer can be fabricated by Au sputtering.

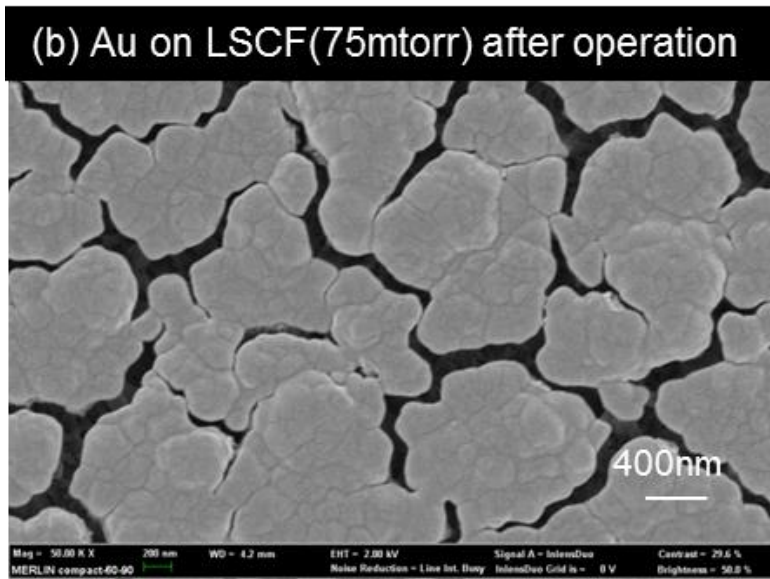
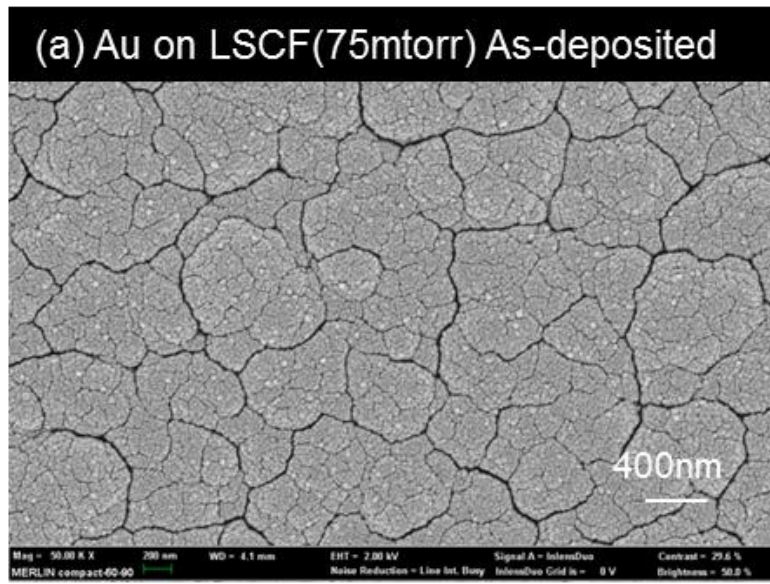


Figure 4.12 Surface images of Au on LSCF (a) as-deposited and (b) after operation.

The surface images of as-deposited and heat treated LSCF films are shown in figure 4.12. According to the as-deposited Au on LSCF, the entire electrode is covered with Au. After the heat treatment at 650°C, the Au showed the same morphology of original LSCF layer by aggregation. The sputtered Au-SSC electrodes have some limitation of increasing porosity but pulsed laser deposited LSCF and Au current collector has advantages of high electric conductivity and high porosity.

#### **4.3.2 Characterization of thin film single chamber SOFCs**

Using the pulsed laser deposited LSCF with Au current collector, we fabricated a cell with a configuration of 500nm Ru-GDC / 550nm YSZ / 100nm GDC / 500nm LSCF-Au (figure 4.13). The 100nm GDC interlayer between electrolyte and cathode was used to enhance oxygen reduction kinetics [62] and the cell was operated at 510°C and 550°C with a methane and air mixture of  $R_{\text{mix}}=2$ .

Figure 4.14 shows the i-V characteristics of thin film single chamber SOFC. The i-V and power density curves were measured at 510°C and 550°C. The initial temperature of cell operation was 510°C. The peak power densities at 510°C and 550°C were 330mW/cm<sup>2</sup> and 560mW/cm<sup>2</sup>. In our knowledge it is the best performance of single chamber SOFC among YSZ cells [71-77]. In table 4.1 the performances and cell configurations of single chamber SOFC using YSZ electrolytes were introduced.

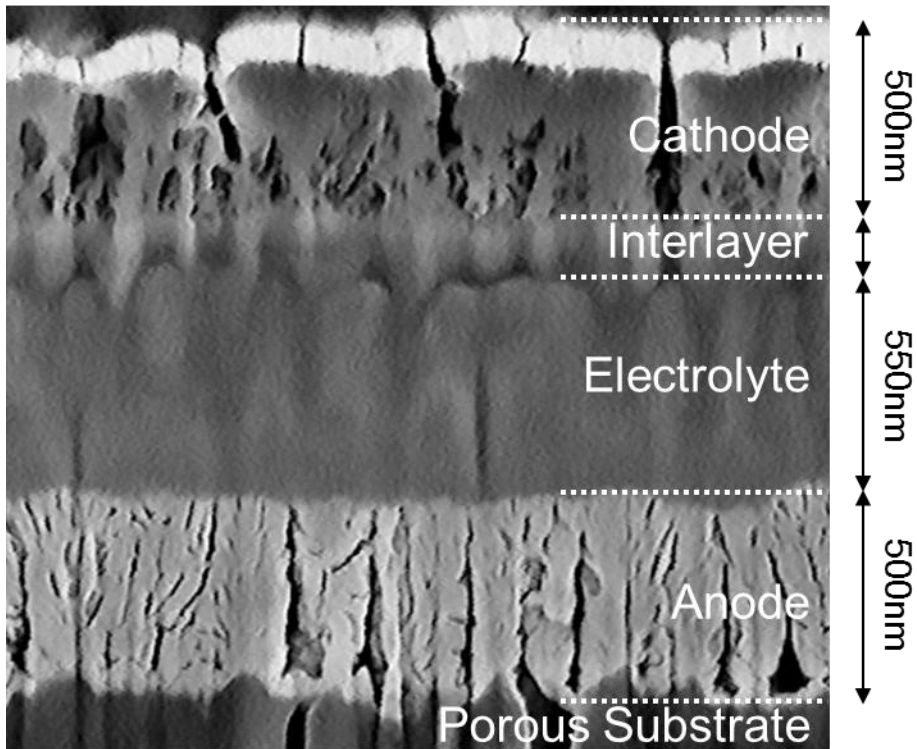


Figure 4.13 Cross section of thin film single chamber SOFCs cell with a cell configuration of Ru-GDC/ YSZ / GDC / LSCF / Au.

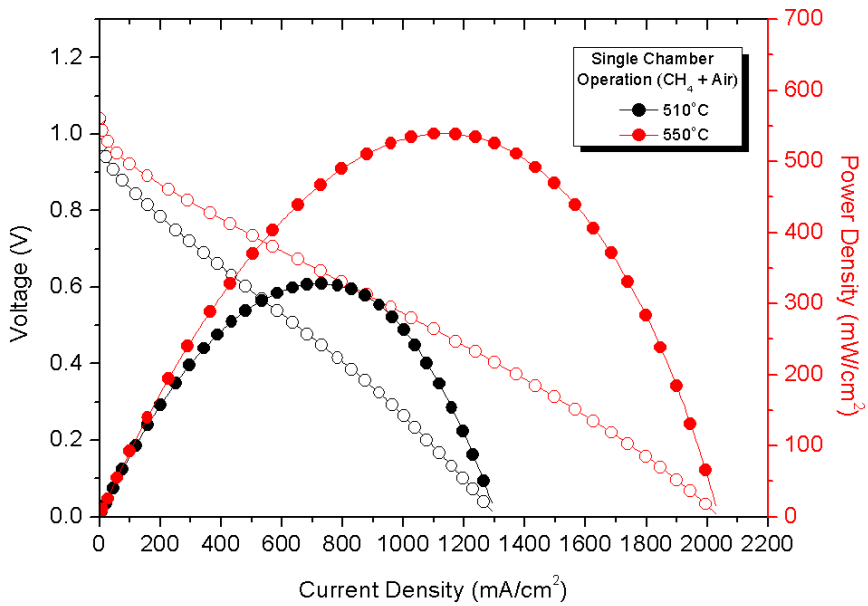


Figure 4.14 I-V behaviors and power densities of thin film single chamber SOFCs cell with a cell configuration of Ru-GDC/YSZ/GDC/LSCF/Au.

Table 4.1 Performances of single chamber SOFC using YSZ electrolyte.

Reference	Electrolyte	Anode	Cathode	Performance
[72]	2um YSZ	Ni-YSZ	LSCF	120mW/cm <sup>2</sup> @ 750°C
[73]	10um YSZ	Ni-YSZ	LSM	360mW/cm <sup>2</sup> @ 800°C
[74]	YSZ	Ni-YSZ	LSCF-GDC	700mW/cm <sup>2</sup> @750°C
[75]	30um YSZ	Ni-YSZ	LSM	280mW/cm <sup>2</sup> @700°C
[76]	8um YSZ	Ni-YSZ	LSM	220mW/cm <sup>2</sup> @600°C
[77]	15um YSZ	Ni-YSZ	LSM-SDC	300mW/cm <sup>2</sup> @650°C
[78]	15um YSZ	Ni-YSZ	LSM-SDC	150mW/cm <sup>2</sup> @700°C
<b>Our research</b>	<b>550nmYSZ</b>	<b>Ru-GDC</b>	<b>LSCF</b>	<b>560mW/cm<sup>2</sup></b> <b>@550°C</b>

#### **4.4 Conclusion**

We successfully fabricated thin film single chamber SOFCs and evaluated electrochemical performances. The thin film SOFC cell using nano-dendritic Ru-GDC anodes showed superior catalytic activity and thermo-mechanical stability compared to the Ni-GDC. The perovskite cathodes were fabricated with sputter and pulsed laser deposition using SSC and LSCF respectively. To improve the electric conductivity of nano fabricated perovskite cathode, Au was used as a current collecting and surface modifying material. The cell showed 560mW/cm<sup>2</sup> of peak power density at 550°C under single chamber condition of  $R_{\text{mix}}=2$  under cell configuration of 500nm Ru-GDC/ 550nm YSZ/ 100nm GDC/ 500nm LSCF.

## Chapter 5 Concluding remarks

In this research, we focused to solve the primary issues of solid oxide fuel cells. In our knowledge, operating temperature, fuel and performances are the main problem to solve. We approached these issues with nano-fabricating devices such as sputter and pulsed laser deposition.

In chapter 2, Thermal barrier coating and dispersion hardening methods were used to improve the thermal stability of nano-porous Pt electrodes. While the pure Pt electrode suffered serious performance degradation due to coarsening at an operating temperature of 500 °C, the thermal barrier coating and dispersion-hardened Pt/GDC electrodes showed superior thermal stability and significant performance enhancement. Different film morphology was observed using the various deposition techniques and GDC ratios, and electrochemical analysis was performed to further investigate the fuel cell performance. The YSZ thin film was fabricated by reactive sputtering of Y/Zr metal alloys and it has advantages of allowing both DC and RF power sources, crack free targets, high deposition rates. Through XRD, XPS and FE-SEM analysis, YSZ thin film by Y/Zr metal alloy showed feasibility for application to thin film SOFCs.

In chapter 3, thin film SOFC based on nano porous AAO has been fabricated using Ru/NiO-GDC anode. The fabricated anode has fine nano structure and thermal durability is superior compared to the conventional Ni anode. Two different fuels (hydrogen, methane) were used to verify the feasibility of direct methane operation and it showed only 10% of performance difference. We used

ruthenium and Ni-GDC layer separately due to the technical problems but we expect the performance difference could be decreased by mixing ruthenium to the entire anode structure.

In chapter 4 we successfully fabricated thin film single chamber SOFCs and evaluated electrochemical performances. Remarkable thing was the structure of dendritic Ru-GDC anodes which have superior catalytic activity and thermo-mechanical stability. The cathodes were fabricated with sputter and pulsed laser deposition. To improve the electric conductivity of nano fabricated perovskite cathode, Au was used as a current collecting and surface modifying material. The Au-SSC co-sputtered cathode shows more than 13time bigger peak power density compared to the pure SSC. In case of cell using pulsed laser deposited LSCF as a cathode, it showed  $560\text{mW}/\text{cm}^2$  of peak power density at  $550^\circ\text{C}$  under single chamber condition of  $R_{\text{mix}}=2$ .

## References

- [1] R. O'Hayre, S.-W. Cha, W. Colella, F.B. Prinz, Fuel cell fundamentals, John Wiley & Sons New York, 2006.
- [2] B.C. Steele, A. Heinzel, Materials for fuel-cell technologies., *Nature*. 414 (2001) 345–352. doi:10.1038/35104620.
- [3] E.P. Murray, T. Tsai, S. a. Barnett, A direct-methane fuel cell with a ceria-based anode, *Nature*. 400 (1999) 649–651. doi:10.1038/23220.
- [4] K. Sasaki, M. Muranaka, a. Suzuki, T. Terai, Synthesis and characterization of LSGM thin film electrolyte by RF magnetron sputtering for LT-SOFCs, *Solid State Ionics*. 179 (2008) 1268–1272. doi:10.1016/j.ssi.2008.02.039.
- [5] S.-E. Lin, Y.-L. Kuo, C.-H. Chou, W.-C.J. Wei, Characterization of electrolyte films deposited by using RF magnetron sputtering a 20mol% gadolinia-doped ceria target, *Thin Solid Films*. 518 (2010) 7229–7232. doi:10.1016/j.tsf.2010.04.082.
- [6] Y.-L. Kuo, C. Lee, Y.-S. Chen, H. Liang, Gadolinia-doped ceria films deposited by RF reactive magnetron sputtering, *Solid State Ionics*. 180 (2009) 1421–1428. doi:10.1016/j.ssi.2009.08.016.
- [7] T. Park, I. Chang, S.W. Cha, Augmentation Method of Triple Phase Boundary in Thin Film Solid Oxide Fuel Cell via Physical Vapor Deposition, *J. Nanosci. Nanotechnol.* 13 (2013) 7834–7838.

doi:10.1166/jnn.2013.8102.

- [8] I. Chang, S. Woo, M.H. Lee, J.H. Shim, Y. Piao, S.W. Cha, Characterization of porous Pt films deposited via sputtering, *Appl. Surf. Sci.* 282 (2013) 463–466. doi:10.1016/j.apsusc.2013.05.153.
- [9] S.M. Kim, J.-W. Son, K.-R. Lee, H. Kim, H.-R. Kim, H.-W. Lee, et al., Substrate effect on the electrical properties of sputtered YSZ thin films for co-planar SOFC applications, *J. Electroceramics*. 24 (2008) 153–160. doi:10.1007/s10832-008-9550-y.
- [10] H. Wang, W. Ji, L. Zhang, Y. Gong, B. Xie, Y. Jiang, et al., Preparation of YSZ films by magnetron sputtering for anode-supported SOFC, *Solid State Ionics*. 192 (2011) 413–418. doi:10.1016/j.ssi.2010.05.022.
- [11] M. Boulouz, a Boulouz, a Giani, a Boyer, Influence of substrate temperature and target composition on the properties of yttria-stabilized zirconia thin films grown by r.f. reactive magnetron sputtering, *Thin Solid Films*. 323 (1998) 85–92. doi:10.1016/S0040-6090(97)01053-5.
- [12] R. Frison, S. Heiroth, J.L.M. Rupp, K. Conder, E.J. Barthazy, E. Müller, et al., Crystallization of 8mol% yttria-stabilized zirconia thin-films deposited by RF-sputtering, *Solid State Ionics*. 232 (2013) 29–36. doi:10.1016/j.ssi.2012.11.014.
- [13] H. Huang, M. Nakamura, P. Su, R. Fasching, Y. Saito, F.B. Prinz, High-Performance Ultrathin Solid Oxide Fuel Cells for Low-Temperature

- Operation, *J. Electrochem. Soc.* 154 (2007) B20. doi:10.1149/1.2372592.
- [14] W. Jung, J.L. Hertz, H.L. Tuller, Enhanced ionic conductivity and phase meta-stability of nano-sized thin film yttria-doped zirconia (YDZ), *Acta Mater.* 57 (2009) 1399–1404. doi:10.1016/j.actamat.2008.11.028.
- [15] M. Tsuchiya, B.-K. Lai, S. Ramanathan, Scalable nanostructured membranes for solid-oxide fuel cells., *Nat. Nanotechnol.* 6 (2011) 282–6. doi:10.1038/nnano.2011.43.
- [16] P. Panjan, B. Hobein, F. Tietz, D. Sto, DC Sputtering of yttria-stabilised zirconia films for solid oxide fuel cell applications, 21 (2001) 1843–1846.
- [17] N. Jordan, W. Assenmacher, S. Uhlenbruck, V. a. C. Haanappel, H.P. Buchkremer, D. Stöver, et al., Ce<sub>0.8</sub>Gd<sub>0.2</sub>O<sub>2</sub> –  $\delta$  protecting layers manufactured by physical vapor deposition for IT-SOFC, *Solid State Ionics.* 179 (2008) 919–923. doi:10.1016/j.ssi.2007.12.008.
- [18] M. Swanson, N. Tangtrakarn, M. Sunder, P.D. Moran, Impact of the presence of grain boundaries on the in-plane ionic conductivity of thin film Gd-doped CeO<sub>2</sub>, *Solid State Ionics.* 181 (2010) 379–385. doi:10.1016/j.ssi.2010.01.020.
- [19] K. Hayashi, O. Yamamoto, Y. Nishigaki, H. Minoura, electrodes for SOFC, 98 (1997) 49–55.
- [20] T. Ishihara, H. Matsuda, Y. Takita, Perovskite Type Oxide as a, (1994) 3801–3803.

- [21] S. Ji, I. Chang, Y.H. Lee, M.H. Lee, S.W. Cha, Performance enhancement of thin-film ceramic electrolyte fuel cell using bi-layered yttrium-doped barium zirconate, *Thin Solid Films*. 539 (2013) 117–121.  
doi:10.1016/j.tsf.2013.05.063.
- [22] I. Chang, P. Heo, S.W. Cha, Thin film solid oxide fuel cell using a pinhole-free and dense Y-doped BaZrO<sub>3</sub>, *Thin Solid Films*. 534 (2013) 286–290.  
doi:10.1016/j.tsf.2013.03.024.
- [23] a. Infortuna, a. S. Harvey, L.J. Gauckler, Microstructures of CGO and YSZ Thin Films by Pulsed Laser Deposition, *Adv. Funct. Mater.* 18 (2008) 127–135. doi:10.1002/adfm.200700136.
- [24] J. Tomaschko, V. Leca, T. Selistrovski, S. Diebold, J. Jochum, R. Kleiner, et al., Properties of the electron-doped infinite-layer superconductor Sr<sub>{1-x}</sub>La<sub>{x}</sub>CuO<sub>{2}</sub> epitaxially grown by pulsed laser deposition, *Phys. Rev. B*. 85 (2012) 024519. doi:10.1103/PhysRevB.85.024519.
- [25] J. Park, J.Y. Paek, I. Chang, S. Ji, S.W. Cha, S.I. Oh, Pulsed laser deposition of Y-doped BaZrO<sub>3</sub> thin film as electrolyte for low temperature solid oxide fuel cells, *CIRP Ann. - Manuf. Technol.* 62 (2013) 563–566.  
doi:10.1016/j.cirp.2013.03.025.
- [26] S. Kang, P. Heo, Y.H. Lee, J. Ha, I. Chang, S.W. Cha, Low intermediate temperature ceramic fuel cell with Y-doped BaZrO<sub>3</sub> electrolyte and thin film Pd anode on porous substrate, *Electrochem. Commun.* 13 (2011) 374–377. doi:10.1016/j.elecom.2011.01.029.

- [27] P. Plonczak, A. Bieberle-Hütter, M. Søgaaard, T. Ryll, J. Martynczuk, P.V. Hendriksen, et al., Tailoring of  $\text{La}_x\text{Sr}_{1-x}\text{Co}_y\text{Fe}_{1-y}\text{O}_{3-\delta}$  Nanostructure by Pulsed Laser Deposition, *Adv. Funct. Mater.* 21 (2011) 2764–2775. doi:10.1002/adfm.201100251.
- [28] J.Y. Paek, I. Chang, M.H. Lee, S. Ji, S.W. Cha, Influence of target to substrate distance on properties of Y-doped  $\text{BaZrO}_3$  Thin films grown by pulsed laser deposition, *Int. J. Precis. Eng. Manuf.* 14 (2013) 839–843. doi:10.1007/s12541-013-0110-2.
- [29] J. Joo, G. Choi, Electrical conductivity of YSZ film grown by pulsed laser deposition, *Solid State Ionics.* 177 (2006) 1053–1057. doi:10.1016/j.ssi.2006.04.008.
- [30] S. Heiroth, T. Lippert, a. Wokaun, M. Döbeli, J.L.M. Rupp, B. Scherrer, et al., Ytria-stabilized zirconia thin films by pulsed laser deposition: Microstructural and compositional control, *J. Eur. Ceram. Soc.* 30 (2010) 489–495. doi:10.1016/j.jeurceramsoc.2009.06.012.
- [31] K. Rodrigo, J. Knudsen, N. Pryds, J. Schou, S. Linderorth, Characterization of yttria-stabilized zirconia thin films grown by pulsed laser deposition (PLD) on various substrates, *Appl. Surf. Sci.* 254 (2007) 1338–1342. doi:10.1016/j.apsusc.2007.07.194.
- [32] J.H. Joo, G.M. Choi, Electrical conductivity of thin film ceria grown by pulsed laser deposition, *J. Eur. Ceram. Soc.* 27 (2007) 4273–4277. doi:10.1016/j.jeurceramsoc.2007.02.135.

- [33] J.H. Shim, C. Chao, H. Huang, F.B. Prinz, S.U. V, R. V April, et al., Atomic Layer Deposition of Yttria-Stabilized Zirconia for Solid Oxide Fuel Cells, (2007) 3850–3854.
- [34] J.H. Shim, J.S. Park, J. An, T.M. Gür, S. Kang, F.B. Prinz, Intermediate-temperature ceramic fuel cells with thin film yttrium-doped barium zirconate electrolytes, *Chem. Mater.* 21 (2009) 3290–3296.  
doi:10.1021/cm900820p.
- [35] B.M. Putkonen, T. Sajavaara, L. Johansson, L. Niinistö, Low-Temperature ALE Deposition of Y<sub>2</sub>O<sub>3</sub> Thin Films from  $\beta$ -Diketonate Precursors \*\*, *Chem. Vap. Depos.* 3 (2001) 44–50.
- [36] M. Putkonen, L. Niinistö, Zirconia thin films by atomic layer epitaxy . A comparative study on the use of novel precursors with ozone, 11 (2001) 3141–3147. doi:10.1039/b105272c.
- [37] M. Putkonen, T. Sajavaara, J. Niinistö, L.-S. Johansson, L. Niinistö, Deposition of yttria-stabilized zirconia thin films by atomic layer epitaxy from  $\beta$ -diketonate and organometallic precursors, *J. Mater. Chem.* 12 (2002) 442–448. doi:10.1039/b107799f.
- [38] C. Bernay, A. Ringuedé, P. Colomban, D. Lincot, M. Cassir, Yttria-doped zirconia thin films deposited by atomic layer deposition ALD: a structural, morphological and electrical characterisation, *J. Phys. Chem. Solids.* 64 (2003) 1761–1770. doi:10.1016/S0022-3697(03)00105-7.

- [39] C. Brahim, a. Ringuedé, M. Cassir, M. Putkonen, L. Niinistö, Electrical properties of thin yttria-stabilized zirconia overlayers produced by atomic layer deposition for solid oxide fuel cell applications, *Appl. Surf. Sci.* 253 (2007) 3962–3968. doi:10.1016/j.apsusc.2006.08.043.
- [40] C.N. Ginestra, R. Sreenivasan, A. Karthikeyan, S. Ramanathan, P.C. McIntyre, Atomic Layer Deposition of Y<sub>2</sub>O<sub>3</sub>/ZrO<sub>2</sub> Nanolaminates, *Electrochem. Solid-State Lett.* 10 (2007) B161. doi:10.1149/1.2759606.
- [41] C.-W. Kwon, J.-W. Son, J.-H. Lee, H.-M. Kim, H.-W. Lee, K.-B. Kim, High-Performance Micro-Solid Oxide Fuel Cells Fabricated on Nanoporous Anodic Aluminum Oxide Templates, *Adv. Funct. Mater.* 21 (2011) 1154–1159. doi:10.1002/adfm.201002137.
- [42] J.H. Shim, C.-C. Chao, H. Huang, F.B. Prinz, Atomic Layer Deposition of Yttria-Stabilized Zirconia for Solid Oxide Fuel Cells, *Chem. Mater.* 19 (2007) 3850–3854. doi:10.1021/cm070913t.
- [43] T. Hibino, A. Hamashimoto, T. Inoue, J. Tokuno, S. Yoshida, M. Sano, A Low-Operating-Temperature Solid Oxide Fuel Cell in Hydrocarbon-Air Mixtures, *Science* (80-. ). 288 (2000) 2031–2033. doi:10.1126/science.288.5473.2031.
- [44] M. Kuhn, T.W. Napporn, Single-Chamber solid oxide fuel cell technology- from its origins to today's state of the art, *Energies.* 3 (2010) 57–134. doi:10.3390/en3010057.

- [45] T. Hibino, A. Hashimoto, M. Yano, M. Suzuki, M. Sano, Ru-catalyzed anode materials for direct hydrocarbon SOFCs, *Electrochim. Acta.* 48 (2003) 2531–2537. doi:10.1016/S0013-4686(03)00296-2.
- [46] P.C. Su, C.C. Chao, J.H. Shim, R. Fasching, F.B. Prinz, Solid oxide fuel cell with corrugated thin film electrolyte, *Nano Lett.* 8 (2008) 2289–2292. doi:10.1021/nl800977z.
- [47] Y.B. Kim, T.M. Gür, S. Kang, H.J. Jung, R. Sinclair, F.B. Prinz, Crater patterned 3-D proton conducting ceramic fuel cell architecture with ultra thin Y:BaZrO<sub>3</sub> electrolyte, *Electrochem. Commun.* 13 (2011) 403–406. doi:10.1016/j.elecom.2011.02.004.
- [48] J. Yoon, R. Araujo, N. Grunbaum, L. Baqué, A. Serquis, A. Caneiro, et al., Nanostructured cathode thin films with vertically-aligned nanopores for thin film SOFC and their characteristics, *Appl. Surf. Sci.* 254 (2007) 266–269. doi:10.1016/j.apsusc.2007.07.053.
- [49] B. Steele, Appraisal of Ce<sub>1-y</sub>Gd<sub>y</sub>O<sub>2-y/2</sub> electrolytes for IT-SOFC operation at 500°C, *Solid State Ionics.* 129 (2000) 95–110. doi:10.1016/S0167-2738(99)00319-7.
- [50] P. Ranran, W. Yan, Y. Lizhai, M. Zongqiang, Electrochemical properties of intermediate-temperature SOFCs based on proton conducting Sm-doped BaCeO<sub>3</sub> electrolyte thin film, *Solid State Ionics.* 177 (2006) 389–393. doi:10.1016/j.ssi.2005.11.020.

- [51] R.A. De Souza, M.J. Pietrowski, U. Anselmi-Tamburini, S. Kim, Z.A. Munir, M. Martin, Oxygen diffusion in nanocrystalline yttria-stabilized zirconia: the effect of grain boundaries, *Phys. Chem. Chem. Phys.* 10 (2008) 2067–2072. doi:10.1039/b719363g.
- [52] P. Heo, T.Y. Kim, J. Ha, K.H. Choi, H. Chang, S. Kang, Intermediate-temperature fuel cells with amorphous Sn<sub>0.9</sub>In<sub>0.1</sub>P<sub>2</sub>O<sub>7</sub> thin film electrolytes, *J. Power Sources.* 198 (2012) 117–121. doi:10.1016/j.jpowsour.2011.09.094.
- [53] D. Pergolesi, E. Fabbri, A. D’Epifanio, E. Di Bartolomeo, A. Tebano, S. Sanna, et al., High proton conduction in grain-boundary-free yttrium-doped barium zirconate films grown by pulsed laser deposition., *Nat. Mater.* 9 (2010) 846–852. doi:10.1038/nmat2837.
- [54] V. Dusastre, J.A. Kilner, Optimisation of composite cathodes for intermediate temperature SOFC applications, *Solid State Ionics.* 126 (1999) 163–174. doi:10.1016/S0167-2738(99)00108-3.
- [55] Y.B. Kim, C.-M. Hsu, S.T. Connor, T.M. Gür, Y. Cui, F.B. Prinz, Nanopore Patterned Pt Array Electrodes for Triple Phase Boundary Study in Low Temperature SOFC, *J. Electrochem. Soc.* 157 (2010) B1269. doi:10.1149/1.3455046.
- [56] X. Wang, H. Huang, T. Holme, X. Tian, F.B. Prinz, Thermal stabilities of nanoporous metallic electrodes at elevated temperatures, *J. Power Sources.* 175 (2008) 75–81. doi:10.1016/j.jpowsour.2007.09.066.

- [57] J.S. Benjamin, Dispersion strengthened superalloys by mechanical alloying, *Metall. Trans.* 1 (1970) 2943–2951. doi:10.1007/BF03037835.
- [58] J. Naser, W. Riehemann, H. Ferkel, Dispersion hardening of metals by nanoscaled ceramic powders, *Mater. Sci. Eng. A.* 234-236 (1997) 467–469. doi:10.1016/S0921-5093(97)00269-4.
- [59] Q. Zhang, D. Zhang, S. Jia, W. Shong, Microstructure and properties of some dispersion strengthened platinum alloys, *Platin. Met. Rev.* 39 (1995) 167–171.
- [60] R.A. Miller, Current status of thermal barrier coatings - An overview, *Surf. Coatings Technol.* 30 (1987) 1–11.  
<http://www.scopus.com/inward/record.url?eid=2-s2.0-0022436687&partnerID=40&md5=2e45ac88baa64d6188e30e2bac9236d2>.
- [61] A.. Brailsford, P. Wynblatt, The dependence of ostwald ripening kinetics on particle volume fraction, *Acta Metall.* 27 (1979) 489–497. doi:10.1016/0001-6160(79)90041-5.
- [62] T. Park, Y.H. Lee, G.Y. Cho, S. Ji, J. Park, I. Chang, et al., Effect of the thickness of sputtered gadolinia-doped ceria as a cathodic interlayer in solid oxide fuel cells, *Thin Solid Films.* 584 (2015) 120–124. doi:10.1016/j.tsf.2015.03.010.
- [63] Z. Fan, F.B. Prinz, Enhancing oxide ion incorporation kinetics by nanoscale Yttria-doped ceria interlayers, *Nano Lett.* 11 (2011) 2202–2205.

doi:10.1021/nl104417n.

- [64] Z. Fan, C.-C. Chao, F. Hossein-Babaei, F.B. Prinz, Improving solid oxide fuel cells with yttria-doped ceria interlayers by atomic layer deposition, *J. Mater. Chem.* 21 (2011) 10903. doi:10.1039/c1jm11550b.
- [65] S. McIntosh, R.J. Gorte, Direct hydrocarbon solid oxide fuel cells, *Chem. Rev.* 104 (2004) 4845–4865. doi:10.1021/cr020725g.
- [66] R.J. Gorte, S. Park, J.M. Vohs, C. Wang, Anodes for Direct Oxidation of Dry Hydrocarbons in a Solid-Oxide Fuel Cell, *Adv. Mater.* 12 (2000) 1465–1469. doi:10.1002/1521-4095(200010)12:19<1465::AID-ADMA1465>3.0.CO;2-9.
- [67] Z. Shao, S.M. Haile, J. Ahn, P.D. Ronney, Z. Zhan, S. a Barnett, A thermally self-sustained micro solid-oxide fuel-cell stack with high power density., *Nature.* 435 (2005) 795–798. doi:10.1038/nature03673.
- [68] I. Chang, S. Ji, J. Park, M.H. Lee, S.W. Cha, Ultrathin YSZ Coating on Pt Cathode for High Thermal Stability and Enhanced Oxygen Reduction Reaction Activity, *Adv. Energy Mater.* 5 (2015) n/a–n/a. doi:10.1002/aenm.201402251.
- [69] S. Park, J. Vohs, R. Gorte, Direct oxidation of hydrocarbons in a solid-oxide fuel cell, *Nature.* 404 (2000) 265–7. doi:10.1038/35005040.
- [70] Y.H. Lee, G.Y. Cho, I. Chang, S. Ji, Y.B. Kim, S.W. Cha, Platinum-based nanocomposite electrodes for low-temperature solid oxide fuel cells with

extended lifetime, *J. Power Sources*. 307 (2016) 289–296.

doi:10.1016/j.jpowsour.2015.12.089.

- [71] M.N.R. Ashfold, F. Claeysens, G.M. Fuge, S.J. Henley, Pulsed laser ablation and deposition of thin films., *Chem. Soc. Rev.* 33 (2004) 23–31. doi:10.1039/b207644f.
- [72] T. Suzuki, P. Jasinski, V. Petrovsky, H.U. Anderson, F. Dogan, Anode Supported Single Chamber Solid Oxide Fuel Cell in CH<sub>4</sub>-Air Mixture, *J. Electrochem. Soc.* 151 (2004) A1473. doi:10.1149/1.1782141.
- [73] T.W. Napporn, X. Jacques-Bédard, F. Morin, M. Meunier, Operating Conditions of a Single-Chamber SOFC, *J. Electrochem. Soc.* 151 (2004) A2088. doi:10.1149/1.1814034.
- [74] I. Riess, P.J. van der Put, J. Schoonman, Solid oxide fuel cells operating on uniform mixtures of fuel and air, *Solid State Ionics*. 82 (1995) 1–4. doi:10.1016/0167-2738(95)00210-W.
- [75] S.P. Yoon, H.J. Kim, B.T. Park, S.W. Nam, J. Han, T.H. Lim, et al., Mixed-fuels fuel cell running on methane-air mixture, *J. Fuel Cell Sci. Technol.* 3 (2006) 83–86. doi:10.1115/1.2134741.
- [76] B. Morel, R. Roberge, S. Savoie, T.W. Napporn, M. Meunier, Catalytic activity and performance of LSM cathode materials in single chamber SOFC, *Appl. Catal. A Gen.* 323 (2007) 181–187. doi:10.1016/j.apcata.2007.02.020.

- [77] M. Liu, Z. Lü, B. Wei, R. Zhu, X. Huang, K. Chen, et al., Anode-Supported Micro-SOFC Stacks Operated under Single-Chamber Conditions, *J. Electrochem. Soc.* 154 (2007) B588. doi:10.1149/1.2724067.
- [78] M. Liu, Z. Lü, B. Wei, X. Huang, K. Chen, W. Su, Effect of the Cell Distance on the Cathode in Single Chamber SOFC Short Stack, *J. Electrochem. Soc.* 156 (2009) B1253. doi:10.1149/1.3196245.

## 국 문 초 록

연료전지는 화학 에너지를 전기 에너지로 직접 변환시키는 장치이기 때문에 효율이 높고, 구동부가 없기 때문에 높은 신뢰성과 지속성, 정숙성을 가진 시스템이다. 하지만 전해질의 재료 특성상 작동 온도가 지나치게 낮거나, 높다는 단점이 존재한다. 이를 해결하기 위해 본 연구에서는 박막 공정을 연료전지 제작에 도입하여 800°C 이상의 높은 온도에서 작동하는 고체산화물 연료전지를 500°C 부근에서 작동시키고자 한다. 이는 고체산화물 연료전지에 값싼 재료의 활용과 높은 신뢰도를 부여한다. 또한 연료전지의 연료로 저장, 보관 및 제조의 효율성이 떨어지는 수소에서 벗어나 탄화수소 기반의 연료를 별도의 개질기 없이 내부 개질 반응을 통해 연료로 쓰하고자 한다. 이는 반응이 더딘 공기극 연구와 내부 개질을 위한 연료극 연구도 병행해야 함을 의미한다.

박막 기술의 연료전지 적용 범위를 알아보기 위해 스퍼터링을 이용하여 금속, 세라믹 복합 나노 전극을 제작하고 이에 따른 공정 변수 및 미세 구조에 따른 성능 차이를 알아보았다. 금속 세라믹 복합체에서는 금속의 함량이 높을수록 큰 입자와 높은 기공률을 보이며 세라믹의 함량이 높아지면 작은 입자와 낮은 기공률을 보였다. 이는 공정 조건 및 금속 세라믹 함량 조절을 통해 박막 구조를 제어 할 수 있음을 의미한다. 또한 박막 전해질을 세라믹 타겟에 RF전력을 가해 스퍼터링을 하는 기존 기술에서 발전된 아르곤 + 산소 기체를 이용하여 금속 타겟을 활용하는 방법을 개발하였다.

위에서 나열한 박막 기술을 활용하여 열화에 안정적인 Ru-Ni-GDC 전극을 개발, 메탄을 개질기 없이 직접 셀에 공급하여 500°C에서 약 80mW/cm<sup>2</sup>의 안정적인 성능을 확보하였다. 박막 고체산화물

연료전지의 메탄 동작은 수소로 동작시켰을 경우와 비교하여 10% 이내의 성능 차이를 보였으며, Ru-Ni-GDC의 혼합도가 더 높아진다면 이 차이는 더 줄일 수 있을 것이라 판단되었다.

마지막으로 단일형 박막 고체산화물 연료전지를 제작, 평가하였다. 나노-텐드라이트 구조의 Ru-GDC 전극을 개발하여 부분 산화 개질 반응을 2배 이상 촉진시켰으며 열화에도 안정적인 성능을 보여주었다. 공기극은 스퍼터와 펄스 레이저 증착법을 이용하여 페롭스카이트 나노 구조체를 제작하였고 집전 저항을 줄이기 위해 금으로 이루어진 집전층을 박막 공정을 통해 제작하였다. 스퍼터로 제작한 페롭스카이트 공기극의 성능을 향상시키기 위해 금을 동시 스퍼터링 하여 입자의 크기, 공극률을 향상시켰고 순수 페롭스카이트 공기극 대비 약 13배의 높은 성능 향상을 이끌어냈다. 펄스 레이저 증착법으로 제작한 공기극을 박막 연료전지에 적용하여 셀을 550°C, 단일형 조건  $R_{mix}=2$ 에서 측정한 결과 약 600mW/cm<sup>2</sup>의 높은 성능을 나타내었다.

주요어: 단일형, 박막 고체산화물 연료전지, 스퍼터링, 펄스 레이저 증착법.

학번: 2010-30966